UNIVERSIDAD NACIONAL AUTÓNOMA DE MÉXICO
PROGRAMA DE POSGRADO EN ASTROFÍSICA

Centro de Radioastronomía y Astrofísica

SISTEMAS DE CÚMULOS GLOBULARES EN AMBIENTES EXTREMOS

PARA OPTAR POR EL GRADO DE
DOCTOR EN CIENCIAS (ASTROFÍSICA)

PRESENTA
KARLA ADRIANA ÁLAMO MARTÍNEZ

TUTORES
DRA. ROSA AMELIA GONZÁLEZ LÓPEZ-LIRA, CRyA
DR. JOHN PAUL BLAKESLEE, HERZBERG INSTITUTE OF ASTROPHYSICS

MORELIA, MICHOACÁN, ENERO 2014

Abstract

Globular Cluster Systems in Extreme Environments

The understanding of what a galaxy is, and of its formation and evolution has been one of the main goals of modern astronomy. During the last decades our knowledge about galaxies has been greatly improved, both observationally and theoretically. However, a general picture that reconciles large and small scales, as well as baryonic and non-baryonic mass is still missing. Globular clusters (GCs) are appealing tracers of galaxy structure, and indicators of formation mechanisms. These systems are very old ($>10\,$Gyr), and so they have imprinted on them the initial conditions of galaxy formation. Furthermore, since GCs are very dense stellar systems (10^3-$10^5 M_\odot\,\mathrm{pc}^{-3}$), they can survive galactic mergers and interactions without being disaggregated. GCs are easily identifiable in faraway galaxies thanks to their compactness and brightness (mean M_V=-7.2 mag). Most galaxies have GCs, from giant ellipticals to dwarf irregulars. Although there are clues about a link between GCs and dark matter, until now it had not been possible to establish how the GCs relate to the dark matter distribution. In this doctoral thesis I study the properties of GC populations (total number, specific frequency, spatial distribution, luminosity function, and color distribution when possible) in extreme systems, in order to find indications about how large structures, such as giant elliptical galaxies, were assembled. By extreme environments I mean fossil groups (FGs), and the center of the massive galaxy cluster Abell 1689 (A1689). These systems are large, massive, distant, and represent the link between regular galaxies and galaxy clusters.

FGs are isolated giant elliptical galaxies surrounded by dwarf companions, all immersed in an extended X-ray halo. They were first identified less than two decades ago, and still are poorly understood. One interpretation of these systems, according to the hierarchical scenario, is that they are the final evolutionary phase of a galaxy group. However, FGs show higher mass-to-light ratios and X-ray-to-optical luminosity ratios than typical galaxy groups; these facts are inconsistent with the assumption that FGs are formed by the merging of the members in ordinary galaxy groups (Khosroshahi et al. 2007). In this project, the GC populations

in three representative systems are studied for the first time. These systems are: the nearest (NGC 6482), the prototype (NGC 1132), and the most massive known to date (ESO 306-G017). Using data from the Advanced Camera for Surveys (ACS) on board the *Hubble Space Telescope* (*HST*), through the filters $F475W$ and $F850LP$, we find that the three FGs show a bimodal GC color distribution, the GCs are spatially more extended than the starlight, and the red population is more concentrated than the blue one. The specific frequency (S_N) of these FGs seems to scale with the optical luminosity, and the values span a range similar to that of bright elliptical galaxies in rich environments. However, when we compare with X-ray data from the literature, we find unexpectedly that the least massive FG in our sample, NGC 6482, has the GC system with the reddest mean color, and the X-ray halo with the highest metallicity. These facts are in disagreement with the well-known mass-metallicity relation. We also analyze the galaxy surface brightness distributions to look for deviations from the best-fit Sérsic profiles, and find evidence of recent dynamical interaction in the FGs. These results have been published in Alamo-Martínez, K. A., et al. 2012, A&A, 546, A15.

In a second project, the GC system in the very massive galaxy cluster, A1689, was studied. A1689 is a well-known gravitational lens with precise measurements of its mass distribution. With the goals of testing the existence of a universal GC formation efficiency per total mass ($\epsilon_t = \mathcal{M}_{GC}/\mathcal{M}_{total}$) in an extreme system, and of exploring the relationship between GCs and dark matter, we have studied the center of this faraway and massive galaxy cluster. Using data from the ACS/*HST* in the $F814W$ filter, we estimate that the total number of GCs within a projected radius of 400 kpc is ∼163,000. This is the largest GC population found to date. The global value of the S_N, corrected for passive evolution, is 14, which is high but expected for central galaxies in massive clusters. Interestingly, by analyzing the behavior of the local S_N in concentric annuli, we find that the cannibalization of normal cluster galaxies by the central cD has already lowered the value of the S_N, suggesting that the high S_N value must have been imprinted in the cluster core at early times.

From the surface number density of GCs, the galaxy luminosity model, the lensing-derived mass distribution, and the X-ray emitting gas, we estimate the mass of each

of these components, and construct its projected radial mass profile. We find that the hot X-ray intracluster gas and the total mass are distributed more smoothly than both the GCs and the stars which shape the galaxies. We calculate the radial profile of ϵ_t, and find that the previous values from the literature (Blakeslee 1999, McLaughlin 1999) are consistent with ours when comparing within the same physical radius. On the other hand, ϵ_t varies with radius in a manner that appears similar for different clusters. We conclude that, although the GC formation efficiency is not universal, the GCs are good tracers of the total mass (baryonic and non-baryonic). It seems that the dark matter halo density governs the GC formation efficiency. These results are published in Alamo-Martínez, K. A., et al. 2013, ApJ, 775, 20.

Resumen

Sistemas de Cúmulos Globulares en Ambientes Extremos

Entender qué son las galaxias, además de sus procesos de formación y evolución, se encuentran entre las principales metas de la astronomía moderna. Durante las últimas décadas, nuestro conocimiento sobre las galaxias ha mejorado notablemente, tanto observacional como teóricamente. Sin embargo, aún hace falta una visión general que reconcilie las pequeñas y las grandes escalas, así como la materia bariónica y la no bariónica. Los cúmulos globulares (GCs) son considerados buenos trazadores de la estructura galáctica. Estos sistemas estelares son viejos, con edades mayores a 10 mil millones de años, de manera que llevan impresas las condiciones iniciales de la formación de las galaxias. Además, dado que son objetos extremadamente densos (10^3-$10^5 M_\odot \, \mathrm{pc}^{-3}$), pueden sobrevivir colisiones e interacciones galácticas sin ser disgregados.

Los GCs son fácilmente identificables en galaxias lejanas gracias a su estructura compacta y a su brillo (M_V=-7.2 mag). La mayoría de las galaxias tienen GCs, desde las gigantes elípticas hasta las enanas irregulares. Aún cuando hay algunas pistas sobre una conexión entre los GCs y la materia oscura, hasta ahora no ha sido posible establecer cómo estas poblaciones estelares se relacionan con la distribución de la materia oscura.

En esta tesis doctoral estudio varias propiedades de las poblaciones de GCs, como su número total, frecuencia específica, distribución espacial, función de luminosidad y distribución de color, en sistemas galácticos extremos, con el fin de encontrar pistas sobre el ensamblaje de grandes estructuras, como son las galaxias elípticas gigantes. Considero como "ambientes extremos" a los llamados Grupos Fósiles (FGs) y el centro del cúmulo masivo de galaxias Abell 1689 (A1689). Estos sistemas son grandes, masivos, lejanos, y representan la conexión entre las galaxias regulares y los cúmulos de galaxias.

Los FGs son galaxias elípticas gigantes rodeadas por compañeras enanas, todas ellas inmersas en un halo extendido de rayos-X; fueron identificados hace menos de dos décadas y su origen aún no se entiende bien. Una interpretación de estos

sistemas, de acuerdo con el esquema jerárquico, es que son la fase evolutiva final de un grupo de galaxias. Sin embargo, los FGs muestran cocientes de masa-luminosidad y rayos X-luminosidad óptica más altos que los grupos de galaxias típicos; esto es inconsistente con el supuesto de que los FGs son formados por la fusión de los miembros de grupos de galaxias ordinarios (Khosroshahi et al. 2007).

En el presente proyecto, fueron estudiadas por primera vez las poblaciones de GCs en tres grupos fósiles representativos: el más cercano (NGC 6482), el prototipo (NGC 1132) y el más masivo conocido a la fecha (ESO 306-G017). Usando datos de la Cámara Avanzada para Sondeos (Advanced Camera for Surveys o ACS, por sus siglas en inglés) a bordo del *Telescopio Espacial Hubble* (*HST*) y con los filtros $F475W$ y $F850LP$, hemos encontrado que los tres FGs muestran una distribución de color bimodal de GCs. Además, los GCs se distribuyen de manera más extendida que las estrellas de campo, y la población de GCs roja está espacialmente más concentrada que la población azul.

Las frecuencias específicas (S_{N}) determinadas para los FGs parecen escalar con la luminosidad óptica, y los valores abarcan un intervalo similar a los de galaxias elípticas en ambientes con densidad galáctica alta. Sin embargo, cuando comparamos con datos de rayos-X, tomados de la literatura, inesperadamente encontramos que NGC 6482, el objeto menos masivo de la muestra, tiene el sistema de GCs con color promedio más rojo y el halo de rayos-X con mayor metalicidad. Esta fenomenología va en contra de la relación masa-metalicidad. También analizamos las distribuciones de brillo superficial en las galaxias con el fin de encontrar desviaciones con respecto a los perfiles de Sérsic que mejor los ajustan, y encontramos evidencia de interacciones dinámicas recientes en los tres FGs.

Estos resultados fueron publicados en el artículo Alamo-Martínez, K. A., et al. 2012, A&A, 546, A15.

En un segundo proyecto, se estudió el sistema de GCs en el cúmulo de galaxias supermasivo A1689, conocido por sus lentes gravitacionales y por sus precisas estimaciones de distribución de masa. Con el objetivo de probar la existencia de una eficiencia de formación de GCs por unidad de masa (ϵ_{t}) universal, en un sistema extremo, y de explorar la relación entre GCs y la materia oscura, hemos estudiado el centro de este lejano y masivo cúmulo de galaxias. Usando datos de

la ACS en el *HST*, con el filtro $F814W$, estimamos que el número total de GCs dentro de un radio proyectado de 400 kpc es $\sim$163,000. Esta es la población de GCs más grande encontrada hasta a la fecha.

El valor global de S_N, corregido por evolución estelar pasiva, es 14, un valor esperado para galaxias centrales en cúmulos masivos. De manera interesante, analizando el comportamiento de S_N local en anillos concéntricos, encontramos que la canibalización de galaxias normales disminuye el valor de S_N, lo que sugiere que el alto valor global de S_N ha sido inscrito en el núcleo del cúmulo en tiempos tempranos.

De la densidad superficial de número de GCs, el modelo de luminosidad de la galaxia, la distribución de masa derivada por el efecto de lente gravitacional y la emisión del gas en rayos-X, estimamos la masa para cada una de estas componentes y construimos su perfil radial de masa proyectado. Encontramos que el gas caliente que emite en rayos-X y la masa total están distribuidos de manera menos concentrada que los GCs y las estrellas que forman las galaxias. Calculamos el perfil radial de ϵ_t y encontramos que los valores de la literatura son consistentes con los nuestros, cuando se los compara al mismo radio físico. Por otro lado, ϵ_t varía con el radio de una forma que parece similar para diferentes cúmulos. Concluimos que, aún cuando la eficiencia de formación de GCs no es universal, los GCs son buenos trazadores de la masa total (bariónica y no bariónica). Aparentemente, la densidad de materia oscura en el halo gobierna la eficiencia de formación de GCs.

Estos resultados fueron publicados en el artículo Alamo-Martínez, K. A., et al. 2013, ApJ, 775, 20.

Acknowledgements

Antes que nada, agradezco a mi Papá, Jorge Alamo, quien siempre me ha apoyado, orientado y motivado con consejos oportunos. Ha sido un pilar en mi vida.

Agradezco a Heinz Andernach quien en la licenciatura me dió el impulso para llegar a donde estoy ahora. Agradezco a Rosa Amelia, quien desde un inicio confió en mí, por sus consejos tanto académicos como personales. A John Blakeslee y Michael West por haber confiado en mí estos grandes proyectos, por su paciencia, tiempo, y motivación; siempre procuraron darme las herramientas necesarias. A Karin Hollenberg y Paulina Jirón por hacer la vida más sencilla. Al CRyA, ESO Chile, y HIA por abrirme las puertas.

A mi tía Lupita, a mis hermanos: Claudia, Luis, y Jorge. A Xochitl, Mónica y José Luis. A mis amigos que hicieron más ligero el camino, especialmente a Georgina Ramirez, Jesus Toalá, Miriam Díaz, Paulina Lares, Mariana Medina, Carlos Carrasco, Gabriela Montes, Roberto Galván, Rosa Torres y Lucie Jilkova.

Y por último pero no menos importante, a mi compañero, amigo, soporte, amor, Vicente.

Contents

Chapter 1

Globular Clusters

On clear nights, besides stars, nebulous objects are visible with the naked eye across the sky. Some of these nebulous objects are: ωCentauri, 47 Tucanae, M3, M22, and M13; the first humans who observed the sky must have been aware of them. However, a telescope is needed to resolve the stars within these nebulous objects. In the literature, the credit for the discovery of the first stellar cluster has been awarded to a certain German Astronomer Abraham Ihle, who observed M22 in 1665. However, nothing is known about Abraham Ihle, and it has been suggested that 'Ihle' is a misprint for 'Hill' (Burnham 1966). The first confirmed reports of star clusters were made by Halley (1677), Kirch (1681), La Caille (1752), Messier (1764), and Herschel (1782). But it was in the *Catalogue of a Second Thousand of New Nebulae and Clusters of Stars* (1789), where William Herschel studied the shape of stellar clusters, and found an increased accumulation of stars towards the center; discussing their appearance, he inferred that these systems were indeed spherical, and called them **globular clusters (GCs)**.

As the mapping of the sky continued with better instruments, more GCs were reported, not only in the Milky Way but in external galaxies too. And the more they were studied, the more intriguing their properties became.

1.1   Individual Properties

1.1.1   Size

Not a long time had passed after the invention of photography (early nineteenth century), when it was applied to the study of the heavens. Thanks to photographic plates, it was possible to systematically obtain accurate brightness measurements of stars and other celestial objects.

FIGURE 1.1:   *HST* optical image of the globular cluster M80.   Field of view:$\sim 3' \times 3'$ (at a distance of $8.7\,\mathrm{kpc}$ corresponds to $\sim 7.6\mathrm{pc} \times 7.6\,\mathrm{pc}$).   Credit: Hubble Heritage Team (AURA/ STScI/ NASA).

In 1912, Leavitt found a correlation between the brightness and the period of the light curve of some supergiant stars (with radii hundreds of times the solar radius), the Cepheid variables. In 1913, Hertzsprung combined the Leavitt data with proper motion measurements to calibrate this period-luminosity relationship, and used it as a method to estimate distances. Globular clusters possess many variable stars, although most of them with shorter periods (less than one day) than Cepheids ($\sim$ 1-50 days). Eddington (1917) studied the light curves of tens to a hundred variable stars in some GCs, to then estimate an average magnitude for each GC. He assumed that the differences in brightness between GCs were

a consequence of their relative distances. However, he could determine neither absolute magnitudes nor distances.

In 1917, Shapley applied the Cepheid period-luminosity method, using *cluster-type variables*, to calculate the distance to and the physical dimensions of the GC M3. Now we know that those variable stars were RR Lyrae, not Cepheids, and that they do not follow the same period-luminosity relation (Baade 1956). Despite the wrong distance, the physical radius of $\sim$70 pc for M3 reported by Shapley is about twenty times bigger than the right one.

The first systematic measurements of Galactic GCs' physical sizes were limited by the spatial resolution of the data. van den Bergh (1956) determined the radii of 36 GCs, defined as the mean distance of the variable stars to the GC center. He reported a mean value of ~ 5 pc, and noted an increase in GC diameter with distance of the cluster from the Galactic plane.

Although the mean distance of the variables from the GC center seemed to be a good indicator of the main body size, it is expected to be different for each cluster due to dynamical evolution. Spitzer & Thaun (1972) showed that the radius that encloses half of the total mass of the system, the *half mass radius*, is a better parameter to describe GC size, since it is practically unaffected by dynamical evolution. As the stellar content of GCs consists mainly of low mass stars, with mass-to-light ratios (M/L, in solar units) of $\sim 1 - 2$ (Pryor & Meylan 1993), the *half mass radius* and the *half light radius* ($r_{\rm h}$), are used interchangeably.

Recent values of the sizes of globular clusters are expressed in terms of $r_{\rm h}$. van den Bergh et al. (1991) determined $r_{\rm h}$ for 98 Galactic GCs by fitting Kron & Mayall (1960) profiles to the photometric measurements. He also found a similar mean value of $r_{\rm h}$ $\sim$5 pc, and confirmed the correlation between GC diameter and Galactocentric distance. Kundu & Whitmore (2001) used Wide Field and Planetary Camera 2 (WFPC2) on board *Hubble Space Telescope* (*HST*) data to measure $r_{\rm h}$ for several hundreds of GCs in 28 elliptical galaxies. The determination of $r_{\rm h}$ was done by fitting the point spread function (PSF) convolved with a King (1966) profile. The mean value for the complete sample is $\langle r_{\rm h}\rangle$=2.4$\pm$0.4 pc. They claimed that this value is independent of host galaxy luminosity, suggesting that this *preferred* size could be used as a distance indicator.

More recently, Jordán et al. (2005) measured r_h for more than five thousand GCs belonging to 100 Virgo cluster galaxies, using the Advanced Camera for Surveys (ACS) on board *HST* (program ACS Virgo Cluster Survey, ACSVCS, Côté et al. 2004). They derived an average value of $\langle r_\mathrm{h} \rangle$=2.7±0.35 pc. Also, they found that the average r_h decreases with redder host galaxy color, and a dependence with GC color as well (red GCs being ∼17% smaller than blue ones). This study confirmed the increase of r_h with Galactocentric distance, and corroborated that, after correcting for the aforementioned trends, r_h is very homogeneous and hence can be used as a standard ruler for distance estimation.

1.1.2   Color Magnitude Diagram

The Color Magnitude Diagram (CMD) is a tool that has played a very important role in astronomy. The CMD is a variant of the Hertzsprung-Russell (HR) diagram, which displays the spectral type (indicator of surface temperature) of stars on the horizontal axis and their luminosity on the vertical axis. The first HR diagram was constructed with stars from the Solar neighborhood (Russell 1914). Using parallax measurements to estimate distances, Russell found that stars with the same apparent magnitude but different spectral type were located at different distances, the blue stars being farther away (thus more luminous) than the red ones. Russell noted that the absolute magnitude of giant stars was nearly independent of their spectral type, or perhaps slightly fainter for the reddest giants.

The first study of magnitudes and colors of individual stars within GCs was done by Shapley (1916). It included only the brightest stars (brightest four magnitudes), and noted the tendency of the brightest stars to have the reddest colors (Fig. 1.2). This fact was in contradiction with Russell's result for Solar neighborhood stars, suggesting an essential difference between these stars and the ones within GCs. Now we know that the stars that Shapley studied have already left the main sequence (see Figure 1.4): they are red giant stars, while Russell's stars are in the main sequence. Incidentally, the first diagrams (both of GCs and of Solar neighborhood stars) had magnitude on the horizontal axis and spectral class (or color) on the vertical axis (see Fig. 1.2) contrary to modern CMDs.
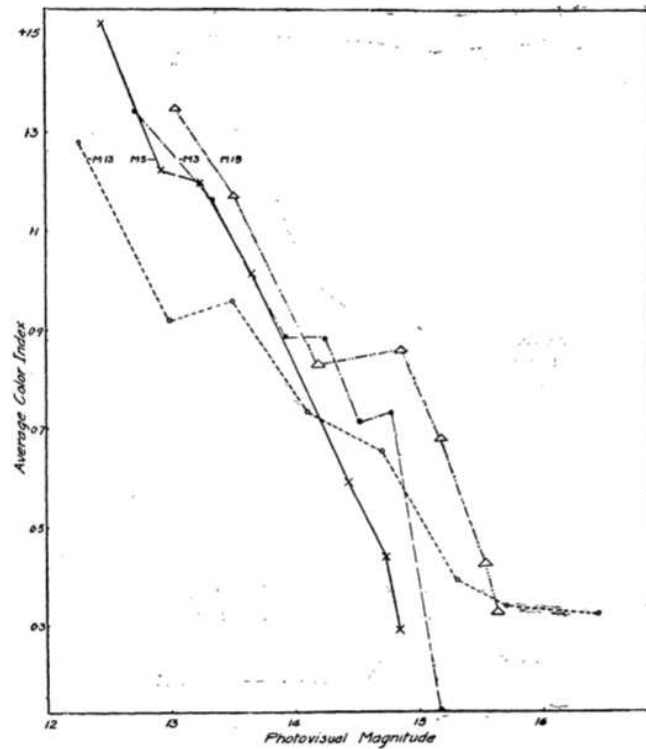
FIGURE 1.2: Apparent magnitude vs. color of the brightest thousand stars of
the GCs M13, M5, M3, and M15. Shapley (1916).

The study of the stellar content (spatial distribution and frequency of each spectral
type) within GCs started to be exploited. Arp (1955) published the first systematic
investigation of CMDs for 7 GCs.

After photographic plates came charged coupled devices (CCDs), and new instruments have improved the accuracy of brightness measurements and have better
spatial resolution. The *HST* has provided a huge amount of data. Thanks to refined photometric techniques, it has been possible to construct with them accurate
and deeper CMDs with more than 10,000 stars per GC (Sarajedini et al. 2007).

1.1.3 Ages

With the development of the theory of stellar evolution (Eddington and Chandrasekhar in the early twentieth century), it was understood that the CMD shows
the paths followed by stars on different stages of their life, from birth to death.

FIGURE 1.3: ACS/HST CMDs for NGC 5466 (21 449 stars, left panel) and NGC 5053 (15 618 stars, right panel). The plus signs represent stars with at least one saturated pixel in either or both of the F606W and F814W images. Sarajedini et al. (2007).
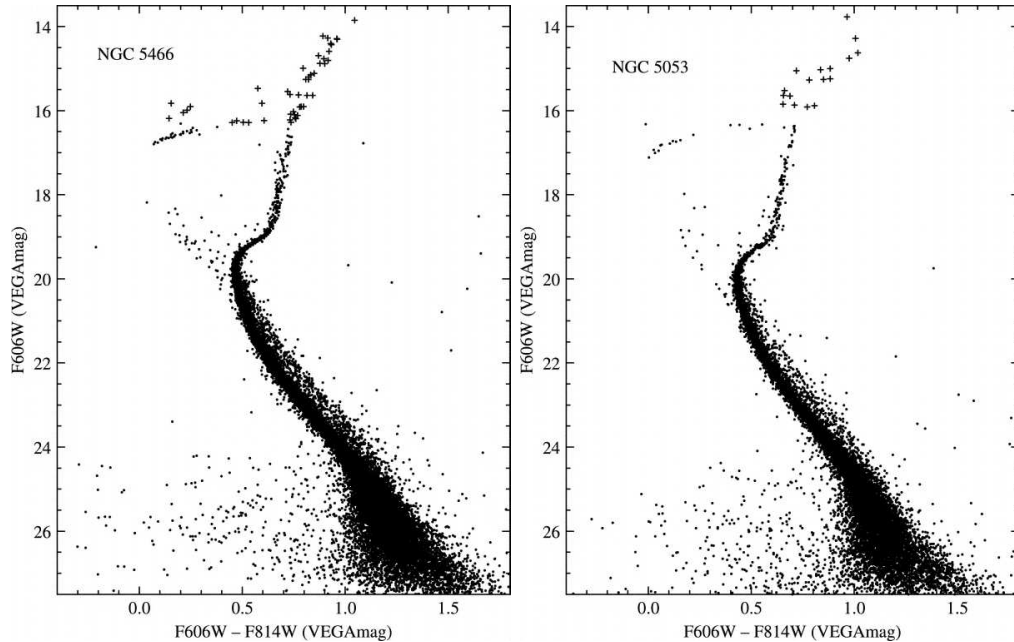
The color (or surface temperature) and luminosity are determined by the stellar mass and chemical composition. An approximation to the surface temperature is the effective temperature ($T_{\rm eff}$), which is the temperature of a black body with the same radius and luminosity as the star ($L = 4\pi R^2 \sigma T_{\rm eff}^4$, Stefan-Boltzmann law). The radius of a star can be determined from its luminosity and $T_{\rm eff}$.

Stellar evolution is strongly dependent on initial mass. The description below is for typical stars within GCs (mass $<1.5 M_\odot$). Every star starts burning hydrogen into helium in its core (main sequence), spending in this stage most of its lifetime. When the hydrogen is exhausted in the core ($\sim10\%$ of the initial hydrogen mass), the star leaves the main sequence (reaching the main sequence turnoff, MSTO). There is not enough radiative pressure to support the star, and the core contracts, releasing gravitational energy that is absorbed by the hydrogen envelope; as a consequence, the envelope expands (increasing the radius and thus the luminosity), and the star evolves into a red giant, while it burns hydrogen in a shell around the helium core. Then the helium core ignites, and the star sheds some of its envelope and enters the horizontal branch. Those stars that have lost only a

moderate amount of mass as red giants end up on the red horizontal branch, while those that have lost more enter the blue horizontal branch. The next phase is the asymptotic giant branch, with helium burning in a shell around an inert carbon core, and hydrogen burning in another shell around the first one (Fig. 1.4). Lastly, a star may then shed its envelope and become the nucleus of a planetary nebula.
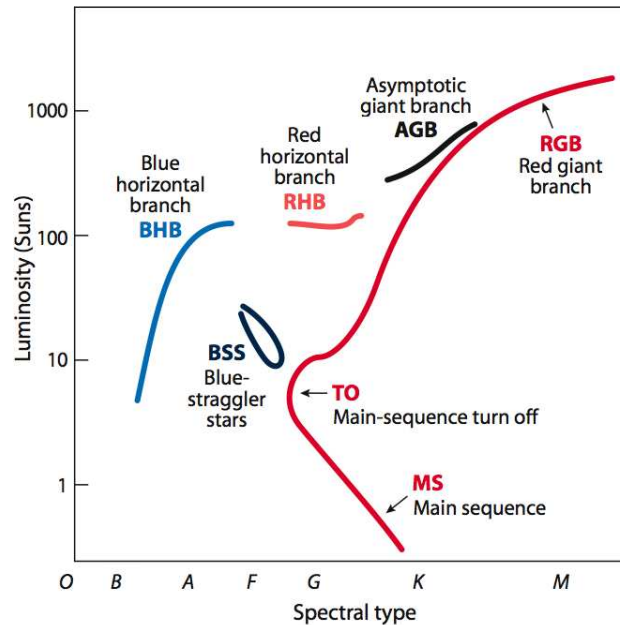
FIGURE 1.4: Representation of a GC CMD, showing the main evolutive stellar stages. Djorgovski (1998).

Knowing the initial mass and metallicity of a star, it is possible theoretically to predict its color and luminosity along its evolution. On the other hand, if we measure from observations color and luminosity (and assume or measure a certain metallicity), the age can be inferred. This method has been applied to estimate the age of GCs using their observed CMDs, by identifying and measuring the observed MSTO point and then comparing it with theoretical stellar evolution models (synthetic CMDs).

Hoyle (1959) constructed the first stellar evolutionary models, which were applied by Sandage (1962) to estimate stellar ages from the CMD of the open cluster NGC 188, assuming the same chemical composition as the Hyades. Afterwards, this method was applied to GCs (M3, M5, and M13), obtaining ages of ∼24Gyr. Improved evolutionary stellar models covering wider ranges of stellar mass, helium

content, and heavy-metal abundance (Demarque 1967, Hartwick & VandenBerg 1973, Sandage 1982, VandenBerg 1983) were developed in the following decades, resulting always in old ages for GCs ($>14\,\mathrm{Gyr}$). Most of these age measurements were performed on GCs located in the Galaxy's halo. GCs started to be recognized as the oldest Galactic stellar populations, providing a lower limit for the age of the universe. This motivated a very active research on GCs. Special effort was invested in GC age determination (Sandage 1982, VandenBerg 1983, VandenBerg 1988).

In practice there are some complications with this technique: (1) the determination of a single point (see Figure 1.3) is difficult, and the MSTO magnitude can have large uncertainties (Chaboyer et al. 1996); (2) the theoretical stellar models used for comparison have many assumptions (initial mass function, helium composition, heavy-metal abundance, T_{eff}-color transformation) and simplifications (RGB and AGB phases, convection layers, atmosphere structure). For example, the MSTO is brighter for bluer globulars (Sandage 1982); assuming a wrong metal abundance will affect the estimated age. However, this is the most accurate and calibrated clock for GCs (Renzini 1991). Unfortunately, it can only be applied to nearby GCs (belonging to the Milky Way or nearby galaxies).

On the other hand, relative ages between GCs can be obtained by comparing the separation in magnitudes between the MSTO and the horizontal branch at the same color, $\Delta V_{\mathrm{MSTO}}^{\mathrm{HB}}$ (VandenBerg et al. 1990, De Angeli et al. 2005). As the globular system evolves, this magnitude difference will be larger. However, since the region around the MSTO is vertical, the uncertainties are large. Buonanno et al. (1998) suggested to use a spot in the MS close to the MSTO but where the slope is not vertical, and chose the arbitrary location in the MS with color = MSTO color + 0.05 (right panel of Figure 1.5).

More recently, Sarajedini et al. (2007), within the ACS Survey of Galactic Globular Clusters program, obtained high quality photometry of 65 Galactic GCs, covering from the horizontal branch down the main sequence to $\sim 0.2 M_{\odot}$ (~ 7 mags below the MSTO). These data provided well defined CMDs for a large and homogeneous sample, allowing Sarajedini et al. to fit not only the MSTO point, but the subgiant
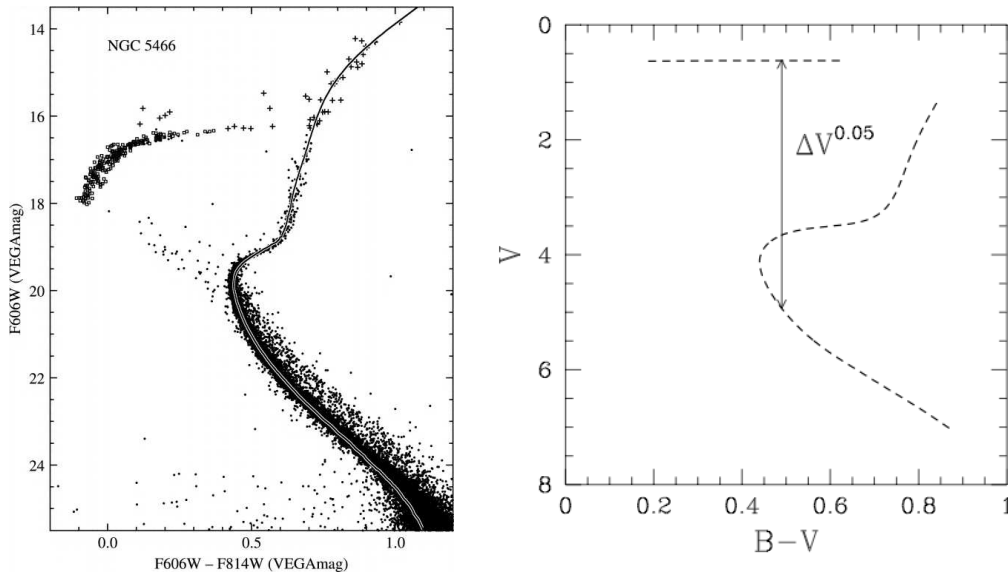
FIGURE 1.5: *Left panel:* ACS/*HST* CMD for NGC 5466 (21 449 stars). The plus signs represent stars with at least one saturated pixel in either or both of the F606W and F814W images. The solid line shows the theoretical isochrone fitted, from which the age was estimated. Sarajedini et al. (2007). *Right panel:* Representation of a CMD, indicating the magnitude difference between the horizontal branch and the magnitude at the color of MSTO + 0.05. Buonanno et al. (1998).

branch slope and giant branch; they obtained ages in the range of 12 to 14 Gyr for most of the globulars.

Theoretical stellar models are also used to construct synthetic spectra for comparison with observations. Worthey (1994) showed that certain absorption features are good indicators of metallicity or age, and can thus break the degeneracy observed in broadband colors. Balmer lines, for example, are sensitive to age. The strongest Balmer lines ($\sim$4000Å) are evident in the young GC spectrum of Figure 1.6. Integrated light spectroscopy has been used to measure ages and metallicity mainly in extragalactic GCs, confirming old ages (> 10 Gyr) for most of them (Cohen et al. 1998; Puzia et al. 2005).

Despite the difficulties and uncertainties in GC age measurements (see Brodie & Stradler 2006), it is a fact that they are very old objects. The estimated ages have imposed constraints on the age of the universe and on galaxy formation theories;
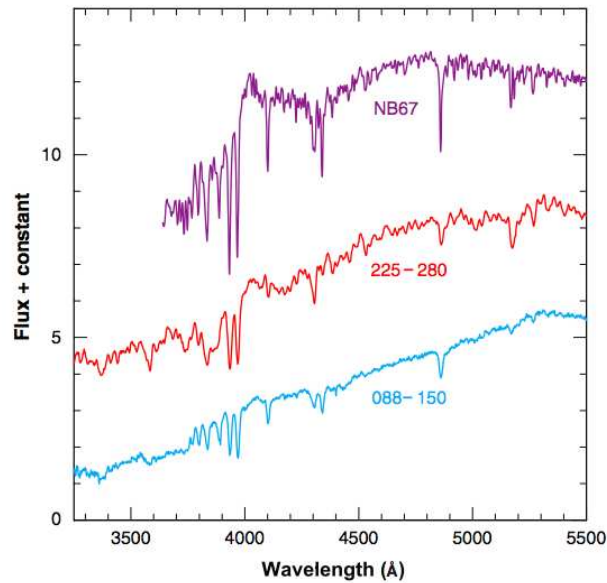
FIGURE 1.6: Representative spectra of three M31 GCs. Bottom: old metal-poor. Middle: old metal-rich. Top: intermediate-age and intermediate metallicity. Brodie & Stradler (2006).

most of them have ages older than 10 Gyr, and therefore probably formed before or during galaxy assembly.

1.1.4 Structure and Dynamics

Globular clusters contain neither gas nor dust, only old stars shaped into a spherical morphology that suggests they are dynamically stable.

In 1962, King studied the spatial distribution of stars within GCs, and found an empirical density law that describes the structure of the clusters. King showed that the radial density profile can be represented with three parameters:

1. Core radius. Measure of the internal energy of the system. Approximated as the radius at which the central surface brightness has dropped by half.

2. Limiting (or tidal) radius. Measure of the external tidal field. The radius of gravitationally bound stars, beyond which the cluster cannot hold stars against the tidal force of the host galaxy.

3. Richness factor. Measure of the total number of stars. It is related to the total brightness or central surface brightness.

Peterson & King (1975) determined the structural parameters of 101 GCs. Furthermore, by fitting theoretical models to photometric data, they estimated: densities ($\sim 10^2 - 10^4 M_\odot \, \mathrm{pc}^{-3}$), velocity dispersions ($\sim$2-10 km s^{-1}), and escape velocities ($\sim$10-40 km s^{-1}). In 1993, Pryor & Meylan published a homogeneous sample of 56 Galactic GCs with spectroscopic measurements; they derived their velocity dispersions from Doppler broadening of integrated spectra, or with radial velocities of individual stars. They estimated the masses ($\sim 10^4 - 10^6 \, M_\odot$), global M/L ratios ($\sim$2), densities ($\sim 10^2 - 10^6 M_\odot \, \mathrm{pc}^{-3}$), and velocity dispersions ($\sim$3-15 km s^{-1}).

Eddington (1913b, 1915) studied the dynamics of globular stellar systems, and claimed that stars move in undisturbed paths under the general attraction of the whole system, without being affected by encounters. However, due to the very high stellar densities of $\sim 10^4 M_\odot \, \mathrm{pc}^{-3}$ in GCs cores (for comparison, in the Solar neighborhood the stellar density is $\sim 0.05 M_\odot \, \mathrm{pc}^{-3}$, Binney & Tremaine 1987), interactions between stars are expected.

On the other hand, the most massive stars are located in the inner regions; this is the so-called *mass segregation*, which is a consequence of dynamical friction. When a star moves through a uniform stellar distribution, it attracts (deflects) the close field stars, causing an overdensity behind it. The star's trajectory will not be affected in the perpendicular direction, but in the direction of movement the star will be decelerated, attracted by the overdensity (Figure 1.7). Thus the star loses kinetic energy and sinks to the cluster center. The deceleration is proportional to the mass of the star, hence the most massive ones will end up located near the center.

The dynamical evolution of a GC is dominated by dynamical relaxation and gravitational shocks when the cluster passes through the galactic bulge or disk. Dynamical relaxation can be seen as energy equipartition, where less massive stars will have higher velocities farther from the cluster center, and the massive ones with lower velocities will be located close to the center (mass segregation is a consequence of dynamical relaxation). In such a system the stars follow a Maxwellian
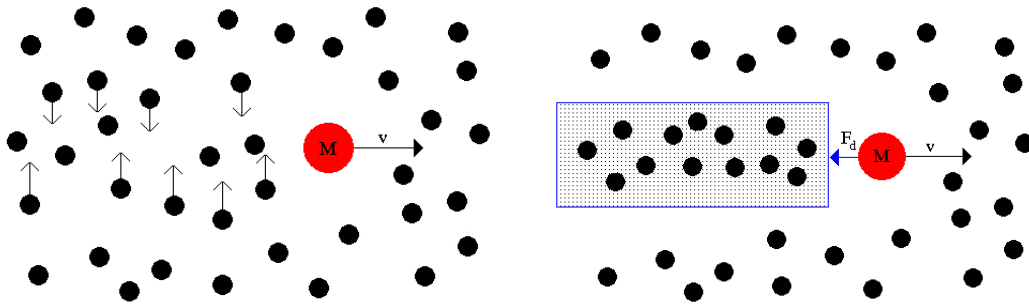
FIGURE 1.7: Dynamical friction simplified sketch. Schombert Lectures.

velocity distribution, and some stars in the high velocity Gaussian tail will exceed the escape velocity and evaporate from the system. The loss of these high velocity stars is also a loss of kinetic energy (or pressure), thus this evaporation is followed by a contraction of the cluster: this is the mechanism of GC *core-collapse* (Spitzer & Hart 1971). Observationally, GCs are classified in two types according to their central surface brightness: *core* or *cusp*. The surface brightness radial profile of the core-GCs is constant in the central region (King's profile), while it increases for smaller radii in cusp-GCs. Cusp-GCs are interpreted as globulars that already have undergone a core-collapse (and consequently have a denser core), and are more evolved than core-GCs.

1.1.5   Stellar Content

In 1927, Shapley & Sawyer published a classification of 95 Galactic GCs highlighting their uniform apparent sizes, shapes and luminosities. To first order GCs are simple, single stellar populations: stars at the same distance, coeval, and chemically homogeneous. However, when they are closely investigated, complexity emerges.

Since early studies of chemical abundances, variations from star to star within a given GC were reported (Kraft 1979, Freeman & Norris 1981).

With *HST*'s superb spatial resolution, it was confirmed that GCs are not as simple as once thought. Piotto et al. (2007) found three main sequence branches in the

GC NGC 2808, and associated them with a complex metal abundance distribution. Many GCs show complex CMD features, such as double or multiple main sequences, subgiant and giant branches, extended horizontal branches (Piotto et al. 2012), as well as individual stars with abundance variations of light elements (Gratton et al. 2012).

Several theories have attempted to explain these CMD 'anomalies'and abundance complexities. The more intuitive and probably simpler is that those stars were formed from material with different initial metal abundances. As both populations belong to the same cluster, it has been suggested that they were born on different epochs, *in situ*, where the first generation contaminated the gas from which the next generation was formed.

Goudfrooij et al. (2011) calculated the mass young clusters need in order to retain the material processed from the first generation of stars (i.e., escape velocities would have to be larger than stellar winds and ejecta velocities), and claimed that current GCs with $r_{\rm h} \sim 3\,{\rm pc}$ and mass $\sim 5 \times 10^3 M_\odot$ were able to retain the chemically enriched material when they were young (10 Myr). If the chemical differences are due to multiple star formation episodes, it is expected to find evidence of star forming activity in young massive clusters. Bastian et al. (2013) looked for ongoing star formation within 130 young massive clusters (expected to be GCs in the future), without finding any evidence of it (they noted complex CMDs for some clusters but not current star formation). Bastian et al. suggested an alternative mechanism for metal contamination: through protostellar disc accretion of the ejecta of high mass stars and interacting binaries (all of the same generation). This is viable given the very high stellar density at GC cores, where close encounters might be very common, with some of them resulting in interactions. Thus, accretion of material from depleted red giant envelopes, stellar winds, fast rotating stars or interacting binaries is an alternative.

The explanation of these abundance anomalies is still an open question, and its understanding will shed light on GC formation and evolution.

1.2 Globular Cluster System Properties

Summarizing the previous section, GCs are old ($>10\,\mathrm{Gyr}$), massive ($\sim 10^4$-$10^6 M_\odot$), compact ($r_\mathrm{h} \sim 3\,\mathrm{pc}$), and very dense ($10^3$-$10^5 M_\odot\,\mathrm{pc}^{-3}$) stellar systems. These spherical clusters do not contain gas, dust, or dark matter (M/L ratios ~ 2). They are survivors of galactic assembly, and their properties can constrain galaxy formation theories.

GCs are easily identifiable in faraway galaxies thanks to their compactness and brightness (mean absolute magnitude in V=-7.2 mag). Most galaxies have GCs, from giant ellipticals to dwarf irregulars. Unfortunately, it is not possible to study the stellar content of individual GCs belonging to distant galaxies, but we can study homogeneously the whole GC population (or most of it) from a larger scale perspective: its spatial distribution, total number, ages and metallicities from integrated spectra, and luminosity function. Hubble, Harris, and van den Bergh are the pioneers in studying GC system properties as tracers of galaxy structure and indicators of formation mechanisms. Actually, GC system properties are much more homogeneous than those of their parent galaxies (Harris & Racine 1979).

On the other hand, GCs have been studied extensively in elliptical galaxies for three main reasons: their numbers are larger than in spiral galaxies, they are easily recognizable against the background galaxy (star forming regions and open clusters affect strongly the identification of GCs in spirals), and extinction by dust is minimal.

1.2.1 Specific Frequency

The most basic measure of a GC system is its richness, or the total number of globulars. Harris & van den Bergh (1981) introduced the concept of *specific frequency*, S_N, as the number of GCs (N_GC) per unit galaxy luminosity, normalized to a galaxy with absolute V magnitude of -15, i.e.:

$$S_N = N_\mathrm{GC} 10^{0.4(M_\mathrm{V}+15)}, \tag{1.1}$$

where M_V is the absolute magnitude of the galaxy in the V band, both quantities (N_{GC} and M_V) measured over the same area. They reported values in the range $4 < S_N < 10$ for elliptical galaxies. Later, van den Bergh & Harris (1982) measured S_N in spirals and found values < 1. In 1991, Harris published a homogenized catalog of S_N for galaxies with different morphological type, and confirmed that the values for spirals and irregulars (~ 1) are different from the ones of dwarf and regular ellipticals (~ 5). This apparently fundamental difference between spirals and ellipticals was already noted by Harris & Racine (1979) when they attempted to find a proportionality between N_{GC} and parent galaxy luminosity for different galaxy types. They claimed that spirals and irregulars were too bright for their estimated N_{GC}, compared to the relationship shown by ellipticals.
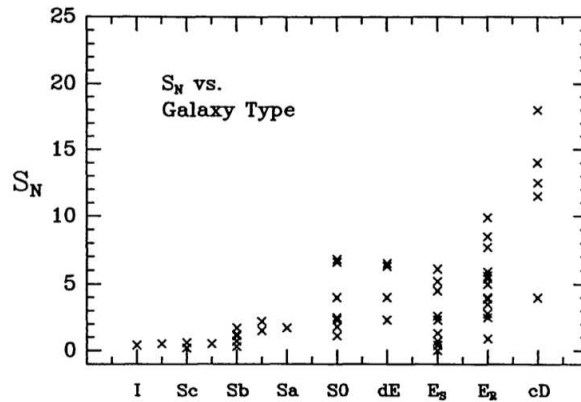
FIGURE 1.8: Specific frequency, S_N, for different morphological types. E_S and E_R are ellipticals in sparse and rich clusters, respectively. Harris (1991).

Interestingly, Harris & van den Bergh (1981) also noted that M 87, the central giant elliptical in the Virgo cluster, had an outstandingly large value of $S_N \sim 20$ (a more recent value from Peng et al. 2008 is $S_N = 12.6 \pm 0.8$). Later, other high-S_N galaxies were identified (Harris 1991), most of them being either brightest cluster galaxies (BCGs) or second brightest cluster galaxies; often, these galaxies were classified as type cD (giant elliptical with an extended envelope, see Section 2.1.1). However, not all galaxies classified as cDs have high S_N (Jordán et al. 2004). It is interesting to remark that, although BCGs have quite a uniform luminosity, to the point of being considered standard candles (Postman & Lauer 1995), they have a wide range of S_N.

More recent typical values of S_N for different morphological types are:

Spirals: 0.5 to 1 (Goudfrooij et al. 2003; Rhode & Zepf 2004).

Regular ellipticals: 2 to 6 (Kundu & Whitmore 2001; Peng et al. 2008).

Giant ellipticals: 4 to ∼15 (Harris 1991; Peng et al. 2008; Jordán 2004; Georgiev et al. 2010).

Dwarf (spheroidals and irregulars): 0 to ∼100 (Harris 1991; Peng et al. 2008; Georgiev et al. 2010).

Even though dwarf galaxies and giant ellipticals show similar S_N values, they follow opposite trends with luminosity. For dwarfs, S_N tends to increase as the luminosity decreases. Conversely, for giants S_N tends to increase with luminosity (Figure 1.9), in both clusters and isolated environments (Cho et al. 2012). Peng et al. (2008), in a study of 100 early-type galaxies from the ACSVCS, claimed that this S_N behavior is driven by the metal-poor GCs (see Section 1.2.2).
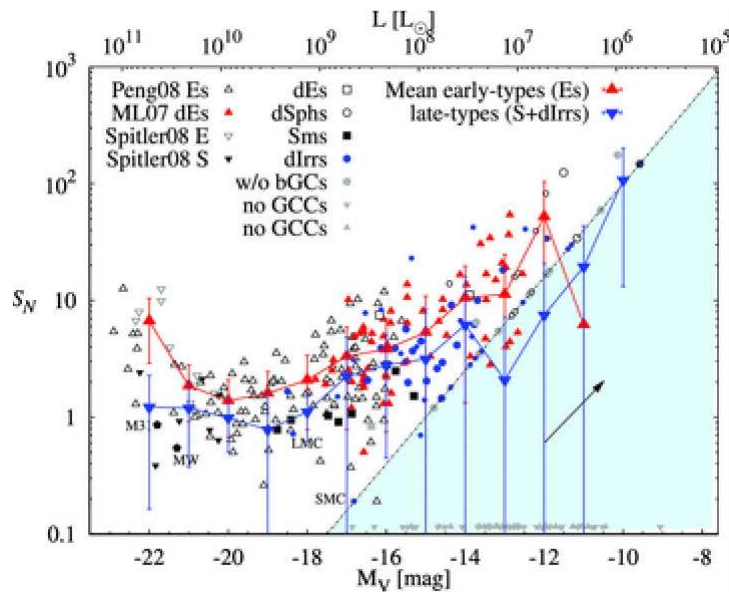
FIGURE 1.9: S_N vs. M_V (luminosity on top axis) for different morphological types. Georgiev et al. (2010)

No correlation between S_N and galaxy luminosity was found, but a dependence with environment was noted (Harris & van den Bergh 1981; Harris 1991). West (1993) found that the mean S_N of ellipticals seemed to be influenced by the local galaxy density. Then, Blakeslee et al. (1997) found a correlation between S_N of BCGs and the velocity dispersion and X-ray luminosity of the cluster, both indicators of cluster mass. They therefore suggested that the number of GCs scales

roughly with the total mass of the galaxy cluster. Since early studies, S_N has been interpreted as a measure of GC formation efficiency (Harris 1991, Forbes et al. 1997). Consequently, Blakeslee et al. claimed that high-S_N galaxies, like M87, are not anomalously rich in GCs but, rather, underluminous as a consequence of the lower overall star formation efficiency within the galaxies in more massive and denser systems (Blakeslee 1999; Peng et al. 2008). McLaughlin (1999) found a similar scaling of S_N in massive ellipticals with the baryonic mass; Blakeslee (1999) showed that the ratio of the scale factors is consistent with the expected baryon fraction. Thus, the GC number per unit total cluster mass shows much less variation than S_N.

Peng et al. (2008) studied S_N and the stellar mass fraction contained in GCs for 100 ACSVCS galaxies. As already shown in Figure 1.9, they found that the GC stellar mass fraction tends to be larger in giant and dwarf galaxies, but is universally low at intermediate masses. Such intermediate mass galaxies also appear to have been most efficient in converting baryons into stars (e.g., van den Bosch et al. 2007; Conroy & Wechsler 2009; Guo et al. 2010). Spitler & Forbes (2009) compiled a sample of galaxies with a wide range of masses in various environments and also concluded that there was a direct proportionality between the mass in GCs and the total halo mass.

Georgiev et al. (2010) studied GC formation efficiencies with an analytical model that includes mass-dependent feedback mechanisms. They found that GC formation efficiency is roughly constant with halo mass, but S_N and stellar mass fraction vary with the field star formation efficiency, which in turn depends on halo mass and is highest at intermediate values.

1.2.2 Color Distribution

GC color distribution has been a diagnostic to test different galaxy formation scenarios. In trying to understand the different S_N values for galaxies with the same absolute magnitude but different morphological type, Ashman & Zepf (1992) suggested that elliptical galaxies formed by the merging of gas-rich spirals (Toomre 1977), forming GCs on the way. They predicted a bimodal GC color distribution

as consequence of this new generation of clusters with different properties than the original ones. This hypothesis was strengthened when, in 1993, Zepf & Ashman found a bimodality in the color distribution in two elliptical galaxies (NGC 5128 and NGC 4472). Then, it was confirmed in M87 using *HST* data (Whitmore et al. 1995). Later on, studies revealed that bimodality in GC optical color distributions was a rule for early-type galaxies (Geisler et al. 1996; Gebhardt & Kissler-Patig 1999; Larsen et al. 2001; Kundu & Whitmore 2001). These color differences could be due to differences in age and/or metallicity. Since most GCs are old (Worthey 1994; Cohen et al. 2003; Puzia et al. 2005), color bimodality is usually attributed to a bimodal metallicity distribution (Brodie & Stradler 2006). Furthermore, in the Milky Way (and other close spirals), spectroscopic studies reveal two populations of GCs with distinct metallicities (Figure 1.10; Zinn 1985, Cohen et al. 1998, Côté 1999; Puzia et al. 2005). These two GC color components are commonly referred to as the metal-poor (blue) and metal-rich (red) subpopulations.
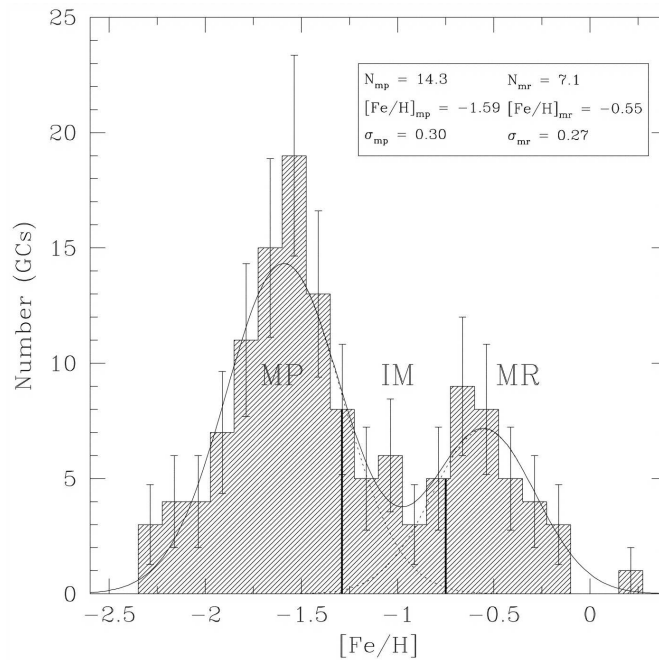

FIGURE 1.10: Metallicity distribution for 133 Galactic GCs with spectroscopic measurements. Côté (1999).

Most studies are biased towards massive ellipticals due to their richness, or to very nearby ones, since they are easier to observe. However, Peng et al. (2006) studied the GC color distributions in 100 early-type Virgo galaxies covering a

wide range of magnitudes (-22< M_B <-15). They found that all massive galaxies show bimodality, while the dwarf galaxies have predominantly blue GCs (i.e., all galaxies have at least metal-poor GCs), and showed that the fraction of metal-rich clusters increases with luminosity of the host galaxy (Figure 1.11).
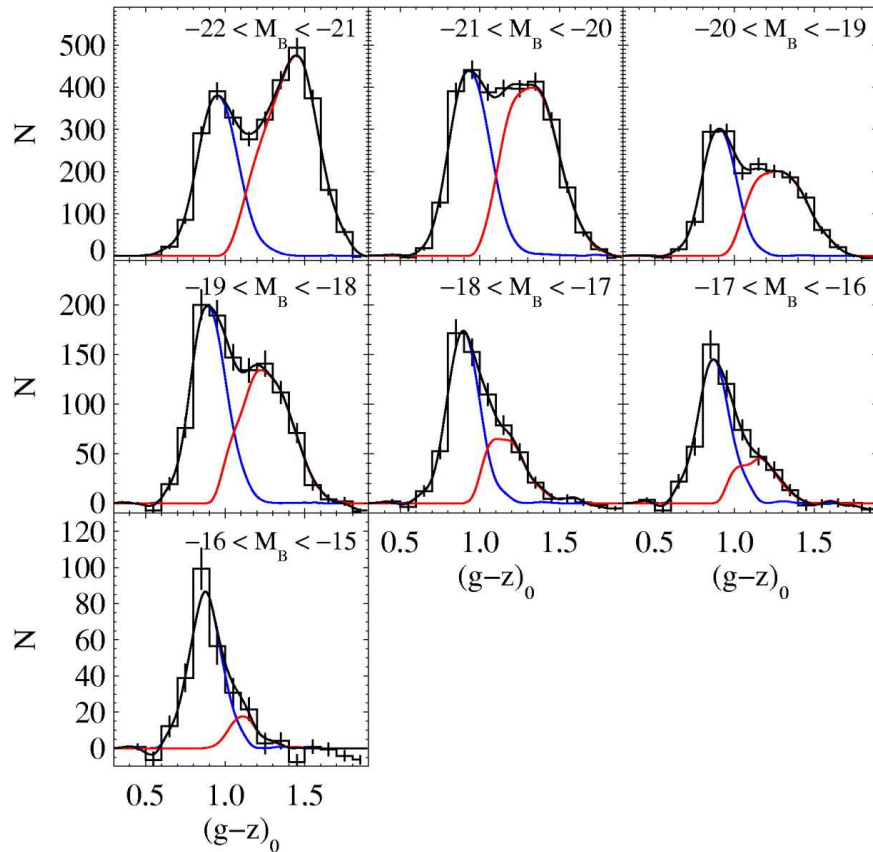
FIGURE 1.11: Color distribution of GCs binned by host galaxy magnitude (histograms). Red and blue curves show the decomposition of red and blue population, respectively. Peng et al. (2006).

As this bimodality seems to be a general property of massive galaxies, galaxy formation scenarios were proposed in order to explain it. When studied in detail, the Ashman & Zepf scenario (primordial metal-poor GCs and metal-rich GCs formed in mergers) failed to reproduce the observations. First, spirals already have these two GC populations (Geisler et al. 1996). Second, with the present GC formation efficiency (Whitmore & Schweizer 1995) it is unlikely to achieve the

S_N values of ellipticals only through mergers, and impossible to explain the high-S_N galaxies with such mechanism (Forbes et al. 1997). However, GC formation efficiency could have been higher in the past. Forbes et al. (1997) suggested a multiphase collapse scenario, *in situ*, where the metal-poor GCs were formed at early epochs, subsequently enriching their surrounding gas. Then, in a later phase of the collapse, the enriched gas formed the metal-rich GCs.

However, the evidence for mergers playing an important role in galaxy formation cannot be ignored, and Côté et al. (1998) proposed an accretion scenario which invokes the mass-metallicity relation (van den Bergh 1975). Here, the metal-poor globulars were formed in low mass galaxies (satellites), while the metal-rich ones were produced in more massive proto-galaxies; then the satellite galaxies were accreted by the latter. This accretion scenario is supported by the discovery of dwarf galaxies with only metal-poor GCs, which are also the ones that tend to have high-S_N values (Miller et al. 1998; Lotz et al. 2004; Peng et al. 2006; Peng et al. 2008). Furthermore, blue GCs have a more extended spatial distribution than red ones.

Moreover, massive early-type galaxies have much larger GC populations than spirals ($\sim$1000-10000 vs. $\sim$200 GCs), and are expected to have more complex formation histories and, consequently, broader metallicity distributions. Interestingly, Yoon et al. (2006) showed that, starting with a broad unimodal metallicity distribution, it is possible to obtain a bimodal color distribution if the color-metallicity transformation is not linear. This started the debate of whether the GC populations of giant ellipticals are really two subpopulations with distinct metallicities.

However, the Galactic GCs are all relatively metal poor and, do not cover the high metallicities observed for giant ellipticals. In order to sample/calibrate a full metallicity range, Peng et al. (2006) plotted together Galactic and extragalactic GCs (from M49 and M87), and confirmed that the relation is indeed non-linear. They showed that the relation of $(g-z)$ color vs. [Fe/H] has an inflection point at $(g-z)\sim$1.05 (Figure 1.12). Just around this inflection point, small variations in metallicity can be reflected as large variations in color and hence apparent bimodality.
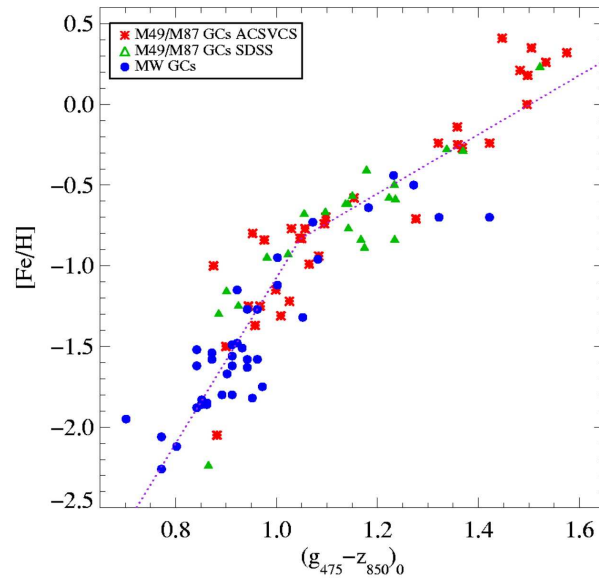
FIGURE 1.12: [Fe/H] vs. $(g-z)$ for Milky Way, M49 and M87 GCs, all with
spectroscopic metallicity. Peng et al. (2006).

The origin color bimodality is still an open question, but for simplicity in the rest
of the text we assume it is due to metallicity bimodality.
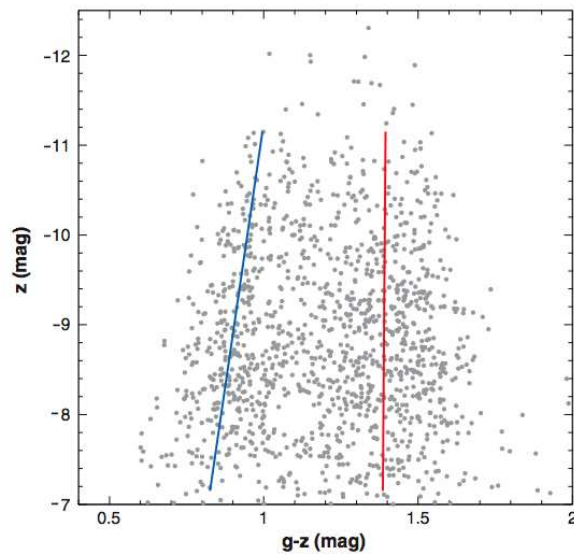
FIGURE 1.13: Color magnitude diagram for M87 GCs. Brodie & Strader (2006).

It is worth mentioning an interesting correlation between color and luminosity
for individual metal-poor GCs: the *blue tilt* (Harris et al. 2006; Strader et al.

2006), also referred to as color magnitude relation. This *blue tilt* (Figure 1.13) has been interpreted as a mass-metallicity relation, possibly a consequence of self-enrichment. This is in agreement with multiple stellar populations within a single cluster (see Section 1.1.5).

1.2.3 Luminosity Function

The uniformity of GC magnitudes was noted since the early studies of GC systems in the Galaxy and the Local Group (Kron & Mayall 1960; Harris 1974). However, it was Hanes (1977) who suggested the existence of a universal GC luminosity function (GCLF, number of GCs per magnitude interval), valid for all galaxy types. He studied the GCLF in 20 Virgo cluster galaxies. Although he sampled only the brightest clusters, the comparison with the GCLF of the Local Group led him to conclude that all have the same form, $\Phi(M)$: a Gaussian distribution.

The parameters that describe the GCLF are the absolute magnitude of the peak or *turnover* (M^0), and the dispersion ($\sigma_{\rm GCLF}$):

$$\Phi(M) = A \exp\{\frac{-(M - M^0)^2}{2\sigma_{\rm GCLF}^2}\}, \tag{1.2}$$

where A is a normalization factor (it represents the richness), and M is the absolute magnitude of each cluster. Harris & Racine (1979), with more and deeper data, confirmed the universality of the GCLF. They estimated $\langle M_{\rm V}^0 \rangle$=-7.3±0.1 and $\langle \sigma_{\rm GCLF,V} \rangle$=1.2±0.05.

Harris et al. (1991), estimated the GCLF parameters for galaxies with different morphological type, luminosity and environment, and found that they are similar but not identical. When Harris et al. compared the values for all the sample ($\langle M_{\rm V}^0 \rangle$=-7.1 and $\langle \sigma_{\rm GCLF,V} \rangle$=1.2) with those for the brightest ones only ($\langle M_{\rm V}^0 \rangle$=-7.3 and $\langle \sigma_{\rm GCLF,V} \rangle$=1.4), they found a dependence on galaxy luminosity.

Although the GCLF parameters vary with galaxy luminosity, they are very homogeneous for giant ellipticals. The turnover magnitude was soon identified as a powerful and simple method to determine distances for faraway elliptical galaxies
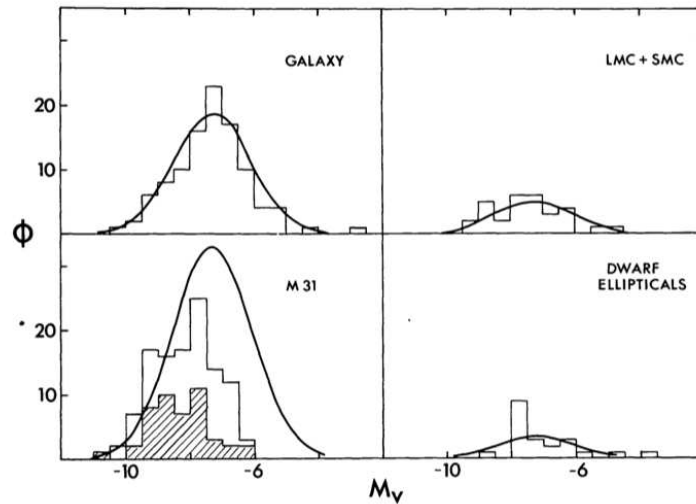
FIGURE 1.14: GC luminosity distributions for Local Group galaxies (histograms). $\Phi(M)$ is the number of GCs in intervals of $0.5\,$mag. The solid curves are scaled Gaussians with M_V^0=-7.3 and $\sigma_{\mathrm{GCLF,V}}$=1.2. Harris & Racine (1979).

(Hanes 1977; Harris 2001; Ferrarese et al. 2000). This was confirmed by Kundu & Whitmore (2001). They used *HST* images to measure the GCLF parameters of 28 elliptical galaxies, and found the values $\langle M_V^0 \rangle$=-7.4 and $\langle M_I^0 \rangle$=-8.5.

Larsen et al. (2001) derived the GCLF for the blue and red subpopulations separately, finding that the turnover magnitude in the V-band of the blue population is brighter than for the red one. This is expected if the two populations have similar ages but different metallicities. They also found that the bright side of the GCLF is similar to the luminosity distribution of young star clusters (Zhang & Fall 1999; Zepf et al. 1999) and giant molecular clouds (Harris & Pudritz 1994), i.e., a power-law with exponent -1.75. Similar luminosity functions (LF) can give insights of the initial conditions of GC formation. However, since they are power-laws, the mass distributions of giant molecular clouds and young massive clusters are dominated by objects with masses smaller than $10^5 M_\odot$, with numbers increasing with decreasing mass. This is inconsistent with the observed number of low mass GCs. Two possible explanations for the different mass distributions of GCs and local massive young clusters are: (1) GCs had initially a wider mass distribution, similar to young ones, but the less massive clusters were destroyed (Fall & Rees 1977); (2) the initial conditions of GC formation were different, and conducive to a narrow mass distribution (Peebles & Dicke 1968).
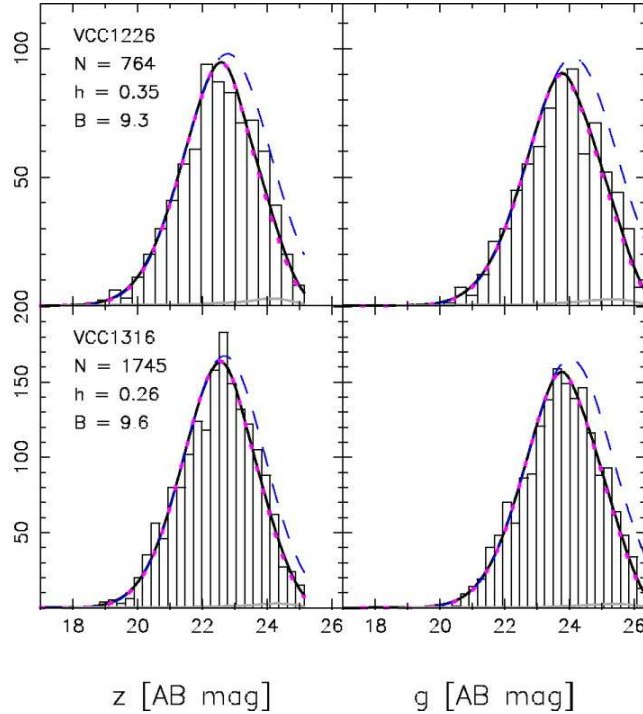
FIGURE 1.15: GCLF for two Virgo galaxies in z (left) and g (right) bands. For each system, the host galaxy name and B magnitude, number of GCs, and bin width (h) are given. Overplotted are the best fit (black solid), intrinsic Gaussian (blue dashed), Gaussian multiplied by completeness (pink dotted), and contaminants (gray solid) curves. Jordán et al. (2007)

The general homogeneity of the GCLF is unexpected *a priori*, given that GC destruction mechanisms should depend on the environment (McLaughlin & Fall 2008). Jordán et al. (2007) constructed the GCLF for 89 galaxies from de ACSVCS and determined their parameters. For each GCLF they derived the mass distribution (or mass spectrum) of GCs, assuming M/L=2 for all. They measured a GCLF turnover, converted to mass, of $\mathcal{M}_{TO}\sim2.2\pm0.4 \times10^5 M_\odot$ for luminous early-type galaxies. On the other hand, they assumed that the mass distribution of young massive clusters is well represented by a Schechter function (see Section 2.1.2). Then, they let the young clusters evolve by evaporation due to dynamical relaxation (see Section 1.1.4). They obtained an evolved Schechter function, with which they fitted the observed mass distribution of GCs. They concluded that the observed variations in the GCLF are due to variations in the initial cluster mass function, rather than to long term dynamical evolution.

1.2.4 Intergalactic Globular Clusters

The existence of intergalactic (or intracluster) starlight (ICL) and its properties are of great importance to test galaxy formation models. ICL and its possible evolution are linked to the evolution of the clusters themselves. However, they are hard to detect, owing to their very low surface brightness. Actually, the debate about the nature of the envelope of cD galaxies (Section 2.1.1) is related to the existence of ICL.

In order to explain the values of the specific frequency for high-S_N galaxies, West et al. (1995) proposed the presence of intracluster globular clusters (IGCs), not bound to individual galaxies but that move through the galaxy cluster potential. They claimed that these high-S_N galaxies have additional GCs due to their privileged position at the cluster center.
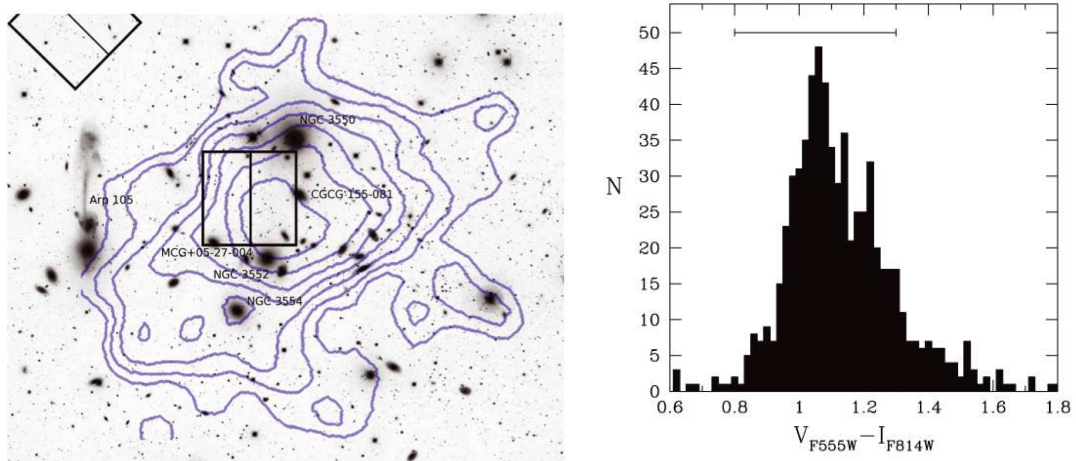
FIGURE 1.16: *Left panel:* galaxy cluster Abell 1185 in optical light; overplotted with contours is the X-ray emission. The boxes indicate the pointing of ACS/*HST* for the detection of IGCs. *Right panel:* color distribution of IGCs in the core of Abell 1185. West et al. (2011).

Indeed, IGCs appear to be a common feature of galaxy clusters: a significant population likely resides in Abell 1185 (Figure 1.16, Jordán et al. 2003; West et al. 2011), a cluster in which the BCG is offset from the centroid of X-ray emission. In the Coma cluster, Peng et al. (2011) found a very large population of IGCs, which are bound to the cluster potential, rather than to individual galaxies. Lee et al. (2010) also report evidence for IGCs in Virgo. Limits on the amount of diffuse

ICL imply a high $S_{\rm N}$ for the IGC population, similar to the values for high-$S_{\rm N}$ cD galaxies and the centrally located Virgo dwarf galaxies.

The IGC populations are overwhelmingly metal-poor (see right panel of Figure 1.16), with colors typical of GCs in dwarf galaxies and the outer regions of massive galaxies. Because of their early formation and subsequent dissipationless assembly, the spatial density profile of the IGCs is expected to trace the total cluster mass profile. However, because of their low surface densities and contamination from GCs bound to galaxies, it remains unclear whether they follow more closely the stellar light, the baryonic matter (including the X-ray gas), or the dark matter distribution. Observations thus far have been limited to nearby ($z \lesssim 0.05$), moderate mass clusters. Further progress requires studying massive galaxy clusters with many thousands of GCs, and well characterized baryonic and total mass density profiles.

Chapter 2

Galaxy Formation and Evolution

Galaxies are like people: The better you get to know them the more peculiar they often seem to become (van den Bergh 1998). It is hard to define the starting point of galactic studies –as it would be trying to pinpoint a single event as the beginning of human history. We find it fair to start with Edwin Hubble, since he set the basis of our definition of galaxies: *stellar systems complete in themselves* (Hubble 1926).

The understanding of what a galaxy is, and of its formation and evolution has been one of the main goals of modern astronomy. Lots of time, effort, and money have been invested in it. During the last decades our knowledge about galaxies has been greatly improved, both observationally and theoretically. However, a general picture that reconciles large and small scales is still missing. Even more, an evolutionary sequence encompassing all the galaxies with their different observed properties has not been established.

2.1 Light Distribution

Once *extra-galactic nebulae* (galaxies) were recognized as stellar systems (Hubble 1926), their intrinsic sizes, distances, and morphologies started to be investigated. Only four are visible to the naked eye: M31, M33, the Large Magellanic Cloud (LMC), and the Small Magellanic Cloud (SMC); however with the magnification

27

offered by the telescope, thousands were found. A natural start to the study of a sample of unknown objects is their classification. Hubble studied photographic images, from which he identified 400 galaxies and classified them based on their morphology. He proposed three main classes: ellipticals (E), spirals (S), and irregulars (Irr). This morphological arrangement, the *Hubble tuning fork*, was interpreted as an evolutionary sequence where the ellipticals evolved into spirals, and hence called "early-type" and "late-type", respectively. This classification was revisited, among others, by Kormendy & Bender (1996), who claimed that Hubble's classification of elliptical galaxies was not indicative of different fundamental properties. Instead, they proposed to classify E galaxies, according to their isophotal shapes, into *disky* and *boxy*. This was based on the fact that ellipticals with disky isophotes have normal to low luminosity and fast rotation, whereas ellipticals with boxy isophotes show high luminosity and slow rotation.
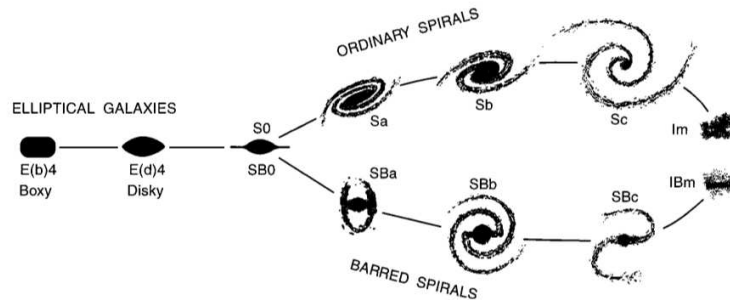
FIGURE 2.1: Revisited version of the Hubble tuning fork. Kormendy & Bender (1996).

2.1.1 Surface Brightness Profiles

de Vaucouleurs (1948, 1959) studied the light distribution of galaxies, and found that the surface brightness ($\mu_{\rm SB}$) radial profile of early-type galaxies (and spiral bulges) is well represented by a power-law ($\mu_{\rm SB} \propto r^{1/4}$). Sérsic (1968) introduced a more general form that describes early and late type galaxies, with $r^{1/n}$ instead of $r^{1/4}$:

$$I(r) = I_{\rm e} \exp\left\{-b_{\rm n}\left[\left(\frac{r}{R_{\rm e}}\right)^{1/n} - 1\right]\right\} , \tag{2.1}$$

where R_e is the effective radius that encloses half of the light; I_e is the effective intensity at R_e; n is the Sérsic index, which indicates the slope; and $b_\mathrm{n} \approx 1.9992n - 0.3271$ (Graham & Driver 2005). Larger n values indicate a more extended light distributions (for a fixed R_e). For example, for an exponential profile (n=1, a good description of disks), 99.1% of the flux resides within the inner $4R_\mathrm{e}$, whereas for an n=4 profile (de Vaucouleurs law), 84.7% of the flux is enclosed by the inner $4R_\mathrm{e}$ (Graham & Driver 2005). However, it is important to note that a degeneracy exists between n and R_e.

In general, the Sérsic profile is a good representation of the global galaxy light distribution. However, high spatial resolution studies of μ_SB profiles have revealed departures from the Sérsic function. The most luminous (boxy) ellipticals often show central deficits, or *cores*, with respect to the inward extrapolation of the best-fit Sérsic models, while intermediate-luminosity (disky) early-type galaxies are generally well described by Sérsic models at all radii (Ferrarese et al. 2006). Even more, fainter early-type dwarf galaxies tend to possess central excesses, or *nuclei* (Figure 2.2, Côté et al. 2007).

In order to fit the most luminous ellipticals, Trujillo et al. (2004) proposed a function composed of an inner power law plus an outer Sérsic function. It is referred to as *core-Sérsic* :

$$I(r) = I_b 2^{-(\gamma/\alpha)} \exp\left[b \left(2^{1/\alpha} \frac{R_b}{R_\mathrm{e}} \right)^{1/n} \right] \tag{2.2}$$

$$\times \left[1 + \left(\frac{R_\mathrm{b}}{r} \right)^\alpha \right]^{\gamma/\alpha} \times \exp\left\{ -b \left[\frac{R^\alpha + R_\mathrm{b}{}^\alpha}{R_\mathrm{e}{}^\alpha} \right]^{1/(\alpha n)} \right\} ,$$

where R_b is the break radius (transition point between Sérsic function and inner power-law), I_b is the intensity at R_b, α indicates how sharp the transition is, and γ is the slope of the inner component. This deficit of light in core-Sérsic galaxies is explained as the product of a dry (i.e., without gas and therefore without star

formation) major merger of two galaxies, each one with a super massive black hole (SMBH). Then, the SMBHs orbit each other while sweeping material from the center.

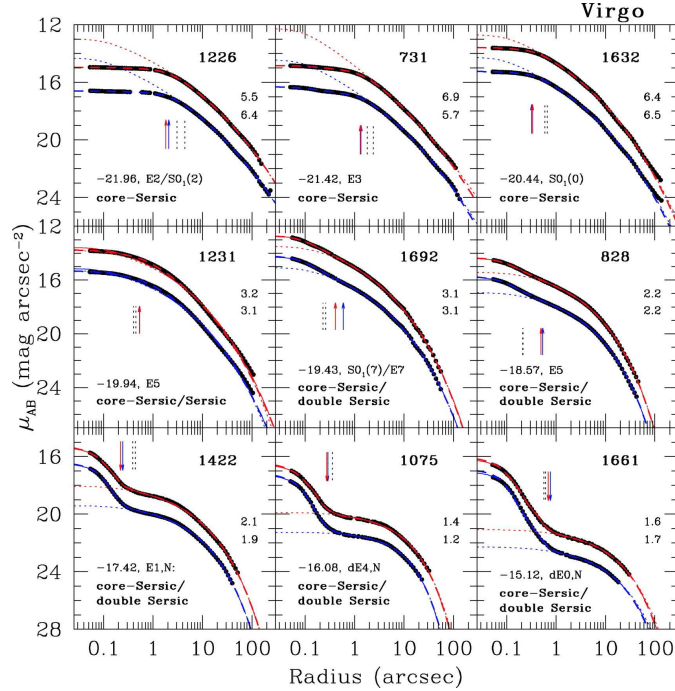FIGURE 2.2: Surface brightness profiles in the g and z ACS/WFC filters for 9 representative Virgo cluster galaxies. Côté et al. (2007).
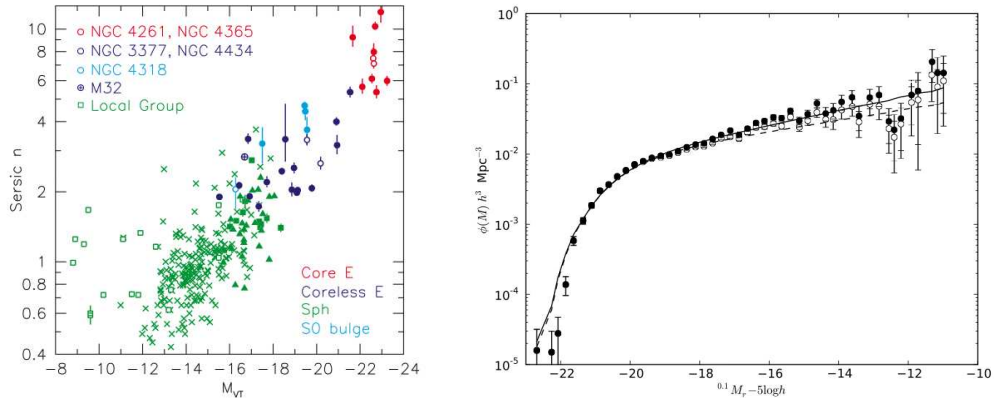

FIGURE 2.3: *Left panel:* Sérsic index, n, vs. visual absolute magnitude. Kormendy et al. (2009). *Right panel:* Luminosity function for galaxies with $z < 0.1$ from the Galaxy and Mass Assembly survey (dots); the solid line shows the best Schechter function. Loveday et al. (2012).

Departures from fitted profiles at large radii also have been seen. A cD galaxy is defined as a giant elliptical with an extended envelope; such an envelope is detected as an upward departure from the de Vaucouleurs $r^{1/4}$ profile at large radii (Oemler 1976; Schombert 1988). However, in a Sérsic framework, cD galaxies may be described as giant ellipticals with high Sérsic index values ($n > 4$), which are characterized by extended, low surface brightness outer profiles. Since Sérsic index correlates with luminosity (see left panel in Figure 2.3), BCGs are more likely to show excesses with respect to an $r^{1/4}$ law, and be classified as cDs. However, Seigar et al. (2007; see also Donzelli et al. 2011) found that some BCGs are surrounded by large-scale stellar envelopes in excess of the best-fitting Sérsic model, possibly associated with ICL stripped off from the general galaxy population.

Notwithstanding the structural differences in the inner regions of early-type galaxies, global properties seem very uniform. Djorgovski & Davis (1987) found that the velocity dispersion, $R_{\rm e}$, and $\mu_{\rm e}$ of early-type galaxies in a wide range of luminosities describe a plane, the *fundamental plane*. Also, there is a correlation between luminosity and Sérsic index n (left panel in Figure 2.3. Ferrarese et al. 2006; Kormendy et al. 2009). This continuity in their properties has been interpreted as a consequence of similar formation processes.

2.1.2 Luminosity Function

One basic property of the galaxy population is its luminosity distribution (or luminosity function, LF), i.e., the number of galaxies per luminosity interval per unit volume. The LF may be determined by the physical processes responsible for galaxy formation and evolution. Schechter (1976) proposed an analytical expression for the LF, the so-called *Schechter* function, with the form:

$$\Phi(L) = \left(\frac{\Phi^*}{L^*}\right)\left(\frac{L}{L^*}\right)^{\alpha}\exp(-L/L^*) , \qquad (2.3)$$

where L^* is a characteristic luminosity at which the distribution starts to decrease exponentially, α is the slope in the low-luminosity region, and Φ^* is the normalization value of Φ at L^*. The local L^* corresponds to a mass of $\sim 10^{12} M_{\odot}$. The LF

has been determined with hundreds of thousands of galaxies from the Sloan Digital Sky Survey (SDSS), and has been found to vary with redshift and filter (Blanton et al. 2003; Loveday et al. 2004). Actually, the Schechter function is a good representation of the global galaxy population, but not of individual morphological classes. Loveday et al. (2012) determined the luminosity function of low-redshift ($z < 0.1$) galaxies over more than 10 magnitudes (right panel of Figure 2.3), and found that it is well represented by a Schechter function.

2.2 Galaxy Content

In 1944, Baade discovered that the CMDs of early and late-type galaxies are different. Hence they are not only morphologically different, but their stellar content is disparate as well. Baade defined population-I as composed of young Solar neighborhood type stars, and population-II composed of old globular cluster type stars. Irregular galaxies and disks contain population-I stars, while spheroidals (ellipticals, spiral bulges and halos) are population-II objects. However, the spectra of spiral bulges revealed a dominant old, metal-rich population (Morgan & Mayall 1957; van den Bergh 1971), unlike GC stars, which are old and metal-poor. On the other hand, radial gradients of ages and metallicities are observed within galaxies (Peimbert 1968; van den Bergh 1975).

Morgan & Osterbrock (1969) studied the spectra of galaxies with different morphological types, and confirmed that galaxies have different mixtures of stellar populations. The relative abundance of each stellar population is important, since it is reflected in the global properties (e.g., surface brightness, chemistry, and M/L values). Most of the total stellar mass is contained in low-mass stars, whereas the luminosity is provided mainly by high-mass stars; both intermediate mass and massive stars change the chemistry of the interstellar medium. Thus, the sampling of the stellar populations that compose galaxies is crucial to reconstruct their history.

2.2.1 Initial Mass Function

The relative abundance of each stellar type is defined by the stellar luminosity function, or mass function. Salpeter (1955) studied the luminosity function of Solar neighborhood stars and reconstructed their initial mass function (IMF, the number of stars per mass interval formed in a single event). Salpeter found that the mass distribution in the range ∼0.4 - 10$M_\odot$ is well described by a power-law with index $\alpha = -2.35$, with the number of stars increasing for lower masses. Kroupa (2001, 2002) sampled the IMF with a wider range of masses: from brown dwarfs (∼0.07$M_\odot$) to massive stars (∼70$M_\odot$). He found that the index α varies with the stellar mass as α=-0.3, -1.3, and -2.3 for $M<0.08M_\odot$, 0.08<M<0.5$M_\odot$, and M>0.5$M_\odot$, respectively. At the same time, Kroupa found this shape to be very uniform across different environments, from stars just forming in small and giant molecular clouds, to ancient and metal-poor populations. Chabrier (2003) estimated the IMF in the Galactic disk and halo, and for open and globular clusters; he found that best descriptors are a log-normal function for M<1$M_\odot$, and a power-law for M>1$M_\odot$, but confirmed that the IMF is the same in the different environments he studied. However, theoretically it is expected that the IMF should vary with environment, since fragmentation depends on the physical conditions of the initial cloud (Larson 2005).

Interestingly, van Dokkum & Conroy (2010) estimated the IMF in giant ellipticals through their spectra, and detected absorption features that indicate a large population of low mass stars (M<0.3$M_\odot$). Using stellar models, they concluded that those spectral features correspond to a power-law IMF with α <-2.3, i.e., a *bottom-heavy* function, but steeper than the local one. Also, they found a dependence of α with the mass and metallicity of the galaxy, where the most massive and metal-rich galaxies have a higher fraction of low-mass stars. Thus, this variation in the IMF might be an indication of a dependence of galaxy properties on their initial conditions.

However, galaxies are not only made up of stars. These systems also comprise gas (in different phases), dust, and dark matter.

2.2.2 Dark Matter

One of the most accurate methods to determine masses in stellar systems (clusters, galaxies, and groups of galaxies) is to measure motions of their stars, or any other baryonic component. Because the dynamics of the system is governed by the gravitational potential, the mass measured through this method is called *dynamical mass*. However, an easier way to estimate the mass is to measure the total luminosity and multiply it by a stellar-mass-to-light ratio ($\mathcal{M}_\star/L$) for a certain IMF, age, and metallicity; this estimation is called *luminous mass*. The dynamical and luminous masses differ for galaxies and groups of galaxies. This was first reported by Zwicky (1937), who measured the dynamical and luminous masses for the Coma cluster, and noticed that the luminous mass was insufficient to avoid expansion when compared to the velocity dispersion of the galaxies. He suggested that there must be *dark matter* in the form of cold stars.

Although $\mathcal{M}_\star/L$ values vary with the properties of the stellar population, the observed global M/L for galaxies and groups of galaxies ($\sim$100-300, Page 1952, 1960; Rood et al. 1972) are too high to be explained only with known low-mass stars and fading due to evolution. Even more, the discovery that the rotational curves of spirals do not decrease as expected from the drop of the disk luminosity (Figure 2.4, Rubin & Ford 1970; Rubin et al. 1980) strengthened the evidence for non-luminous matter. Thus, the very high values of M/L in galaxies, groups and clusters are attributed to dark matter.
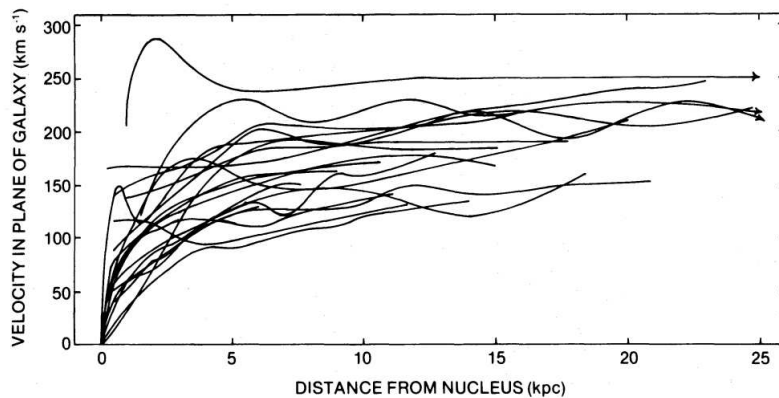

FIGURE 2.4: Rotational velocity curves for 21 spiral galaxies. Rubin et al. (1980).

The fact that the cumulative mass continues to increase faster than the cumulative luminosity with radius, indicates that the dark matter distribution is extended (Rubin et al. 1980). Ostriker et al. (1974) claimed that this extended distribution is similar to the outer parts of an isothermal sphere composed of dark mass points, and that the observed galaxies could be embedded within these spheres or *halos*. Ostriker & Peebles (1973) found that, in fact, disk structures can be easily affected by large scale instabilities, unless they are embedded within massive halos.

Although there is X-ray emission from hot gas in intergalactic regions (Forman et al. 1972), and the hot gas masses are larger than the stellar ones (Cavaliere & Fusco-Fermiano 1976; Gorenstein et al. 1978; Jones & Forman 1984), luminous mass is still much smaller than the dynamical mass.

The fact that the mass distribution is not necessarily predicted by the light distribution (Burstein & Rubin 1985) captured the attention of the extragalactic community, and galaxy formation models including massive halos were proposed (Blumenthal et al. 1986). Blumenthal et al. (1984) propounded an alternative nature for the dark matter: collisionless particles with low velocity dispersion (*cold* particles), that are able to form small scale structures.

Subsequently, more accurate measurements of the total mass within galaxy clusters using the technique of gravitational lensing confirmed the existence of large amounts of dark matter. Tortora et al. (2009) found a strong dependence of the total M/L with mass, in the sense that more massive systems have larger fractions of dark matter. Interestingly, it has been observed that colliding galaxy clusters have their X-ray gas displaced from the bulk of the dark matter, estimated from strong (highly distorted arcs and multiple images of background galaxies) and weak (weakly distorted background galaxies) gravitational lensing (Figure 2.5, Clowe et al. 2006; Bradač et al. 2008). This is explained if dark matter particles are collisionless, whereas the X-ray gas collides and experiences ram pressure; such observations are taken as a strong evidence of the existence of cold dark matter.

FIGURE 2.5: *HST* optical image shows the two galaxy clusters colliding. Overplotted are the X-ray gas (pink) and the gravitational lensing derived mass map (blue). *Left panel:* Bullet cluster; X-ray(NASA/CXC/CfA/M.Markevitch et al.); optical/lensing(NASA/STScI Magellan/U.Arizona/D.Clowe et al.). *Right panel:* galaxy cluster MACS J0025.4-1222; X-ray(NASA/CXC/Stanford/S.Allen); optical/lensing(NASA/STScI/UC Santa Barbara/M.Bradač).

2.3 Galaxy Formation Scenarios

The physical processes that play a role in setting galaxy properties are: minor and major mergers, gas accretion, and feedback from stellar winds, supernovae (SN), and active galactic nuclei (AGN). However, the reason why we do observe such different and diverse configurations at the same epoch (dwarf irregulars, spirals, giant ellipticals, etc.), whether it is the environment or different initial conditions that have more influence on the future galaxy, is still unclear.

Basically, two general scenarios have been proposed to explain galaxy formation: (1) monolithic collapse and (2) hierarchical assembly. Both have evolved since they were proposed. Incidentally, GC properties are crucial to discern between both scenarios.

2.3.1 Monolithic Collapse

The monolithic collapse model propounds that larger structures form first, and through fragmentation give origin to smaller structures, *top-down.*

Eggen et al. (1962) found that the oldest (lowest metallicity) stars in the Galaxy have the most eccentric orbits (and are located farther away from the Galactic center), in comparison to the circular orbits of the youngest ones. They interpreted this as evidence for a protogalactic cloud collapse, where the falling gas moved nearly radially from the outer regions to the center, forming on the way the first generation of stars (GC-type stars, with high eccentricities). Then, the collapse was eventually stopped by rotation and the remaining gas settled into circular orbits. A second generation of stars was formed from this metal-contaminated disk of gas. Under the same general idea, Partridge & Peebles (1967) proposed a detailed model where ellipticals were the result of a single intense burst of star formation, followed by passive evolution.

Searle & Zinn (1978) studied the metal abundance of GCs located at different galactocentric radii, and did not find any radial abundance gradient, being in contradiction with the predictions of a monolithic collapse model. Thus, they suggested a different galaxy formation model, one where GCs formed in protogalaxies that subsequently merged to form the present halo.

2.3.2 Hierarchical Assembly

In the hierarchical scenario smaller structures form first and then merge to construct larger structures, *bottom-up.*

Peebles & Dicke (1968) determined the properties of the first gas clouds able to collapse by their own gravity, the ones that exceed the critical Jeans mass. They claimed that the first bound systems had masses similar to those of present-day GCs. Based on the outstanding homogeneity of GC systems belonging to such a different galaxies, they argued that GCs may have formed before galaxies, under universal conditions. However, correlations between GC systems and parent galaxy

properties are inconsistent with this model. Fall & Rees (1985) argued that GCs formed during the collapse of protogalaxies.
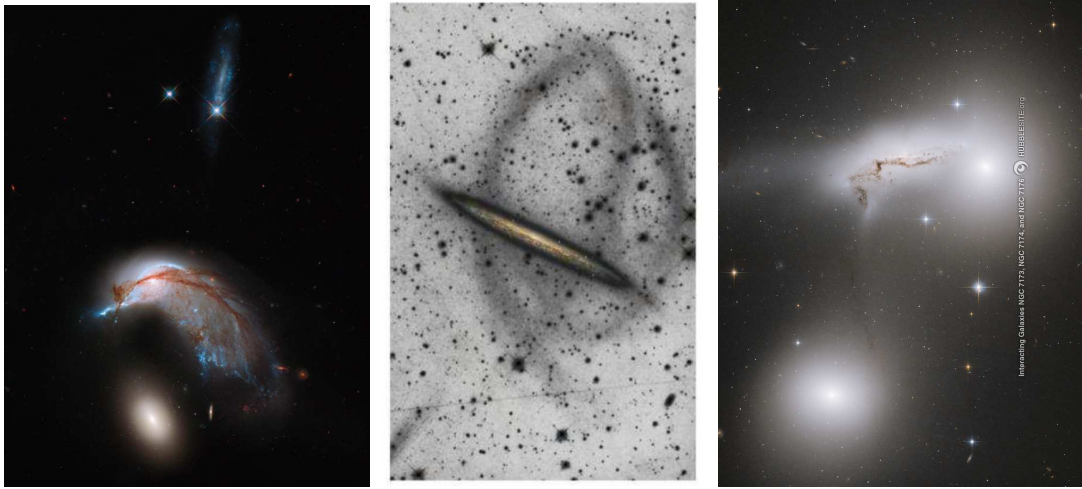
FIGURE 2.6: *Left panel:* Arp 142; credit: NASA, ESA, and the Hubble Heritage Team (STScI/AURA). Middle panel: NGC 5907, Martínez-Delgado et al.(2008). *Right panel:* Hickson Compact Group 90; credit: NASA, ESA, and R. Sharples (University of Durham).

The hierarchical scenario is strongly supported by the frequent observation of minor and major mergers, and of signatures of galactic encounters: shells, bridges, and tails (dynamical disruptions, Toomre & Toomre 1972). Furthermore, studies of the relative frequency of early and late type galaxies in different environments show a relation between galactic density and morphology (Dressler 1980). In the richest environments the fraction of early-type galaxies increases. This fact supports the hierarchical model, where ellipticals are formed through the merger of other galaxies. Furthermore, the most massive giant ellipticals are found in the densest regions (centers of massive galaxy clusters). Actually, clusters with cD galaxies are denser, have a larger fraction of ellipticals, and show a more spherical symmetry (Oemler 1974).

2.4 Standard Paradigm

The most accepted model for the formation of structures is a hierarchical assembly in a universe composed of baryons, cold dark matter and dark energy, the ΛCDM paradigm.

According to this model the structures in the universe were created from density fluctuations at very early epochs. Just after the Big Bang, the whole universe was a very hot plasma. As the universe expanded, it cooled, and recombination occurred. Atoms were formed and photons were released. At this point, baryonic density fluctuations started growing. The effective temperature of the released radiation continues to decrease with the expansion. This radiation was detected for the first time by Penzias & Wilson (1965) in the microwave regime of the electromagnetic spectrum, thus it was called the Cosmic Microwave Background (CMB). However, the measured amplitude of the CMB fluctuations ($\sim 10^{-5}$) is smaller than the one required theoretically ($\sim 10^{-3}$) to form the large structures we observe today if all matter is baryonic. Moreover, the exact moment when these fluctuations were created is not well understood.

The problem of the small amplitude can be solved if non-baryonic particles (dark matter) are included in the model. Density fluctuations from non-baryonic particles could be formed even before the recombination epoch; they could have started as quantum fluctuations that grew to macroscopic scale in an epoch called *inflation*, when the universe expanded exponentially. The observation of the CMB and, furthermore, the detection of temperature fluctuations (manifestation of the density inhomogeneities) are both taken as strong observational evidence in favor of this model.

Once the density inhomogeneities were created, they started to coalesce to form progressively larger structures (e.g., Press & Schechter 1974). Galaxies were formed in the centers of these halos by the cooling of gas, which then fragmented to form stars (White & Rees 1978). The halos aggregated to give origin to groups and clusters of galaxies. Numerical simulations have been used to test and support the theory of structure formation (Springel et al. 2005; De Lucia et al. 2006). These simulations have shown a matter distribution very similar to the observed

spatial distribution of galaxies (Springel et al. 2006), which on large scales appears homogeneous and isotropic.

On the other hand, the modeling of the light distribution of galaxies involves many assumptions and simplifications. Basically, a universal baryonic fraction is assigned to each dark matter halo. Then these baryons are converted to stellar mass assuming a certain star formation efficiency and an IMF. UV ionization background, supernovae, and AGN effects are taken into account (decreasing the baryon fraction mainly for the low mass halos).

Unfortunately, the predictions for the luminous properties of galaxies fail to reproduce the observations. The form of the galaxy LF is an important tool to test the models; imprinted in it are the physical processes of galaxy formation and evolution, i.e., the ability to retain/accrete gas, and its cooling to form stars. The theoretical LF determined from dark matter halos shows an excess of bright and faint galaxies (if matched to the observed one at L^*, Silk & Mamon 2012). It has been suggested that feedback by SN (at small scales) and AGN (at large scales) heats the gas and suppresses star formation.

On the other hand, the hierarchical model predicts that small galaxies are formed prior to giant ones, but observations show the contrary. The most massive galaxies are dominated by old stellar populations. This is called *downsizing* (Cowie et al. 1996), meaning that the most massive galaxies form their stars earlier (and faster) than small ones. Ellipticals show high $[\alpha/\text{Fe}]$ values, indicating short time scales for star formation. The α-elements are attributed to SN type-II (very massive stars that have short lifetimes) while the Fe abundance is due mainly to SN type Ia (product of low mass binaries with longer lifetimes). Thus, the ratio $[\alpha/\text{Fe}]$ is a clock for star formation.

We must have in mind that the stellar formation time and the assembly time could be different. De Lucia et al. (2006) studied the star formation histories in numerical simulations and found that, indeed, elliptical galaxies in dense environments have older stellar populations and shortest formation timescales. They claimed that high density regions originate from the highest density peaks in the primordial fluctuations, and thus had an earlier collapse, reflected as an *accelerated* evolution.

On the other hand, they also found that these massive galaxies have long timescales for their assembly.

This assembly time is still in contradiction with observations. Collins et al. (2009) found that BCGs have already assembled most of their mass ($\sim$90%) at high redshift ($z\sim$1.3), while according to simulations the assembled mass should be only 22% at that time. They suggested that these giant ellipticals had a rapid growth rather than an extended hierarchical assembly.

Although observational evidence supports the ΛCDM model, some discrepancies between the predictions and the observations still remain, e.g., the number of satellites problem (Boylan-Kolchin et al. 2011, 2012) and the core/cusp problem (de Blok 2010; Oh et al. 2011).

2.5   This Thesis

Summarizing, in the last decades our knowledge of how galaxies form and evolve has grown exponentially. However, a general picture that reconciles large and small scales, as well as baryonic and non-baryonic mass, is still missing. We have seen that the luminous mass does not dominate, and does not even trace the bulk of the total mass in the universe. Thus, in order to understand galaxies, we must first find a reliable tracer of the dark matter.

Guo et al. (2010) estimated the stellar formation efficiency as a function of the dark matter halo mass, and found that baryons are converted into stars with different efficiencies, depending on the halo mass. The efficiency is higher for intermediate mass galaxies. This is in agreement with the behavior of S_N for different galaxy types (which tends to be larger in dwarf and giant galaxies, but is universally low for intermediate mass galaxies), if the mass in GCs scales with the underlying total mass (Blakeslee 1999; Peng et al. 2008). Furthermore, observational evidence shows that the spatial distribution of GCs is more extended than the starlight, suggesting that they follow the dark matter distribution. High-resolution numerical simulations indicate that old metal-poor GCs and diffuse stellar light provide

reliable tracers of the earliest star-forming substructures (Moore et al. 2006; Abadi et al. 2006), including their spatial distributions and kinematics.

On the other hand, globular clusters are appealing tracers of galaxy structure, as well as indicators of formation mechanisms. These systems are very old ($>10\,\mathrm{Gyr}$), and so they have imprinted on them the initial conditions of galaxy formation. Furthermore, since GCs are very dense stellar systems (10^3-$10^5 M_\odot\,\mathrm{pc}^{-3}$), they can survive galactic mergers and interactions without being disaggregated. GCs are also easily identifiable in faraway galaxies, thanks to their compactness and brightness (typical magnitudes of $M_V = $ -7.2 mag). Most galaxies have GCs, from giant ellipticals to dwarf irregulars.

In this doctoral thesis I study the properties of GC populations (N_{GC}, S_{N}, spatial distribution, GCLF, and color distribution when possible) in extreme systems, in order to find clues about how large structures, such as giant elliptical galaxies, were assembled. By extreme environments I mean fossil groups (described in Chapter 3), and the center of the massive galaxy cluster Abell 1689 (described in Chapter 4). These systems are large, dense, distant, and represent a link between regular galaxies and galaxy clusters.

Chapter 3

Fossil Groups

3.1 Description

The hierarchical model is supported by the frequent observation of galactic interactions, and predicts that all the galaxies within a galaxy group or cluster will eventually merge into a single massive elliptical galaxy; this would be the last step of galaxy formation (Section 2.4).

Indeed, Ponman et al. (1994) found an extreme system consisting of a giant elliptical galaxy surrounded by dwarf companions, all immersed in an extended X-ray halo. Due to dynamical friction (see Section 1.1.4) the most massive galaxies will be disrupted before the small ones. This system was interpreted as the end product of the merger of galaxies within a group, and was thus called a fossil group (FG). A formal definition was introduced by Jones et al. (2003), according to which FGs are systems with $L_{\mathrm{x}} \geq 10^{42} h_{50}^2 \mathrm{erg \ s^{-1}}$, and an optical counterpart where the difference in magnitude between the first and the second brightest galaxies is $\Delta m_R > 2$ mag. Because of their regular X-ray morphologies and lack of obvious recent merger activity, FG galaxies are usually considered to be ancient and unperturbed systems (Khosroshahi et al. 2007). This is supported by numerical simulations that suggest FGs formed at early epochs ($z > 1$) and afterwards evolved fairly quiescently (D'Onghia et al. 2005; Dariush et al. 2007; Díaz-Giménez et al. 2011).
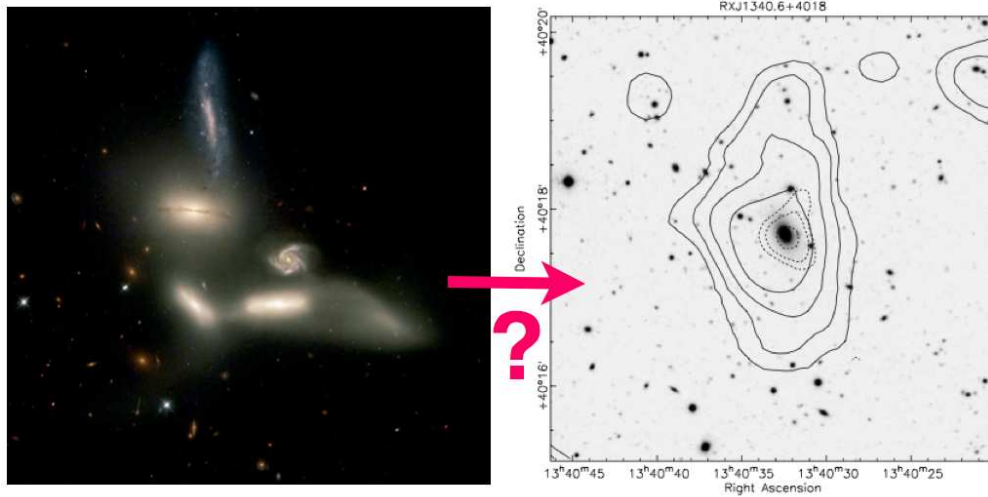
FIGURE 3.1: Left: Seyfert's Sextet. Image Credit: NASA, J. English (U. Manitoba), S. Hunsberger, S. Zonak, J. Charlton, S. Gallagher (PSU), and L. Frattare (STScI). Right: fossil group RXJ1340.6+4018. Optical image from Isaac Newton 2.5m Telescope with overplotted contours of ROSAT X-ray emission. Jones et al. (2003).

At present, there is no consensus about the M/L values of FGs; measurements span from $\sim 100 M_\odot/L_\odot$ (Khosroshahi et al. 2004) to $\sim 1000 M_\odot/L_\odot$ (Vikhlinin et al. 1999; Yoshioka et al. 2004; Cypriano et al. 2006) in the R-band, but there is a tendency towards higher values (Proctor et al. 2011; Eigenthaler & Zeilinger 2012). Such high M/L values, together with the fact that FGs show unusually high L_X/L_{opt} ratios compared with typical galaxy groups (Figure 3.2), appear inconsistent with the assumption that FGs are formed by the merging of the members in ordinary galaxy groups (Khosroshahi et al. 2007). Compact galaxy groups in the nearby universe tend to have lower masses and X-ray luminosities than those observed in FGs, although there is evidence that high-mass compact groups may have been more common in the past and could represent the progenitors of today's FGs (Mendes de Oliveira & Carrasco 2007). In addition, the optical luminosities of the dominant giant ellipticals in FGs (Khosroshahi et al. 2006; Tovmassian 2010) are similar to those of BCGs. For these reasons, it has been suggested that FGs are more similar to galaxy clusters, but simply lack other early-type galaxies with

luminosities comparable to that of the central galaxy (Mendes de Oliveira et al. 2009).
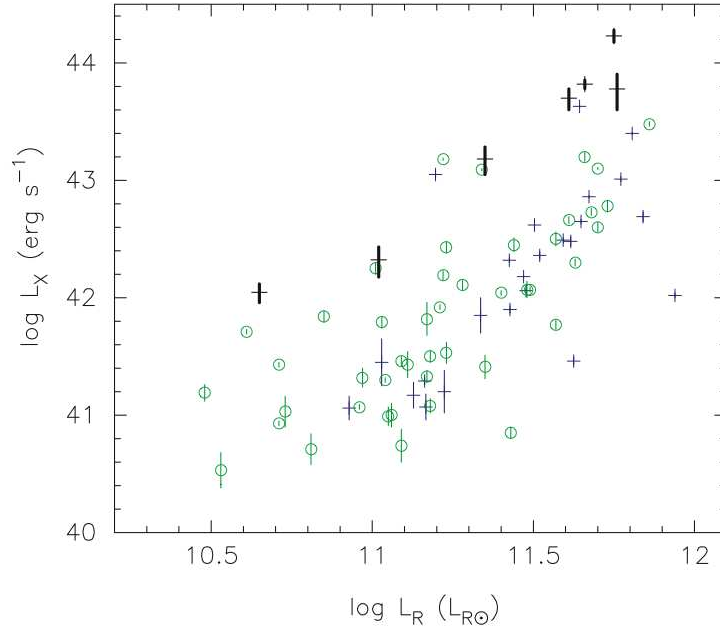
FIGURE 3.2: L_X- L_R relation for galaxy groups (green circles and blue crosses) and fossil groups (bold crosses). Khosroshahi et al. 2007

It remains an open question whether FGs represent the final phase of most galaxy groups, or if they constitute a distinct class of objects which formed with an anomalous top-heavy luminosity function (Jones et al. 2000; Cypriano et al. 2006; Cui et al. 2011; see also Méndez-Abreu et al. 2012).

Hence, given that FGs appear to be ancient, highly luminous, but relatively unperturbed systems with origins that remain poorly understood (identified less than two decades ago), we propose to study for the first time the GC populations of the dominant elliptical, and compare with GC properties from galaxies in different environments.

3.2 The Sample

In order to have a representative sample we choose: the nearest, NGC 6482 ($z = 0.013$); the prototype, NGC 1132 ($z = 0.023$); and the most massive known to date, ESO 306-G017 ($z = 0.036$).

Throughout this chapter, we adopt a ΛCDM cosmology with $H_0 = 71$ km s^{-1}Mpc^{-1}, Ω_{m}=0.27, and $\Omega_\lambda = 0.73$, unless it is indicated otherwise. Right ascention (RA) and declination (DEC) are in J2000.

3.2.1 NGC 6482

FIGURE 3.3: Fossil group NGC 6482. Left: optical ACS/HST RGB image, FOV$\sim 3'.3 \times 3'.3$. Right: optical DSS image with Chandra X-ray contours of the disffuse emission, FOV $8' \times 8'$ (Khosroshahi et al. 2004).

NGC 6482 (RA:17h51m48.8s , DEC:+23°04'19'') is the nearest known FG, located at a distance of 56 Mpc. The optical light is dominated by a giant elliptical with R-band luminosity L_{R}=4.46$\times10^{10}L_\odot$. Another four confirmed members are all at least two magnitudes fainter than the giant elliptical, satisfying Jones et al. (2003) criteria.

This system was studied in detail by Khosroshahi et al. (2004). Using Chandra data, they determined that the X-ray emission shows an extended and relaxed

morphology, with a total luminosity $L_X = 1.1 \times 10^{42}\,\mathrm{erg\,s^{-1}}$, R-band M/L=71, and total mass M_{200}=4×$10^{12}M_\odot$. M_{200} is the mass within a radius (r_{200}) where the density of the system is 200 times the critic density of the universe (ρ_c); for NGC 6482 $r_{200}\approx 310\,\mathrm{kpc}$. They also found a mass profile that is centrally peaked.
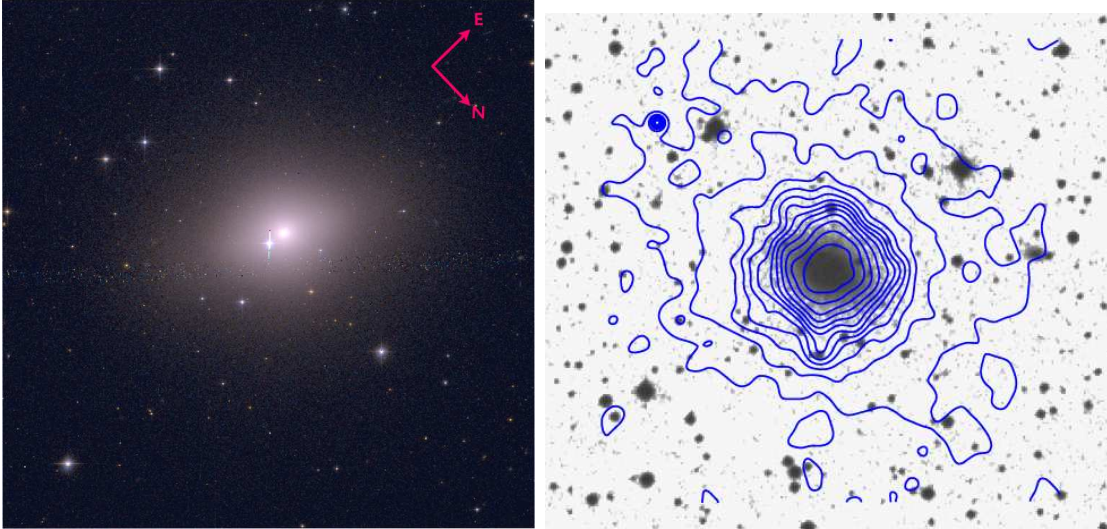
3.2.2   NGC 1132

FIGURE 3.4: Fossil group NGC 1132. Left: optical ACS/HST RGB image, FOV$\sim$ 3′.3 × 3′.3. Right: optical DSS image with ASCA X-ray contours of the disffuse emission, FOV 1° × 1° (Mulchaey & Zabludoff 1999).

NGC 1132 (RA:02h52m51.9s , DEC:-01°16′29″) is known as the prototypical FG. It is located at a distance of 100 Mpc, and it is composed of a giant elliptical with a population of dwarf galaxies. This system was first identified by Mulchaey & Zabludoff (1999), when they were looking for merger remnants of galaxy groups. They found an extended X-ray distribution with $L_X{\sim}5{\times}10^{42}\,\mathrm{erg\,s^{-1}}$, metallicity${\sim}0.25Z_\odot$, and M=2.7×$10^{13}M_\odot$; Mulchaey & Zabludoff claimed that these properties are comparable to those of groups.

They also estimated an R-band M/L=213, and interpreted it as a system deficient of stellar light. Hence, these authors suggested that NGC 1132 could be a *failed group* (with an atypical initial LF). Colbert (2001) studied its optical and IR

morphology, and did not find any sign of recent merger activity (e.g., dust, shells or tidal features).
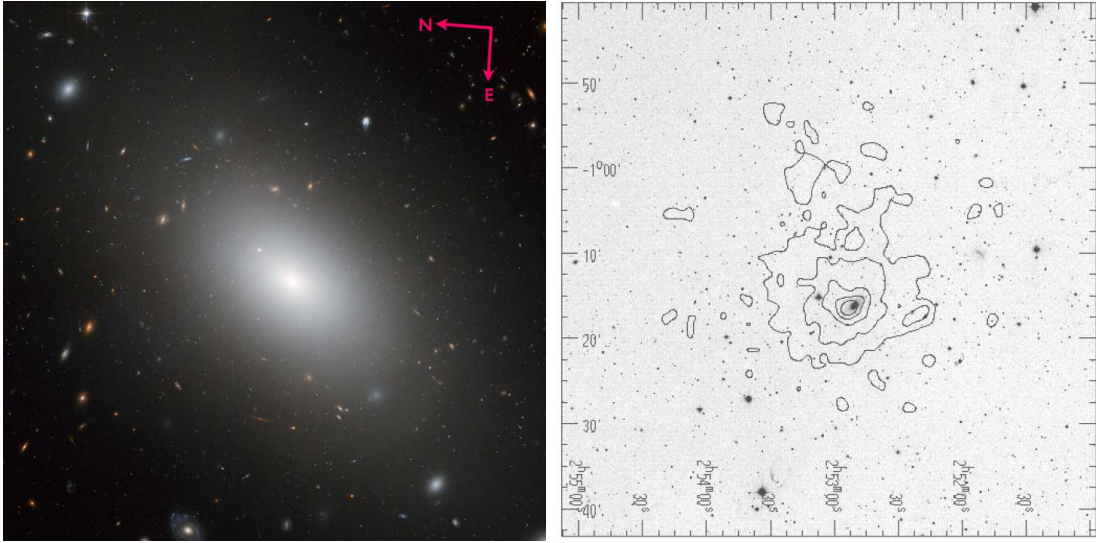
3.2.3   ESO 306-G017
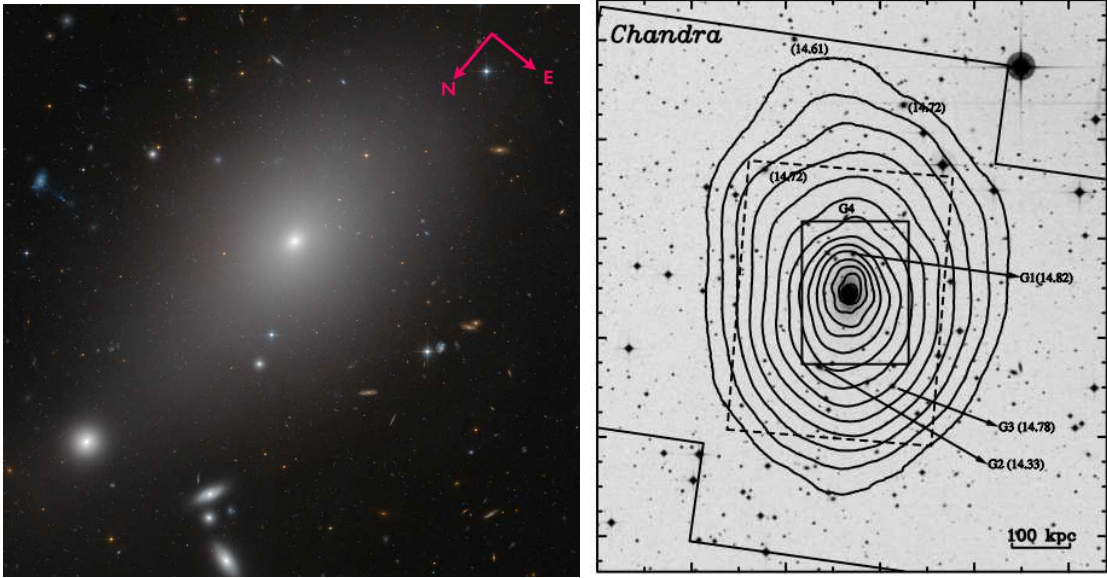
FIGURE 3.5: Fossil group ESO 306-G017. Left: optical ACS/HST RGB image, FOV∼ $3'.3 \times 3'.3$. Right: optical DSS image with Chandra X-ray contours of the disffuse emission, FOV∼$19' \times 22'$ (Sun et al. 2004).

ESO 306-G017 (RA:05h40m06.6s , DEC:-40°50′12″) is located at a distance of 155 Mpc (z=0.036); it was classified as a poor cluster (S 540) by Abell et al. (1989). Beuing et al. (1999) classified it as an X-ray overluminous early-type galaxy. This system was studied in detail by Sun et al. (2004). Using Chandra and XMM-Newton data, they found an extended and elongated X-ray emission with L_X=6.6×10^{43} erg s^{-1}. They also estimated a metallicity of ∼0.4$Z_\odot$, typical for galaxy groups; L_R=2.6×10$^{11}L_\odot$, comparable to the luminosity of cD galaxies; and an R-band M/L=150. With a mass of ∼2×10$^{14}M_\odot$, this system is the most massive FG discovered to date.

3.3 Observations and Data Reduction

The observations were taken with the ACS/*HST*, using the WFC with the *F475W* ($\approx$ the g passband of the SDSS) and *F850LP* ($\approx$SDSS z) filters (GO proposal 10558, P.I.: M. West).

The broadband g and z filters offer relatively high throughput and the $g-z$ color is very sensitive to age and metallicity variations (Côté et al. 2004). The integration time for each galaxy was chosen to reach the expected turnover magnitude of the GCLF, $M_g^0 = -7.2$ and $M_z^0 = -8.4$ (Jordán et al. 2007b), assuming a Gaussian distribution. Table 3.1 lists the distance, absolute magnitude in B-band, distance modulus, foreground extinction in B-band, expected apparent turnover magnitude of the GCLF for each filter, exposure time for each filter, as well as the physical scale corresponding to 1 arcsec. The ACS FOV is $\sim 3\farcs3 \times 3\farcs3$, with a pixel scale of 0.05 arcsec pixel^{-1}.

For all images the same data reduction procedure was followed. Geometrical correction, image combination, and cosmic ray rejection were done with the data reduction pipeline APSIS (Blakeslee et al. 2003). A PSF model was constructed for each image using the DAOPHOT (Stetson 1987) package within IRAF (Tody 1986). The best fitting function for all the images was Moffat25 (good for undersampled data), with FWHM$\sim$2 pixels and fitting radius=3 pixels.

System	d^b	M_B^a	m-M^b	A_B^a	$m^0{}_g$	$m^0{}_z$	$t_{exp,g}$	$t_{exp,z}$	1 arcsec
	(Mpc)						(s)	(s)	(pc)
NGC 6482	56.02	-21.82	33.74	0.43	26.54	25.34	928	1200	264
NGC 1132	99.47	-22.01	34.99	0.27	27.79	26.59	7800*	9630*	461
ESO 306-G017	155.46	-22.77	35.96	0.14	28.76	27.56	7057	8574	702

TABLE 3.1: Sample data
[a]Data from the NASA/IPAC Extragalactic Database (NED).
[b]$H_0 = 71$ km s^{-1}Mpc^{-1}.
*Due to a Hubble Observing Problem Report, the observation was repeated, obtaining at the end an image with longer exposure time than requested.

3.4 Analysis

We are interested in the detection and magnitudes of GCs, which can be affected by drastic changes in the background due to the galaxy light (mainly in the inner region). Hence, in order to perform the detections over an image with nearly flat background it is necessary to subtract the galaxy light.

3.4.1 Surface Brightness

To model the galaxy light, the brightest objects (foreground stars, background and group galaxies) were masked, and subsequently the surface brightness distribution of the central giant elliptical was modeled with the `ellipse` (Jedrzejewski 1987) and `bmodel` tasks within the STSDAS[1] package in IRAF. A second mask was made for objects detected at $> 4.5\sigma$ with SExtractor (Bertin & Arnouts 1996) in the galaxy-subtracted image. The final model of the surface brightness distribution of the stellar component (galaxy model) was produced from the newly masked image (Figure 3.6).

Due to the relatively small ACS field-of-view (FOV; $\sim 3\rlap{.}'3 \times 3\rlap{.}'3$), the giant ellipticals fill the images, and it is not possible to measure an absolute value for the sky brightness directly. Thus, a surface brightness radial profile of galaxy plus sky was constructed.

Although the exact value of the sky brightness is not a critical issue for calculating colors of GCs, since a local value is measured for each of them, a reliable estimate of the sky brightness is essential to measure the magnitude of the galaxy, which is needed to obtain S_{N}. In order to estimate a realistic sky value, we assumed that the starlight follows a Sérsic profile, which provides a good description of the outer parts of early-type galaxies (Section 2.1.1). We fit to the constructed intensity radial profile, including the sky component, equation 2.1.1:

---

[1]STSDAS is a product of the Space Telescope Science Institute, which is operated by AURA for NASA.
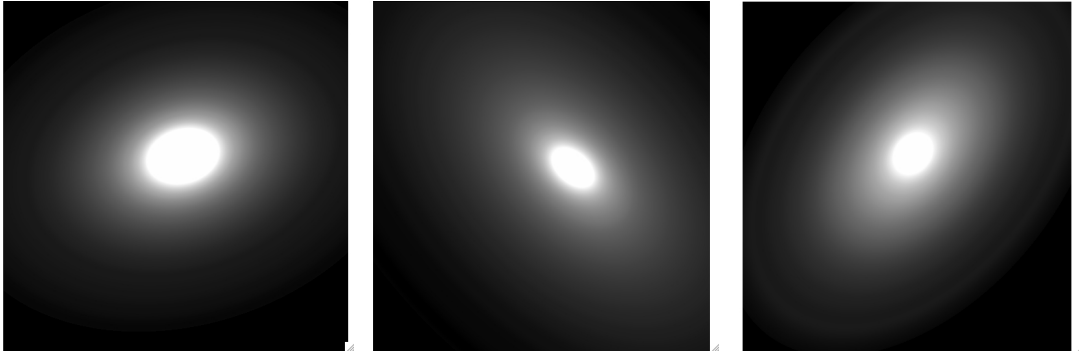
FIGURE 3.6: Galaxy bmodels in the z band for NGC 6482 (left), NGC 1132 (middle), and ESO 306-G017 (right).

$$I(r) = I_{\mathrm{e}} \exp \left\{ -b_{\mathrm{n}} \left[\left(\frac{r}{R_{\mathrm{e}}} \right)^{1/n} - 1 \right] \right\} + I_{\mathrm{sky}}, \tag{3.1}$$

where I_{sky} is the sky intensity; R_{e}, I_{e}, n, and b_{n} have been described in Section 2.1.1. The technique to estimate the best fit model was χ^2 minimization, using the task Optim inside R: A Language and Environment for Statistical Computing[2]. Optim uses the algorithm of Nelder-Mead (1965), which is based on the concept of a simplex, searching for the minimum by comparing the function values on vertices in parameter space. We tried various starting parameters in order to avoid local minima.

The fits were done independently for each filter. Each point was weighted by a factor ϵI, where I is the point's intensity and ϵ is chosen to obtain $\chi^2 \sim 1$ (Byun et al. 1996; Ferrarese et al. 2006); we used $\epsilon = 0.05$, 0.01 and 0.03 for NGC 6482, NGC 1132, and ESO 306-G017, respectively. We performed two fits, one with all the parameters free, and a second fixing $n = 4$. For NGC 1132 and ESO 306-G017, the sky values obtained for the $n = 4$ fits were higher than the mean background values in the regions of the images with the lowest surface brightness, which suggests that the sky levels obtained with these fits were overestimated. Moreover, with n as a free parameter, we recovered higher values ($n > 4$), in line with expectations for such luminous galaxies; thus, we favor the fits with n free (see Section 2.1.1).

---

[2]http://www.R-project.org.

We next subtracted the estimated sky value and converted the semi-major axis of each isophote to the equivalent circular (or geometric) radius, R^c, following the relation: $R^c = R\sqrt{q}$, where q here is the axis ratio of the isophote given by IRAF's task `ellipse`. We then performed a second fit to the sky-subtracted, circularized μ_{SB} profile (Fig. 3.7). This approach allows for direct comparisons with literature values (e.g., Ferrarese et al. 2006).

As seen from the fitted profiles, there is less light in the inner regions of NGC 1132 and ESO 306-G017 than predicted by the Sérsic profile (blue dashed lines). This is a common feature of giant ellipticals. Hence, we add a core component to the function in order to improve the models for these high-luminosity galaxies. The core-Sérsic function plus the sky contibution is:

$$I(r) = I_{\mathrm{b}} 2^{-(\gamma/\alpha)} \exp\left[b \left(2^{1/\alpha} \frac{R_{\mathrm{b}}}{R_{\mathrm{e}}} \right)^{1/n} \right]$$

(3.2)

$$\times \left[1 + \left(\frac{R_{\mathrm{b}}}{r} \right)^{\alpha} \right]^{\gamma/\alpha} \times \exp\left\{ -b \left[\frac{R^{\alpha} + R_{\mathrm{b}}^{\alpha}}{R_{\mathrm{e}}^{\alpha}} \right]^{1/(\alpha n)} \right\} + I_{\mathrm{sky}};$$

b_{n}, R_{b}, I_{b}, α, and γ have been described in Section 2.1.1.

For ESO 306-G017 we can see an excess of light around $\log_{10}(R^c) \sim 1.7$, that might be material stripped from the second brightest galaxy in the image. Consequently, we reject the range $12.5'' < R^c < 90''$ from the fit domain in both filters (gray dots in Fig. 3.7), whereupon we obtain a good fit. Nonetheless, Sun et al. (2004) reported a steeper profile over a larger spatial range using ground-based data in the R-band, with the profile declining more sharply than $n = 4$ at large radii. It would be unusual for a galaxy with such high luminosity to have $n < 4$. The inconsistency in n values at different radii in this galaxy reflects the peculiarity of its light profile, indicating that a single Sérsic model does not provide an adequate description. For the more regular galaxy NGC 1132, Schombert & Smith (2012) give $n = 7.1$ and a circular effective radius $R_{\mathrm{e}}^c = 80.6''$, both of which are close to our fitted values. Table 3.2 lists our final best-fit Sérsic parameters and sky
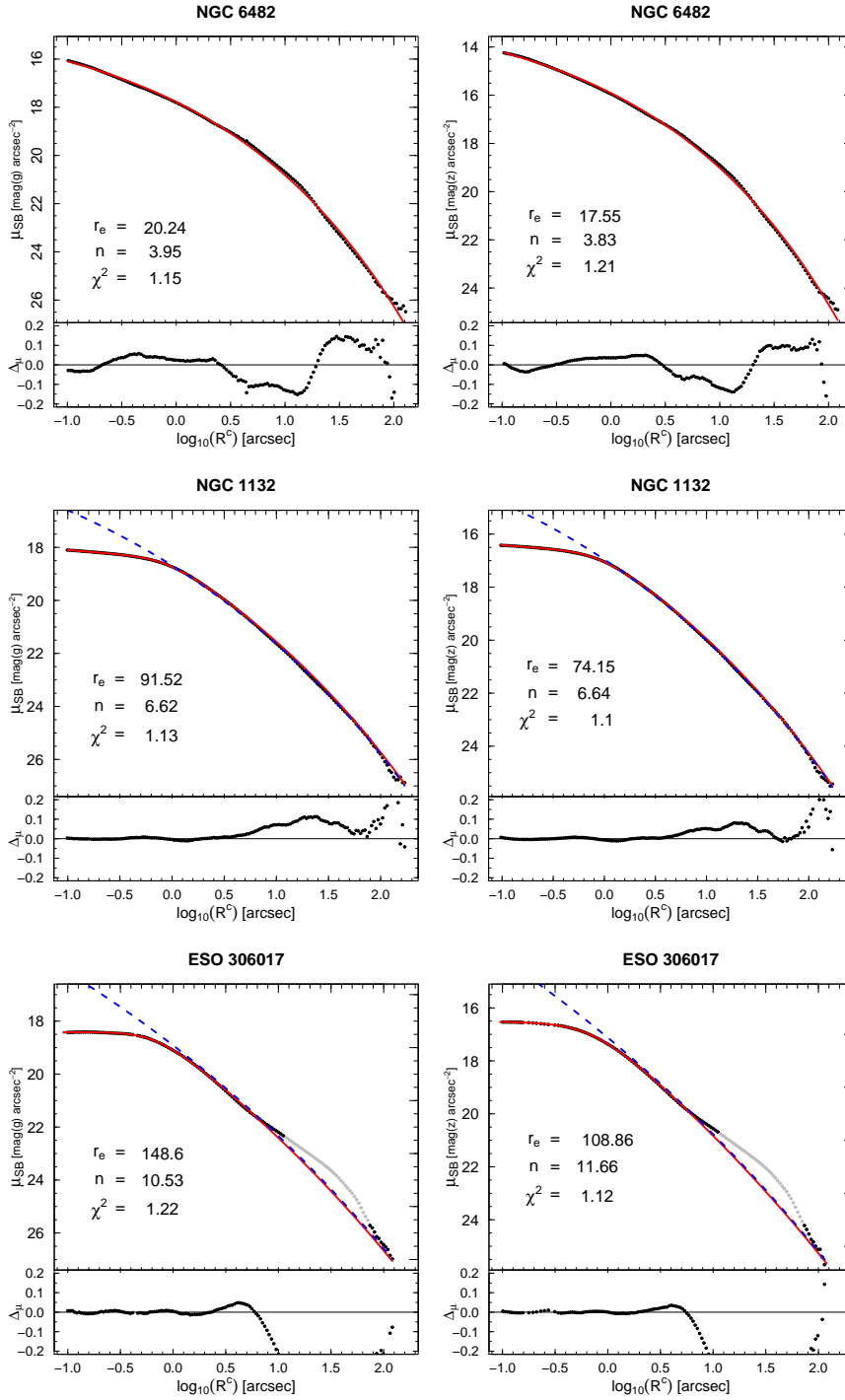
FIGURE 3.7: Galaxy surface brightness distribution as a function of the isophotal equivalent circular radius R^c. *Left panels:* g-band. *Right panels:* z-band. Dots: data after subtraction of the fitted sky value. Solid red lines: best fit profiles: single Sérsic for NGC 6482, and core-Sérsic for NGC 1132 and ESO 306-G017(gray dots were not included in the fits of this galaxy). Dashed blue lines: single Sérsic for NGC 1132 and ESO 306-G017. Fit residuals are shown in the bottom of each panel.

g band							
Galaxy	$R_{\mathrm{e,g}}{}^c$ [arcsec]	n^{g}	$R_{\mathrm{b}}{}^{\mathrm{g}}$ [arcsec]	γ^{g}	α^{g}	χ^2_{g}	$m_{\mathrm{g}}^{\mathrm{sky}}$ [mag/arcsec^2]
NGC 6482	20.2	3.9				1.15	23.38
NGC 1132	91.5	6.6	0.8	0.13	3.12	1.13	22.92
ESO 306-G017	148.6	10.5	0.64	0	2.97	1.22	23.22
z band							
	$R_{\mathrm{e,z}}{}^c$ [arcsec]	n^{z}	$R_{\mathrm{b}}{}^{\mathrm{z}}$ [arcsec]	γ^{z}	α^{z}	χ^2_{z}	$m_{\mathrm{z}}^{\mathrm{sky}}$ [mag/arcsec^2]
NGC 6482	17.6	3.8				1.21	22.65
NGC 1132	74.1	6.6	0.81	0.11	2.92	1.1	22.02
ESO 306-G017	108.9	11.7	0.64	0.02	2.36	1.12	22.16

TABLE 3.2: Best galaxy surface brightness model parameters in *g* and *z* bands: single Sérsic for NGC 6484, and core-Sérsic for NGC 1132 and ESO 306-G017.

values. The values for R_{b} are small but more than 10 times larger than the angular resolution ($0.05''$).

Elliptical galaxies are well described by Sérsic or core-Sérsic profiles unless they are disturbed due to recent interaction (Ferrarese et al. 2006). In order to detect any signature of disturbances, we constructed Sérsic models in two dimensions. We used the Sérsic parameters obtained from the previous fitting and the program BUDDA (de Souza et al. 2004). Because the fit we obtained is in one dimension, in order to construct the 2-D model we needed to assign ellipticities and position angles (PA), which we took from the `ellipse` fit. These values are nearly constant, except in the very inner region (see Fig. 3.14), probably due to dust or inner structures. Thus, we chose the mean values of ellipticity and PA of the outer region isophotes ($r > 30$ arcsec). These models were subtracted from the original images to obtain the images in the left column of Figure 3.8.

For NGC 1132 we see residuals with an appearance of shells; in order to rule out that these are caused by a bad choice of PA value, we constructed model images changing the PA. We recovered the shell-like structure in all cases. The existence of dust lanes is evident in the inner regions of all three FGs (right panels of Figure 3.8). Furthermore, the residual images (left panels of Figure 3.8) show evidence of galactic interaction: apparent shells in NGC 1132, a tidal tail in ESO 306-G017, and an inner disk in NGC 6482. It must be noted that these features contradict
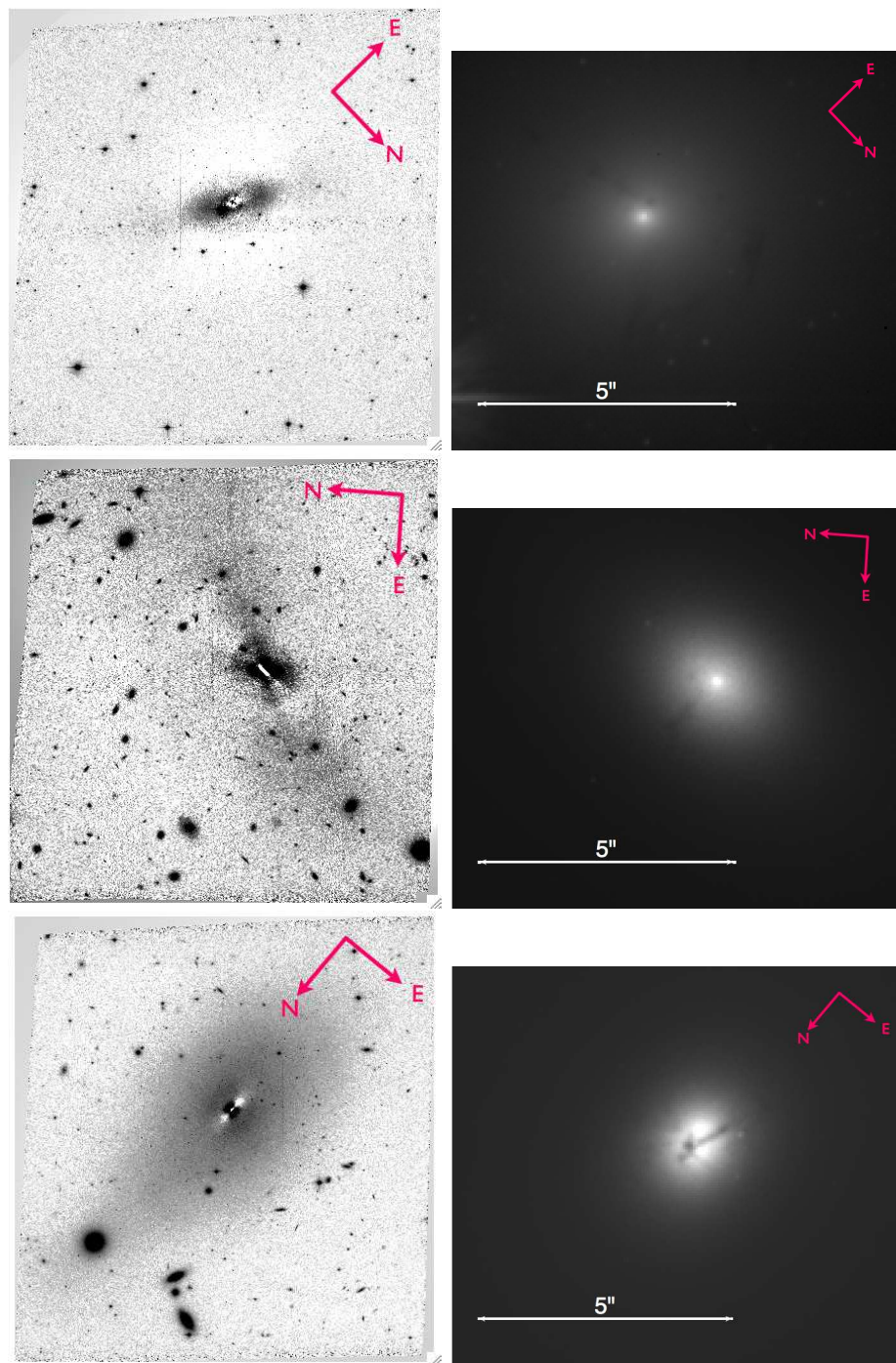
FIGURE 3.8: Left: residual z-band images after subtracting the best single Sérsic model. Right: Inner regions of g-band images; dust is present in all cases. Top to bottom: NGC 6482, NGC 1132, and ESO 306-G017.

the claims of previous authors, who did not find signs of merger activity (Jones et al. 2003; Khosroshahi et al. 2004).

3.4.2   GC Detection

Based on their recession velocities, NGC 6482, NGC 1132, and ESO 306-G017 are located at 56, 99, and 155 Mpc, respectively (Table 3.1); GCs which have $r_{\rm h}$ of $\sim$ 3 pc (Section 1.1.1) will be unresolved and appear as an excess of point sources over the foreground stars and small background galaxies. The number of these contaminants can be estimated using control fields.

The detection and photometry of GC candidates were done with SExtractor, using RMS maps that indicate the weight of each pixel according to read noise, cosmic rays, and saturated pixels. The confidence in the detections is naturally greater for brighter objects, but reaching fainter magnitudes allows a better sampling of the GCLF. Aiming at a compromise between GCLF completeness and good rejection of spurious detections, we chose a threshold of 1.5 σ per pixel, and a minimum area for a positive detection MINAREA = 5 pixels; together, these constraints imply a minimum effective detection threshold of 3.35 σ. An initial sample was constructed with objects detected independently in both the g and z filters, with matching coordinates within a radius of 2 pixels, ellipticity lower than 0.3, and CLASS_STAR[3] greater than 0.7.

We adopt the photometric AB system, for which the zero points are $zp_{\rm g} = 26.081$ and $zp_{\rm z} = 24.867$.[4] These values are valid for an infinite aperture; we use aperture photometry (with a 3 pixel radius), and apply an appropriate aperture correction (Sirianni et al. 2005). Magnitudes are corrected for foreground extinction using the reddening maps of Schlegel et al. (1998) for each field and filter. The extinction transformations to g and z are $A_{\rm g} = 3.634\,E(B-V)$ and $A_{\rm z} = 1.485\,E(B-V)$. $E(B-V)$ values for NGC 6482, NGC 1132, and ESO 306-G017 are 0.099, 0.065, 0.033[5], respectively.

Objects five magnitudes brighter than the expected turnover magnitude, m^0, in both filters ($m_{\rm g,z} < m^0_{\rm g,z} - 5$, see Table 3.1), were rejected from the GC sample,

---

[3]SExtractor parameter that classifies the objects according to their fuzziness; point sources have CLASS_STAR ~ 1, while for extended objects it is ~ 0.

[4]http://www.stsci.edu/hst/acs/analysis/zeropoints.

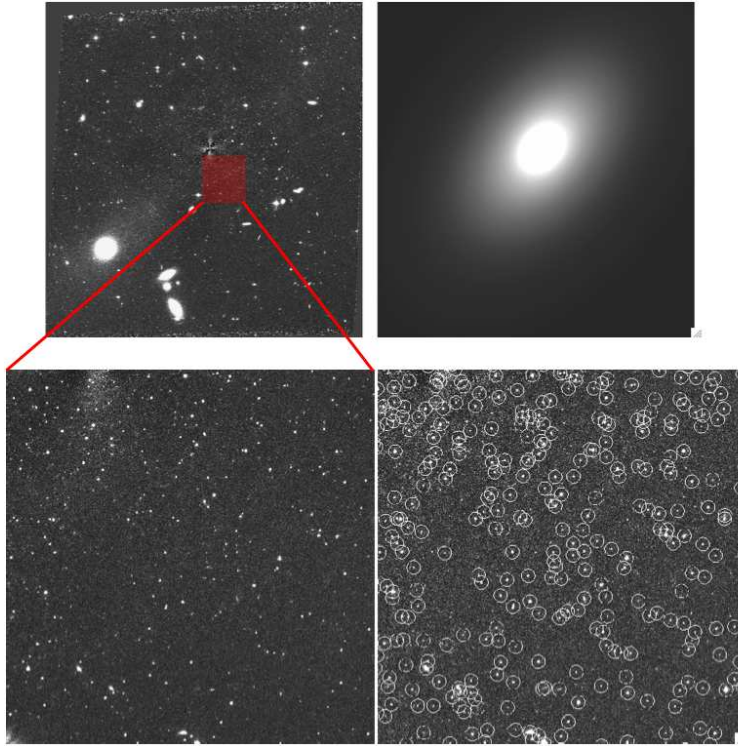[5]http://irsa.ipac.caltech.edu/applications/DUST.

FIGURE 3.9: ESO 306-G017 in z-band. Upper left: residual image; upper right: bmodel of the galaxy; bottom left: zoomed region to the center of the residual image; bottom right: same as bottom left, including the apertures of the objects detected with SExtractor.

as they are undoubtedly contaminants. With this cut we reject $\lesssim 0.02\%$ of the brightest GCs, but we avoid foreground stars.

Objects with reddening-corrected color $0.5 < g-z < 2.0$ were kept; single stellar populations with ages 2-15 Gyr and metallicities $-2.25 < [\text{Fe/H}] < +0.56$ lie in this range (Côté et al. 2004). Finally, the selected sample of GC candidates was cleaned of objects with an uncertainty in magnitude larger than 0.2 mag.

To determine the GC detection completeness as a function of magnitude, $\sim 25,000$ artificial stars were constructed based on the PSF of each image, with magnitudes in the interval $22 < m_{\text{star}} < 29$, and color $0.7 < g_{\text{star}} - z_{\text{star}} < 1.7$, where most GCs lie. This color range is slightly narrower than the color criterion for GCs because we needed to take into account the dispersion in the magnitude measurements (Fig. 3.10). Only ~ 100 stars were added randomly at a time, in order to avoid crowding and overlapping with original objects. Afterwards, each image was
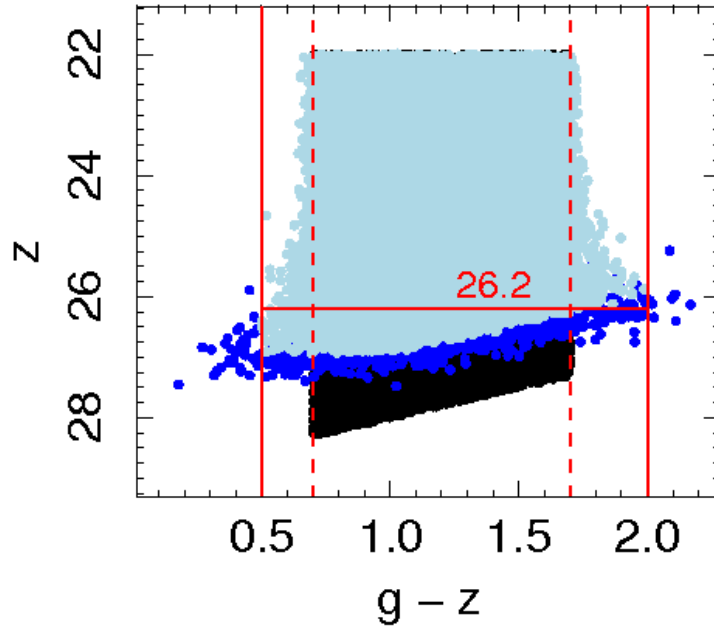
FIGURE 3.10: Color magnitude diagram of added stars. The black points are the constructed stars (input values), overplotted are all the recovered objects (dark blue points) and the recovered objects after applying the same constraints as for GC selection for ESO 306-G017 (light blue points).

analysed in exactly the same way as the original data. The fraction of recovered stars as a function of magnitude is well described by a function of the form:

$$f^P(m) = \frac{1}{2} \left[1 - \frac{\alpha(m - m_{\text{lim}})}{\sqrt{1 + \alpha^2(m - m_{\text{lim}})^2}} \right] , \qquad (3.3)$$

where m_{lim} is the magnitude at which the completeness is 0.5, and α determines the steepness of the curve. This function f^P is sometimes referred to as a "Pritchet function" (e.g., McLaughlin et al. 1994; Fleming et al. 1995). The Pritchet curve fitted to the fraction of recovered stars versus magnitude provides our *completeness function* (Fig. 3.11). Based on the completeness test we are confident that the detection is $\gtrsim 90\%$ complete at $z = 24.7$, 26.2, and 26.2 for NGC 6482, NGC 1132, and ESO 306-G017, respectively. These values are not as deep as the expected

turnover magnitudes (see Table 3.1), but we prefer to be reliable rather than trying to push the magnitude limit.
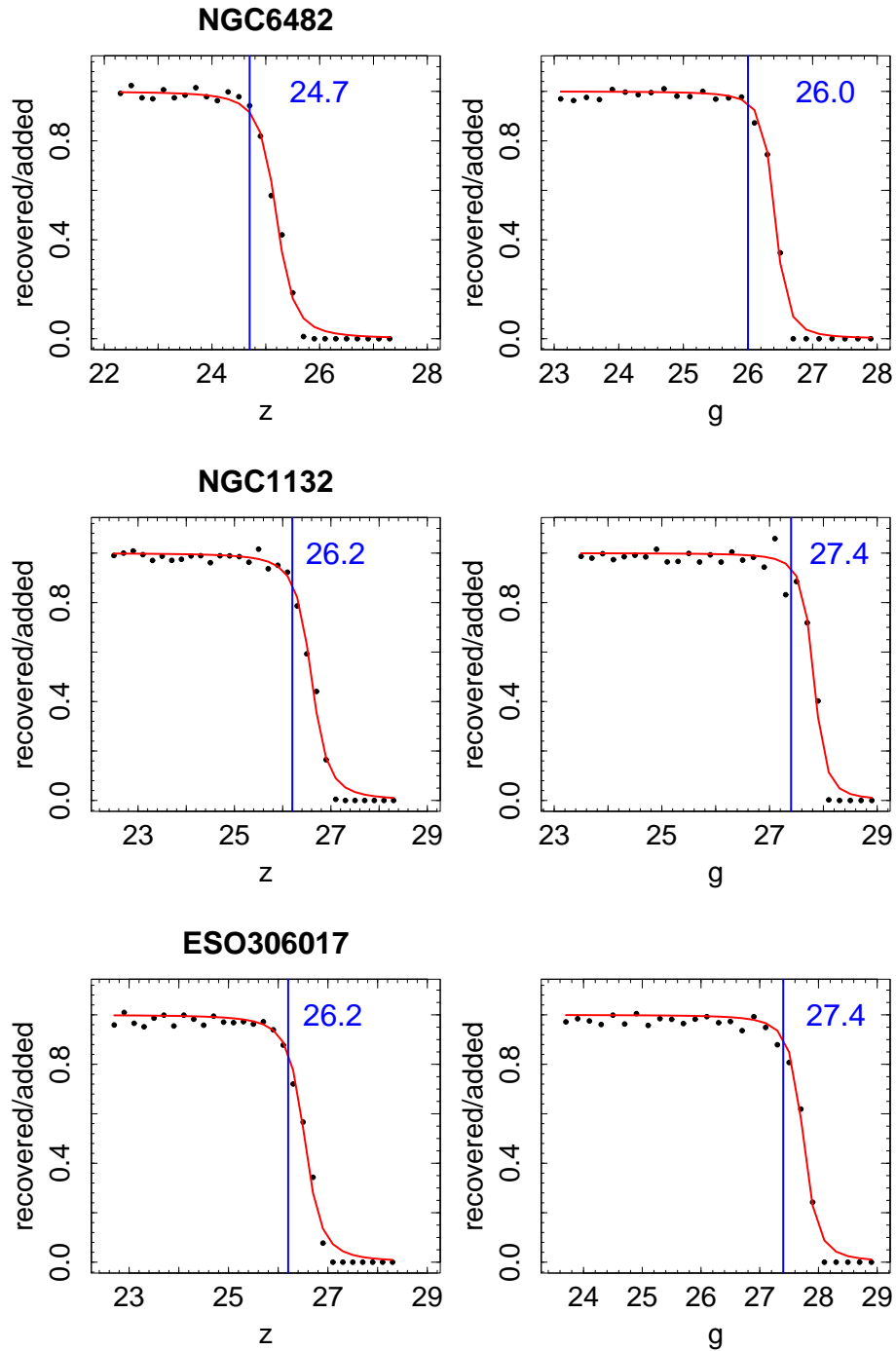

FIGURE 3.11: Completeness tests. Dots: fraction of recovered artificial stars as a function of magnitude. Solid red line: fitted Pritchet function. Blue line and number: magnitude where data are nearly 100% complete.

The upper limit in luminosity might still include some ultra-compact dwarfs (UCDs), but we assume that those are just the brightest GCs in the distribution (see Madrid 2011, 2013). The number of GCs detected by direct photometry, without any spatial, luminosity or contamination correction, are 369, 1410, and 1918 for NGC 6482, NGC 1132, and ESO 306-G017, respectively. In Fig. 3.12 we show the color magnitude diagram of all objects detected in both filters (*black points*), highlighting the GC selected sample (*blue points*); there is a clear excess of point sources within the color range expected for GCs in all these fields.
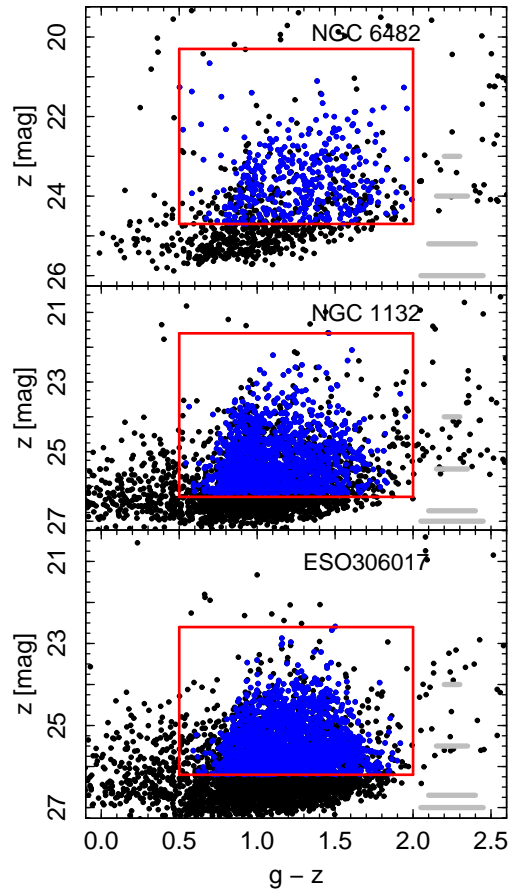
FIGURE 3.12: Color magnitude diagram of objects in the FG fields. Black dots: all detected objects in the FOV. Thick gray lines: error bars in color at different magnitudes. Blue dots framed within the red lines: selected sample of GC candidates with color range $0.5 < g-z < 2.0$. The bright magnitude limit is at $m_z = m_z^0 - 5$; beyond the faint magnitude limit, there is a dependence of the detection limit on color, and redder objects are missed.

As mentioned before, some contamination is expected due to foreground stars and unresolved background galaxies. To estimate the number of these contaminants, N_{cont}, the above detection procedure and selection criteria were applied to three "blank" background fields obtained from the *HST* archive that were chosen to have Galactic latitudes and exposure times in g and z similar to our two deeper fields (NGC 1132 and ESO 306-G017), but without any large galaxies present in the FOV.

In order to simulate the same detection conditions for the empty fields, we applied the rms maps of the FG fields to the blank fields. The number of contaminants is taken to be the average of the three fields. We find $N_{\text{cont}} = 7$, 6, and 7 for NGC 6482, NGC 1132, and ESO 306-G017, respectively; these values correspond to $\sim 1\%$ or less of the number of detected GC candidates, which is negligible. We note that NGC 6482 has Galactic latitude $b \approx 23°$, about $10°$ smaller than that of the lowest latitude control field. Thus, its contamination may be somewhat higher, but not more than by a few per cent, as supported by the steep spatial distribution found below for the GC candidates in this galaxy.

3.5 Results

3.5.1 Globular Cluster Color Distribution

In order to detect and quantify the existence of color bimodality, the data were binned in $(g - z)$ using an optimum bin size, B_{opt} (Izenman 1991; Peng et al. 2006), that depends on the sample size, n, and inter-quartile range, IQR, which is a measure of the dispersion of the distribution:

$$B_{\text{opt}} = 2(IQR)n^{-1/3}. \tag{3.4}$$

Afterwards, we used the algorithm Gaussian Mixture Modeling (GMM), which identifies Gaussian distributions with different parameters inside a dataset through the expectation maximization (EM) algorithm (Muratov & Gnedin 2010). GMM also performs independent tests of bimodality (measure of means separation and

System	μ_{blue}	N_{blue}	σ_{blue}	μ_{red}	N_{red}	σ_{red}	$\overline{g-z}$	p-value	D	k
NGC 6482	1.02 ± 0.02	181 ± 16	0.19 ± 0.02	1.49 ± 0.02	188 ± 16	0.19 ± 0.02	1.26	0.001	2.42 (0.001)	-0.7
NGC 1132	0.91 ± 0.01	540 ± 87	0.10 ± 0.01	1.23 ± 0.03	870 ± 87	0.23 ± 0.02	1.11	0.01	1.88 (0.13)	-0.41
ESO 306-G017	0.99 ± 0.02	781 ± 124	0.12 ± 0.01	1.34 ± 0.03	1137 ± 124	0.19 ± 0.01	1.20	0.01	2.17 (0.08)	-0.59

TABLE 3.3: Parameters of the best GMM fit. *Col. 1*: system name; *Cols. 2*, 3 and 4: mean value, size and dispersion of blue population; *Cols. 5*, 6 and 7: mean value, size and dispersion of red population; *Col. 8*: mean color of the GC population; *Col. 9*: probability of recovering the same χ^2 value from a unimodal distribution; *Col. 10*: separation of the means, D=$| \mu_{\mathrm{blue}} - \mu_{\mathrm{red}} | /[(\sigma_{\mathrm{blue}}^2 + \sigma_{\mathrm{red}}^2)/2]^{1/2}$; in parenthesis, the probability of recovering the same value from a unimodal distribution; *Col. 11*: kurtosis of the color distribution.

kurtosis), calculates the error of each parameter with bootstrapping, and estimates the confidence level at which a unimodal distribution can be rejected.

Figure 3.13 shows the $(g - z)$ color distributions, together with the best fit Gaussians obtained with GMM. For NGC 6482 the best model is homoscedastic (same variance), while for NGC 1132 and ESO 306-G017, a heteroscedastic (different variance) model provides a significantly better fit. The means, μ_{color}, and dispersions, σ_{color}, of the best fitting Gaussians are listed in Table 3.3; they are consistent with parameters in the literature for early-type galaxies (Peng et al. 2006). In Table 3.3, Cols. 9 and 10, we list the probability of obtaining the recovered values from a unimodal Gaussian distribution. Since these probabilities are small, relative to a null hypothesis of Gaussian unimodality, we are confident that the color distributions are bimodal.

3.5.2 Globular Cluster Spatial Distribution

Harris (1991) noted that in general the spatial distribution of GC systems is more extended than the starlight in their parent galaxies. Furthermore, it is known that the blue GCs have a more extended spatial distribution than the red GCs (Geisler et al. 1996; Rhode & Zepf 2004). To see how the distributions compare in these FGs, we first need to select the blue and red GC subsamples.
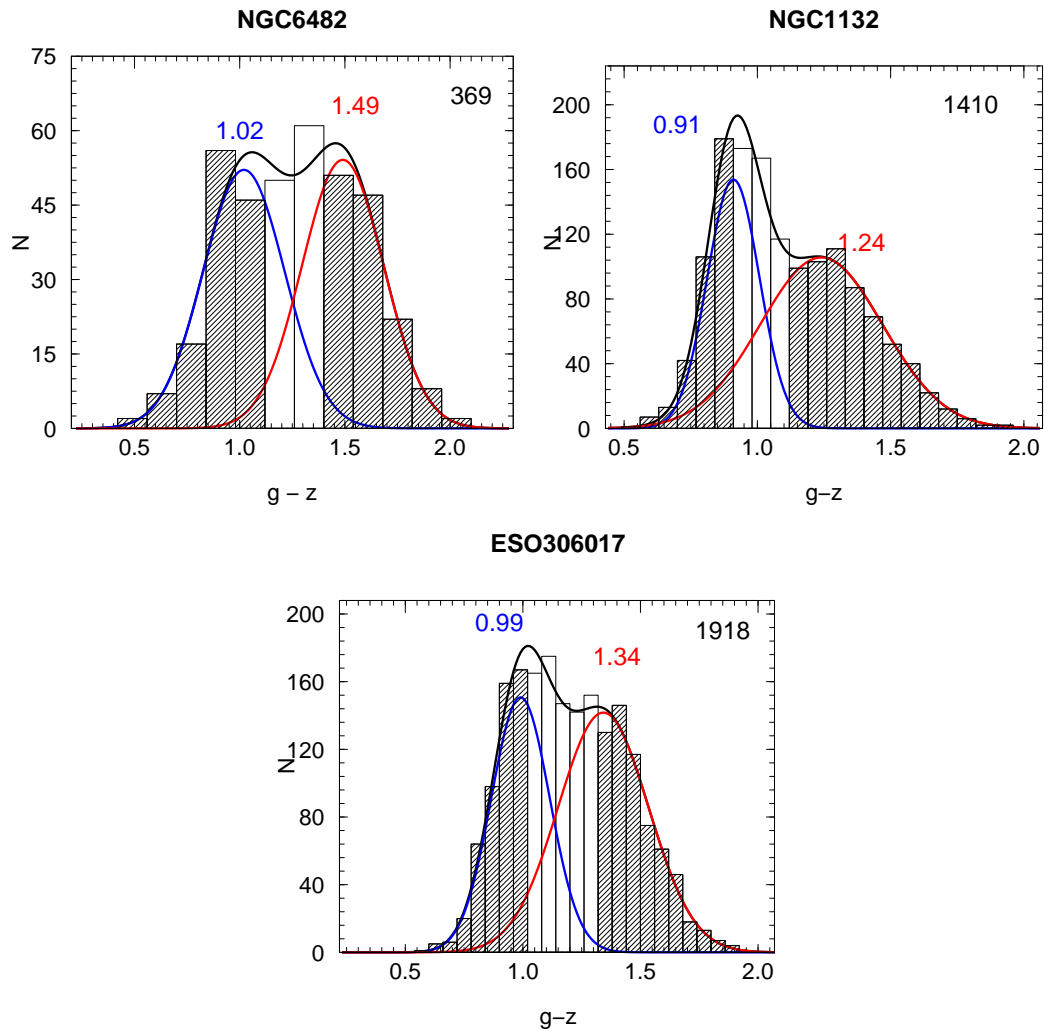
FIGURE 3.13: Color histograms with the best GMM two-Gaussian fit. Red and blue solid lines: individual Gaussians; red and blue numbers: their means; black solid line: sum of Gaussians; hatched areas: objects we include in the blue and red populations. The total number of detected GCs is shown in the upper right of each panel.

In Fig. 3.13, we see that the two Gaussian subpopulations overlap. In order to avoid cross-contamination between the two populations, we reject objects in the overlap regions, selecting blue and red population as indicated by the hatched regions. Because the mixed fractions are different for the three FGs color distributions, the cuts are different for each one: $\mu_{blue} + 0.1$ for NGC 6482, and μ_{blue} for NGC 1132 and ESO 306-G017; $\mu_{red} - 0.1$ for NGC 6482 and NGC 1132, and μ_{red} for ESO 306-G017 (see Fig. 3.13). Figure 3.14 shows the spatial distributions of blue and red GCs thus defined.
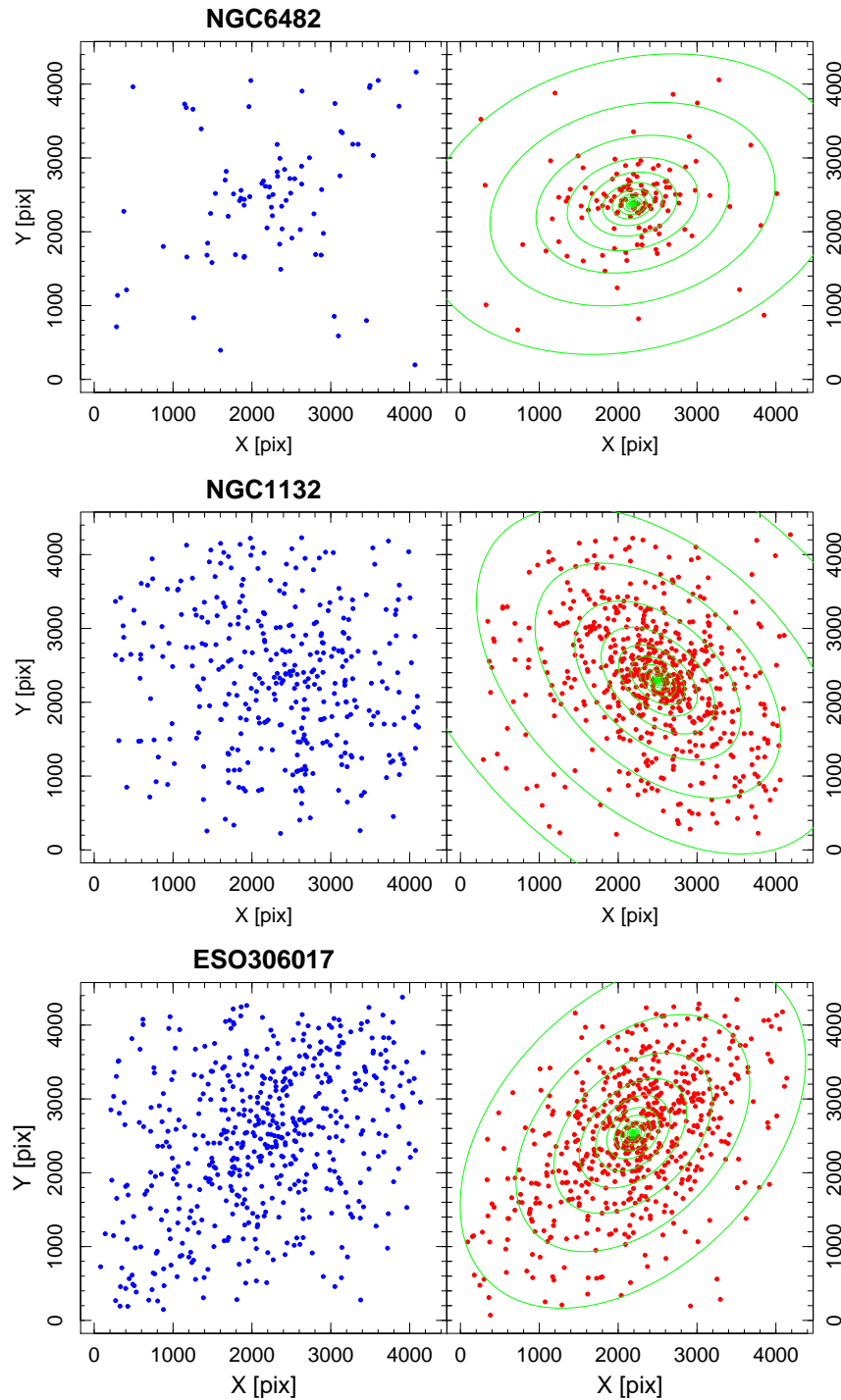
FIGURE 3.14: Spatial distribution of blue (left panel) and red (right panel) populations selected from the color histograms (hatched regions in Fig 3.13). Along with the red population, green ellipses show the starlight distribution.
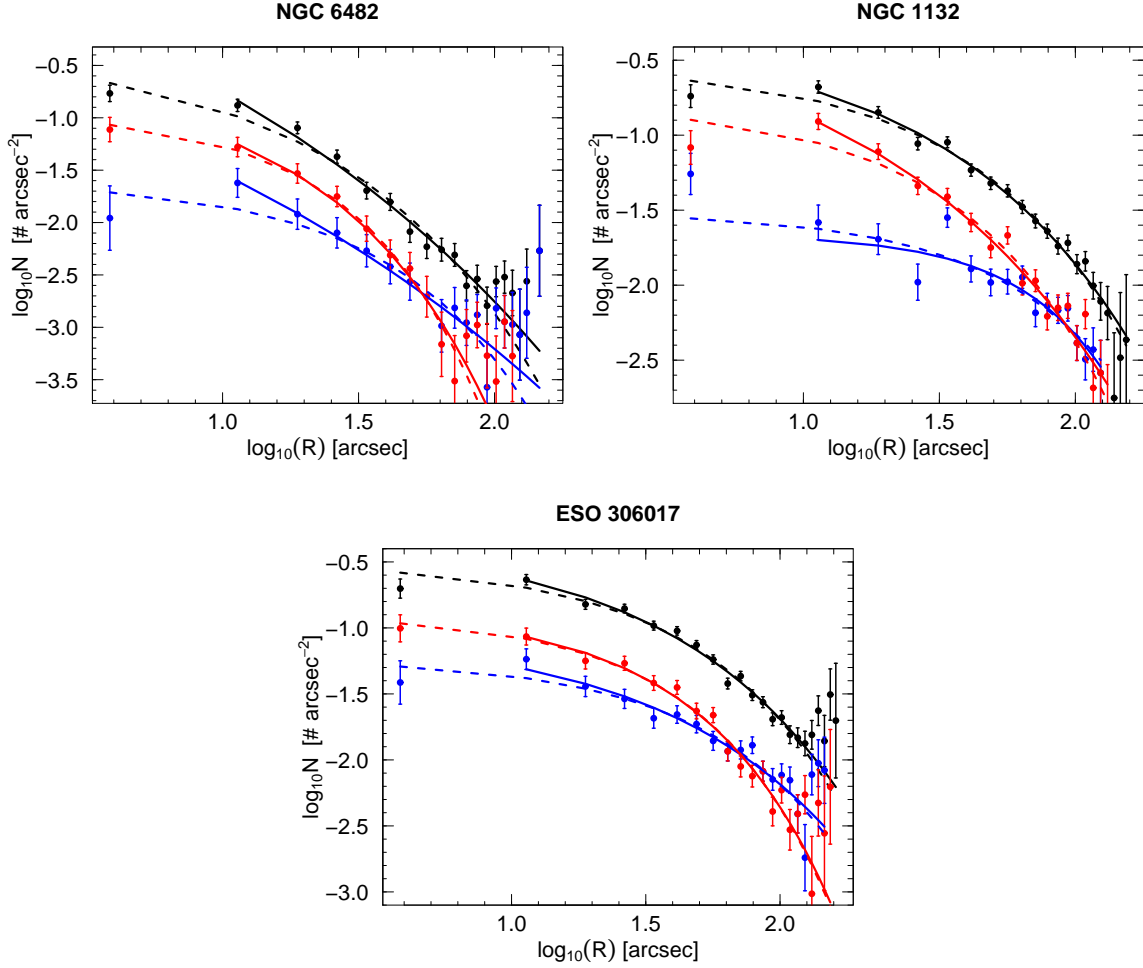
FIGURE 3.15: Surface number density of GCs. Dots: data; lines: best Sérsic fits including all the points (dashed lines) and excluding the innermost point (solid lines) for all the detected GCs (black), only blue GCs (blue), and only red GCs (red).

We measured the surface number density $\mathcal{N}$ of the blue and red populations by counting the number of GCs inside circular annuli with a width of $7\overset{''}{.}5 = 150$ pixels. To compare the GC spatial distribution with the starlight profiles, we fitted Sérsic functions to the radial $\mathcal{N}$ profiles. The fitted function is:

$$\mathcal{N}(r) = \mathcal{N}_{\mathrm{e}} \exp \left\{ -b_n \left[\left(\frac{r}{R_{\mathrm{e}}{}^{\mathrm{GC}}} \right)^{1/n_{\mathrm{GC}}} - 1 \right] \right\}, \qquad (3.5)$$

where $R_{\mathrm{e}}{}^{\mathrm{GC}}$ is the effective radius, that contains half of the GC population; $\mathcal{N}_{\mathrm{e}}$ is the surface number density at $R_{\mathrm{e}}{}^{\mathrm{GC}}$; n_{GC} is the Sérsic index. We performed

GC surface density Sérsic parameters

System	R_e^{all} (*arcsec*)	n^{all}	χ^2_{all}	R_e^{blue} (arcsec)	n^{blue}	χ^2_{blue}	R_e^{red} (arcsec)	n^{red}	χ^2_{red}
Including all the points in the fit									
NGC 6482	32.03	1.60	1.75	45.73	1.17	1.04	22.66	1.01	0.95
NGC 1132	65.68	1.27	1.36	99.06	1.09	1.85	50.70	1.21	2.10
ESO 306-G017	70.29	1.19	1.96	88.65	1.16	1.37	50.57	1.04	1.24
Excluding the innermost point from the fit									
NGC 6482	27.91	3.66	1.04	60.64	4.40	0.75	21.00	1.29	0.97
NGC 1132	70.36	1.59	1.11	82.73	0.77	1.74	54.11	2.01	1.33
ESO 306-G017	77.06	1.49	1.65	106.38	1.56	1.36	50.77	1.09	1.31

TABLE 3.4: Parameters of the best Sérsic fit for all GCs, only red, and only blue populations.

a second fit excluding the innermost point, since the GCs closest to the galaxy center are more strongly affected by dynamical friction. In Fig. 3.15, we show the density profiles of all, only blue, and only red GCs, together with the best Sérsic fits. Table 3.4 shows the fitted parameters. As expected, the difference between both fits is larger for the closest system, NGC 6482, because we are looking at smaller physical scales than for NGC 1132 and ESO 306-G017.

To compare the Sérsic profiles of the galaxy light (Fig. 3.15) with those of the GC number density (Fig. 3.7), in Fig. 3.16 we plot them together, using an arbitrary relative scale. From this diagram we can see that the GC distribution in each galaxy is more extended than its starlight. Nevertheless, we must remember that the comparison of R_e is accurate only if the profiles have similar n.

We find that R_e^{blue} is larger than R_e^{red}, and Figs. 3.14 and 3.15 show that the blue populations are more extensively distributed than the red ones for these three FGs. Also, the distributions of the red populations are more elongated and seem to trace the shape of the galaxy more closely than the blue population.

3.5.3 Globular Cluster Luminosity Function

To parameterize the GCLF, the GC magnitudes, m, were binned, again using an optimum bin size (Eq. 3.4). Figure 3.17 shows the GCLFs for NGC 6482,
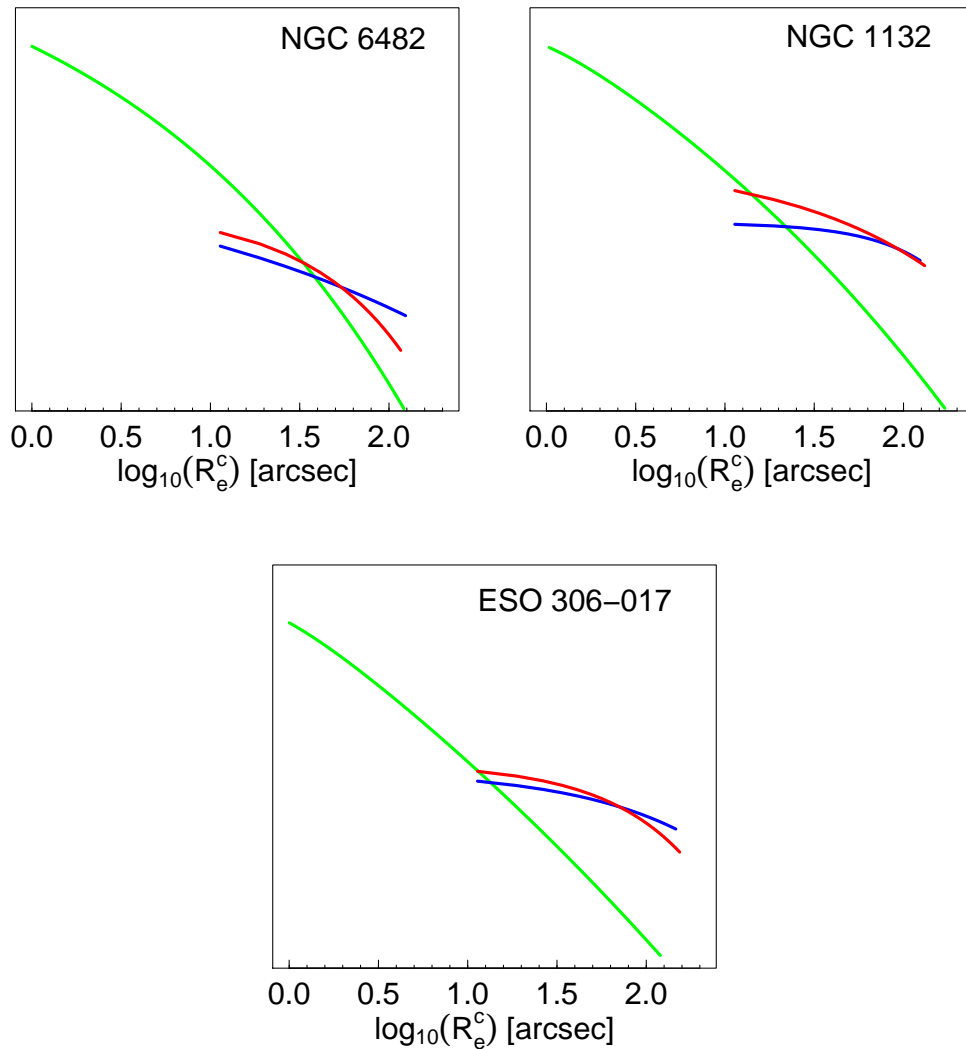
FIGURE 3.16: Comparison of Sérsic profiles. Green solid line: galaxy surface brightness in the z band; blue line: blue GC population only, without innermost point; red line: red GC population only, also excluding innermost point. The relative scale of the galaxy and GC profiles is arbitrary.

NGC 1132, and ESO 306-G017, respectively. Because we are photometrically limited, we do not detect all the GCs in the FOV. The GCLFs that we recover are the convolution of the intrinsic GCLFs and the incompleteness functions. To get the total number of GCs in the FOV, $N_{\rm GC}^{\rm total}$, we fit the product of a Gaussian and a Pritchet function to the GC magnitudes. The function we fit is:

GCLF fitted parameters.

System	m^0 ($N_{\rm GC}{}^{\rm total} \pm \Delta N$)	$\chi^2{}_{m^0}$	$\sigma_{\rm GCLF}$ ($N_{\rm GC}{}^{\rm total} \pm \Delta N$)	$\chi^2{}_{\sigma_{\rm GCLF}}$
	g band			
NGC6482	25.94 (787 $\pm$ 40)	1.04	1.62 (1101 $\pm$ 49)	1.23
NGC1132	27.52 (3298 $\pm$ 173)	1.03	1.42 (3990 $\pm$ 174)	1.36
ESO 306-G017	28.52 (9643 $\pm$ 807)	1.19	1.44 (11778 $\pm$ 597)	1.27
	z band			
NGC6482	24.84 (863 $\pm$ 36)	1.01	1.61 (1130 $\pm$ 42)	1.13
NGC1132	26.86 (4911 $\pm$ 252)	0.93	1.3 (4161 $\pm$ 133)	1.29
ESO 306-G017	27.66 (15460 $\pm$ 1224)	1.18	1.33 (14941 $\pm$ 692)	1.11

TABLE 3.5: *Col. 1*: system; *Col. 2*: m^0 and total number of GC fixing $\sigma_{\rm GCLF} = 1.4$; *Col. 3*: reduced chi-squared when fitting m^0; *Col. 4*:$\sigma_{\rm GCLF}$ and total number of GC fixing m^0; *Col. 5*: reduced chi-squared when fitting $\sigma_{\rm GCLF}$.

$$f(m) = \frac{a_0}{\sqrt{2\pi\sigma_{\rm GCLF}^2}} e^{\frac{-(m-m^0)}{2\sigma_{\rm GCLF}^2}} * \frac{1}{2}[1 - \frac{\alpha(m - m_{\rm lim})}{\sqrt{1 + \alpha^2(m - m_{\rm lim})^2}}]. \qquad (3.6)$$

The values of the parameters α and $m_{\rm lim}$ are obtained from the incompleteness test. We perform two fits. Firstly, we treat the mean value, m^0, and amplitude, a^0, of the Gaussian as free parameters, and fix the dispersion of the Gaussian to $\sigma_{\rm GCLF} = 1.4$ (expected value for giant ellipticals, see Section 1.2.3). Secondly, we fit for $\sigma_{\rm GCLF}$ and a^0, and set m^0. The fits were done by χ^2 minimization using the Optim task. The same procedure was performed independently in the g and z bands; we obtain better results in the z band and when fixing the $\sigma_{\rm GCLF}$. Table 3.5 shows the best values for $\sigma_{\rm GCLF}$ and m^0 recovered from the fits, as well as the estimated $N_{\rm GC}^{\rm total}$ in each case. From Fig. 3.17 we can see that the recovered values are consistent with the expected ones for NGC 1132 and ESO 306-G017; however, for NGC 6482 the recovered m^0 and $\sigma_{\rm GCLF}$ are shifted by $\sim$0.5 and 0.2 mag, respectively.

3.5.4 Specific Frequency

As mentioned in Section 1.2.1, the specific frequency of GCs is $S_{\rm N} = N_{\rm GC} 10^{0.4(M_{\rm V}+15)}$. To derive the absolute V-band magnitudes of the galaxies, we first calculate the g and z magnitudes from the counts in our 2-D isophotal model images, subtracting
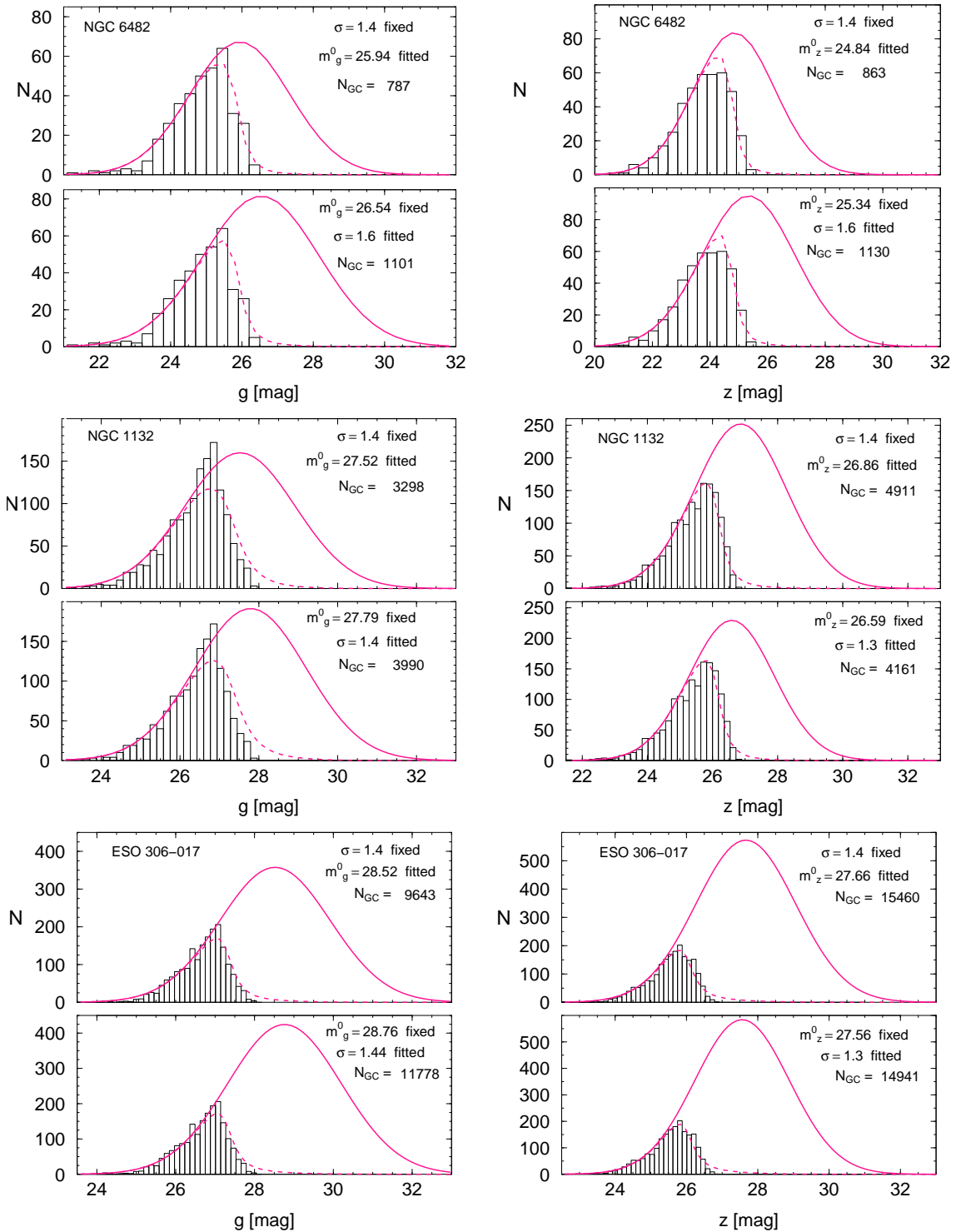
FIGURE 3.17: GC luminosity functions in the *g* (left panel) and *z* (right panel) bands. Dashed lines: best-fit Gaussian × Pritchet (completeness function) model; solid lines: respective Gaussian only. The numbers indicate the fixed and fitted parameters.

Specific frequency

System	$N_{\mathrm{GC},0}^{\mathrm{total}}$	$M_{\mathrm{g}}^{\mathrm{FOV}}$	$M_{\mathrm{z}}^{\mathrm{FOV}}$	$M_{\mathrm{V}}^{\mathrm{FOV}}$	$S_{\mathrm{N}}^{\mathrm{FOV}}$
NGC 6482	1140 ± 87	-21.65	-23.20	-21.95	1.89 ± 0.14
NGC 1132	3613 ± 295	-22.39	-23.84	-22.65	3.15 ± 0.26
ESO 306-G017	11577 ± 1046	-22.88	-24.38	-23.16	6.30 ± 0.57

TABLE 3.6: *Col. 1*: system; *Col. 2*: total number of GC in the FOV using the expected m^{0}_{g} and σ_{GCLF}; *Col. 3, 4* and *5*: absolute g, z and V magnitudes in the FOV, respectively; *Col. 6*: specific frequency in the FOV.

the sky values estimated from the Sérsic fits. Then, we apply the transformation $V = g + 0.320 - 0.399(g-z)$ given by Kormendy et al. (2009) to obtain the absolute V magnitude in the FOV. For the N_{GC}, although the parameters recovered from the GCLF fitting are consistent with expectations for NGC 1132 and ESO 306-G017, they are not for NGC 6482. Thus, to estimate S_{N} we use the expected turnover magnitudes (Col. 7 in Table 3.1) and fix $\sigma_{\mathrm{GCLF}}=1.4$ to calculate more conservative values of the total GC number, $N_{\mathrm{GC},0}^{\mathrm{total}}$, for the three FGs. Although we do not fit for the GCLF parameters in this case, their uncertainties are included in our error estimates for the total GC numbers. The resulting values of $N_{\mathrm{GC},0}^{\mathrm{total}}$ and their uncertainties are listed in Col. 2 of Table 3.6, and are generally consistent with the numbers estimated previously as part of the GCLF analysis in Sec. 3.5.3.

The specific frequencies of GCs and the absolute magnitudes of the FGs in the g , z and V bandpasses within the FOV are listed in Table 3.6. Both the GC population size and the S_{N} increase with the galaxy luminosity for these three FGs. There is a range of more than a factor of 3 in S_{N}, from $\lesssim 2$ for NGC 6482 to $\gtrsim 6$ for ESO 306-G017. This spans the full range of values for normal bright ellipticals in the Virgo cluster (see Section 1.2.1)

These results are largely independent of the galaxy profile fits, which are mainly used for estimating the sky background. In particular, although the unusually high Sérsic index $n \approx 11$ for ESO 306-G017 could in part result from the limited spatial range of the fitted profile, this would not affect the S_{N}, as we do not directly use the Sérsic fit to calculate the galaxy luminosity. Sun et al. (2004) found from much lower resolution ground-based imaging that the n value is lower for ESO 306-G017 at radii beyond the ACS FOV. Adopting a Sérsic profile with a lower n would result in a larger sky estimate, decreasing the luminosity and increasing the S_{N}.

However, if our estimated profile is accurate within the FOV, the estimated sky and S_{N} should also be accurate.

Finally, we could extrapolate the GC radial density profiles and the galaxy surface brightness fits in order to estimate the *global S_{N}*, or up to a certain physical radius; but the extrapolated galaxy profiles are very sensitive to the sky levels, which we cannot measure directly. Moreover, as noted above, there is evidence from the literature that an extrapolation of our Sérsic fit for ESO 306-G017 would not accurately describe its outer profile. The GC number density profiles in Fig. 3.15 also become very uncertain at large radii. We therefore opt to report the more reliable, directly observed, values within the FOV. The general tendency of GC systems to be more extended than the galaxy light means that the global S_{N} might be slightly higher.

3.6 Discussion

3.6.1 Comparison with Cluster Ellipticals

One of the most basic questions to address is whether the GC systems in these FG ellipticals differ from those of cluster ellipticals. To compare our results with the literature, we chose the ACSVCS sample of 100 early-type galaxies, comprising the largest and most homogeneous data set on the GC populations of cluster early-type galaxies. Moreover, the observations were taken with the same instrument and filters as the current study. The ACS Fornax Cluster Survey (Jordán et al. 2007a) targeted a sample of early-type galaxies in Fornax, but the complete results on the GC systems remain to be published. Cho et al. (2012) studied the GC systems in a smaller sample of elliptical galaxies in low-density environments, but the results were generally similar to those found for galaxies in Virgo.

Peng et al. (2006) found that the GC color distributions of the bright ACSVCS galaxies were essentially all bimodal, with mean GC color becoming redder for more luminous galaxies. Likewise, we find that the color distributions of the GCs in all three of our FG galaxies are bimodal. However, one surprising result is that the lowest luminosity FG galaxy NGC 6482 actually has the reddest mean GC

color, $\langle g-z \rangle = 1.26$ mag, equal to that of NGC4649 (M60), the ACSVCS galaxy with the reddest mean GC color.
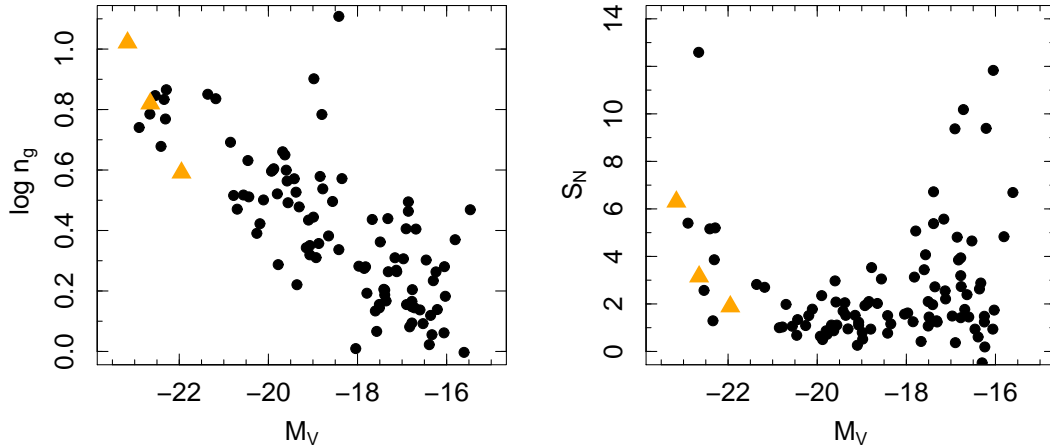

FIGURE 3.18: Fossil groups in context: galaxy Sérsic index in the g band (left) and S_N (right) are plotted as a function of M_V for the fossil groups studied here (orange triangles) and the ACS Virgo Cluster Survey galaxies (black circles). The Virgo data are from Ferrarese et al. (2006)and Peng et al. (2008).

The specific frequencies of the ACSVCS galaxies, and the implications for formation efficiencies, were investigated in detail by Peng et al. (2008). Even though the FOV encloses different physical scales due to different distances of the Virgo cluster and our FG galaxies, most of the ACSVCS galaxies are small enough to encompass the entire GC system in the FOV, while for the largest galaxies, an extrapolated value to large radius was reported. Although S_N tends to increase with luminosity among giant ellipticals, the mean S_N attains a minimum value of ~ 2 for early-type galaxies with $M_V \approx -20$, then increases again, but with much larger scatter, at lower luminosities. Fig. 3.18 (right panel) shows that the three FGs studied here follow the trend defined by the most luminous members of the 100 early-type ACSVCS galaxies. In particular, ESO 306-G017 has the highest luminosity in the combined sample, and its value of $S_N = 6.3$ is greater than that of all other 50+ galaxies with $M_V < -18$, except for M87, which is the extreme high-S_N outlier in this plot. The left panel of Fig. 3.18 shows that the FGs also follow the tendency of higher luminosity ellipticals to have larger Sérsic indices (Ferrarese et al. 2006). Thus, it appears that the FG galaxies accord well with the general S_N and surface brightness trends of normal giant ellipticals, and lack

(at least in this limited sample) the anomalously large S_N values seen in some cD galaxies, such as M87.

3.6.2 Comparisons with X-ray Data

The definition of FG includes a minimum X-ray luminosity. Thus, if an object is classified as FG, it must have been detected in X-rays. It has been noted that the X-ray luminosities of the extended halos of FGs are similar to those of the intracluster media in galaxy clusters (Mendes de Oliveira et al. 2009; Fasano et al. 2010). For each FG studied here, we show in Table 3.7 the literature values for its X-ray luminosity, metal abundance of the intragroup gas, and M/L ratio determined from X-ray data.

For NGC 6482, the luminosity was obtained from Khosroshahi et al. (2004), who analyzed *Chandra* data. They also noted a central point source, possibly an AGN. Yoshioka et al. (2004) analyzed *ASCA* data of NGC 1132, and classified it as an ''isolated X-ray overluminous elliptical galaxy'' (IOLEG). For ESO 306-G017, we use the results from Sun et al. (2004), who analyzed *Chandra* and *XMM-Newton* data and averaged the results of these analyses. They also noticed an X-ray *finger* emanating from the central X-ray peak to the brightest companion galaxy, similar in location to the optical tidal feature reported in the present study (see Sec. 3.4.1). The X-ray emission of this finger is 20%-30% brighter than other regions at the same radius.

System	$L_{X,bol}$ $(10^{42}h_{71}{}^{-2}\mathrm{erg\,s^{-1}})$	$Z/Z_\odot$	M/L $(\mathrm{M_\odot/L_\odot})$
NGC 6482	1.07	0.76 ± 0.28	71 [a]
NGC 1132	2.12	0.19 ± 0.1	180 [b]
ESO 306-G017	64.15 ± 0.26	0.44 ± 0.03	150 [a]

TABLE 3.7: *Col. 1*: system name; *Col. 2*: bolometric X-ray luminosity; *Col. 3*: metal abundance of the X-ray intragroup gas; *Col. 4*: mass-to-light ratio. [a] R band; [b] B band.

Table 3.7 includes the literature values of the M/L ratios. However, we must be cautious in comparing these values, because of different assumptions made

by different authors, mainly regarding the optical luminosity, and because of the large uncertainties in mass estimates (see Khosroshahi et al. 2007 discussion). For instance, Yoshioka et al. (2004) assumed a much lower contribution from the non-brightest galaxies to the total optical luminosity, compared with Khosroshahi et al. (2006) and Sun et al. (2004), a fact that increases their M/L estimate. Thus, systematic uncertainties can make it difficult to determine whether or not there exist any trend in GC properties with M/L.

While three objects are an insufficient sample for drawing general conclusions, we do see hints of interesting trends when comparing the properties of the X-ray gas and GC systems (Table 3.3). The results are consistent with positive correlations between X-ray luminosity, GC number, and S_N, similar to the trends found for BCGs (e.g., Blakeslee 1999; West et al. 1995). There may also be a tendency with optical luminosity. Intriguingly, the mean color of the GC population ($\langle g-z \rangle =$ 1.26, 1.11 and 1.20 for NGC 6482, NGC 1132 and ESO 306-G017, respectively) becomes redder as the metal abundance of the intragroup gas increases. The apparent correlations of the properties of the GC systems with X-ray intragroup gas abundance and galaxy luminosity suggest that these components might have likely formed at similar epochs.

One might expect the systems with the highest X-ray luminosities and masses to possess the most metal-rich GC systems, but this is apparently not the case for this small sample of FGs. Although the mean color of the GC system becomes redder with X-ray metallicity, as already mentioned, it does not correlate with X-ray luminosity. This could be an indication that the metal enrichment is not set mainly by the mass, but rather by the concentration of the halo (Atlee & Martini 2012). The dark matter concentration, c, is measured as the ratio of the virial radius to the radius of a sphere enclosing 20% of the virial mass (von Benda-Beckmann et al. 2008). Higher c values are associated with an earlier formation epoch (Khosroshahi et al. 2007; von Benda-Beckmann et al. 2008). Numerical simulations indicate that FGs have higher values of c than galaxy groups with similar masses but not classified as FGs ($c = 6.4$ for FGs and $c = 5.5$ for normal groups). The c values reported for NGC 6482, NGC 1132 and ESO 306-G017 are 60, 38 and 8.5, respectively (see Fig 9 from Khosroshahi et al. 2007); all of these are

high, with the value for NGC 6482 being quite extreme. However, the dark matter concentration on these scales is notoriously difficult to constrain observationally.

High concentrations can help fuel larger rates of star formation and a higher fraction of massive stellar systems such as GCs (Larsen & Richtler 2000; Peng et al. 2008), as well as a more efficient self-enrichment. Thus, the possible link between dark matter halo concentration, X-ray gas metallicity, and GC mean color may be understood in the context of early and violent dissipative assembly, whereby a first generation of GCs contaminates the surrounding media from which the bulk of the stars formed. Eventually, the feedback from star formation (and possibly AGN) heats the gas and suppresses subsequent star formation (see Johansson et al. 2012). Afterwards, the galaxy continues to grow by non-dissipative minor mergers (De Lucia et al. 2006; Naab et al. 2009). Of course, a larger sample of FGs is needed to confirm these correlations before drawing more detailed conclusions about the star formation histories of FG galaxies.

Chapter 4

Abell 1689

4.1 Description

Abell 1689 (hereafter A1689) is an extremely massive galaxy cluster located at $z = 0.183$, corresponding to a luminosity distance of 886 Mpc and an angular distance of 633 Mpc. It has a velocity dispersion $\sigma \gtrsim 1400$ km s^{-1}, and complex kinematical substructure (e.g., Teague et al. 1990; Girardi et al. 1997; Lemze et al. 2009). It has one of the largest known Einstein radii, and its mass distribution has been extensively studied from both strong and weak lensing (Tyson & Fischer 1995; Taylor et al. 1998; Broadhurst et al. 2005, Zekser et al. 2006; Limousin et al. 2007; Coe et al. 2010), as well as from X-ray properties (Andersson & Madejski 2004; Lemze et al. 2008). A recent multi-wavelength analysis by Sereno et al. (2013), including Sunyaev-Zeldovich, X-ray, and lensing data, finds a total mass $M_{200} = (1.3 \pm 0.2) \times 10^{15} M_\odot$ within $r_{200} = 2.1$ Mpc.

A1689 was one of the targets selected for early release observations with the ACS/WFC (Ford et al. 2002, 2003), after its installation on the *HST*.

Further inspection of these early ACS data revealed a concentration of faint point sources that were consistent with GCs at the distance of A1689. Assuming the usual Gaussian GCLF implied a huge population of $\gtrsim 10^5$ GCs (Blakeslee 2005), but the number was very uncertain, as it involved an extrapolation by two orders of magnitude.
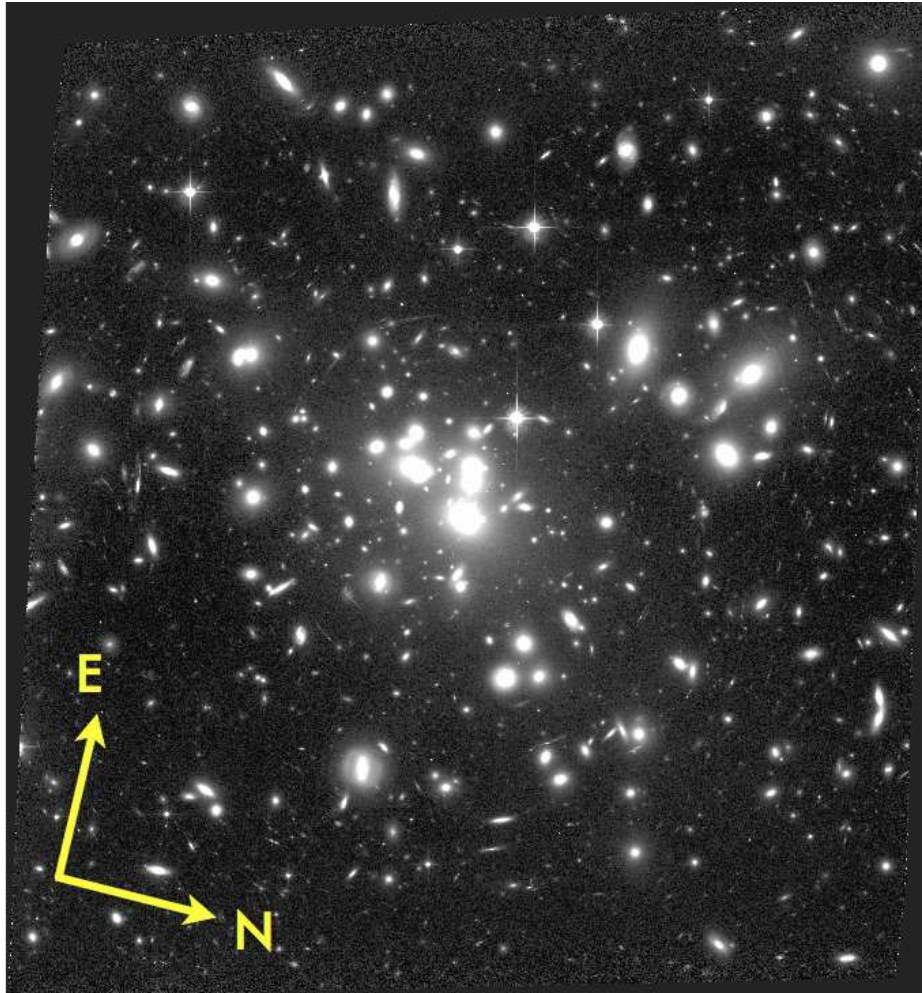
FIGURE 4.1: Deep ACS/WFC F814W image of the galaxy cluster A1689 from program GO-11710, shown in the observed orientation. The field-of-view is $\sim 3\overset{'}{.}3 \times 3\overset{'}{.}3$.

We obtained a very deep image of A1689 in order to go deeper in the GCLF than all previous observations, with the goal of exploring the relationship between GCs and both dark and baryonic matter. Furthermore, we would be able to test the existence of a universal ϵ_t (GC formation efficiency per total mass, $\epsilon_t = \mathcal{M}_{GC}/\mathcal{M}_{total}$) in an extreme system: a distant and one of the most massive galaxy clusters.

4.2 Observations and Data Reduction

As part of *HST* program GO-11710 (P.I: J. Blakeslee), we imaged the central field of A1689 for 28 orbits in the $F814W$ bandpass (also referred to as I_{814}) of the ACS/WFC. The individual exposures were processed with Apsis (Blakeslee et al. 2003) to produce a single geometrically corrected, cosmic-ray cleaned, stacked image with a total exposure time of 75,172 s, and an output pixel scale of $0\rlap{.}''033$ pix^{-1}. At nearly 21 hr, this is the single deepest ACS/WFC image in the F814W bandpass.

We calibrated the photometry on the AB system, using the F814W zero point of 25.947 determined from the time-dependent ACS Zeropoint Calculator.[1] The I_{814}-band Galactic extinction in the direction of A1689 is 0.04 mag (Schlafly & Finkbeiner 2011).

Throughout this chapter, we adopt the WMAP7 maximum likelihood cosmology (Komatsu et al. 2011) with $(h, \Omega_m, \Omega_\lambda) = (0.704, 0.27, 0.73)$, which yields a distance modulus for A1689 of $(m-M) = 39.74$, mag and a physical scale of 3.07 kpc arcsec^{-1}.

4.3 Analysis

As one of the few richness class 4 clusters in the Abell catalogue (Abell et al. 1989), A1689 is exceptionally rich in galaxies, particularly in its central region (Figure 4.1), a fact that hampers source detection and photometry.

4.3.1 Galaxy Modeling

In order to have an image with the flattest background possible, we follow the same procedure described in Section 3.4.1, using the `ellipse` and `bmodel` tasks within IRAF to construct isophotal models for 59 of the brightest galaxies in the

---

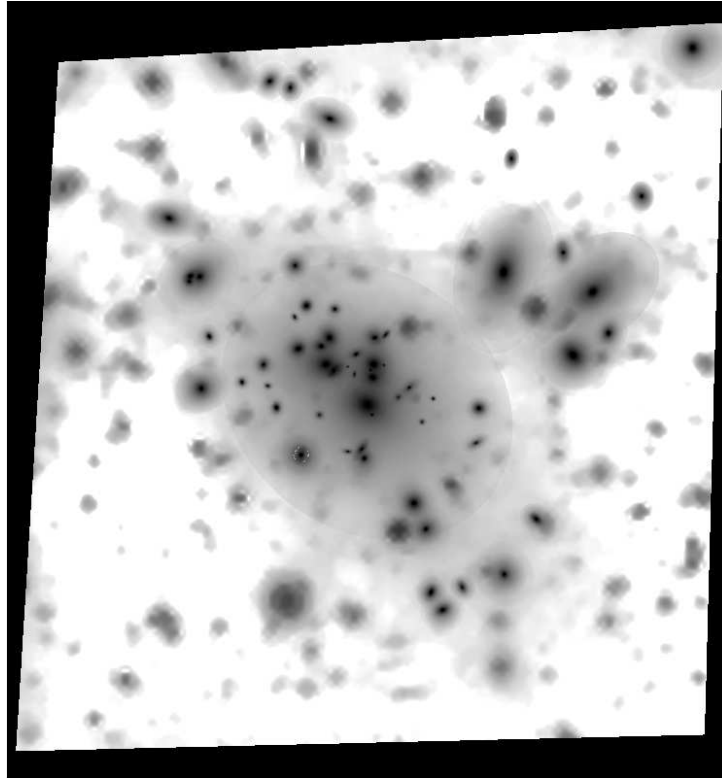[1]http://www.stsci.edu/hst/acs/analysis/zeropoints.

FIGURE 4.2: Final luminosity model of A1689 (*bmodel* plus SExtractor back-
ground map).

ACS/WFC field. Neighboring galaxies were masked during the fitting, and in
cases with very close companions, it was necessary to perform several iterations.

The isophotal models for the 59 galaxies were combined to produce a single *bmodel*
image, which was then subtracted from the original image to create a first-pass
residual image. SExtractor was then run on this residual image to generate a
map of the background due to the imperfect subtraction of the galaxies, as well as
approximate representations of other, unmodeled, cluster galaxies. The SExtractor
background map was then combined with the *ellipse/bmodel* models to produce
our final luminosity model, and this was subtracted from the original image to
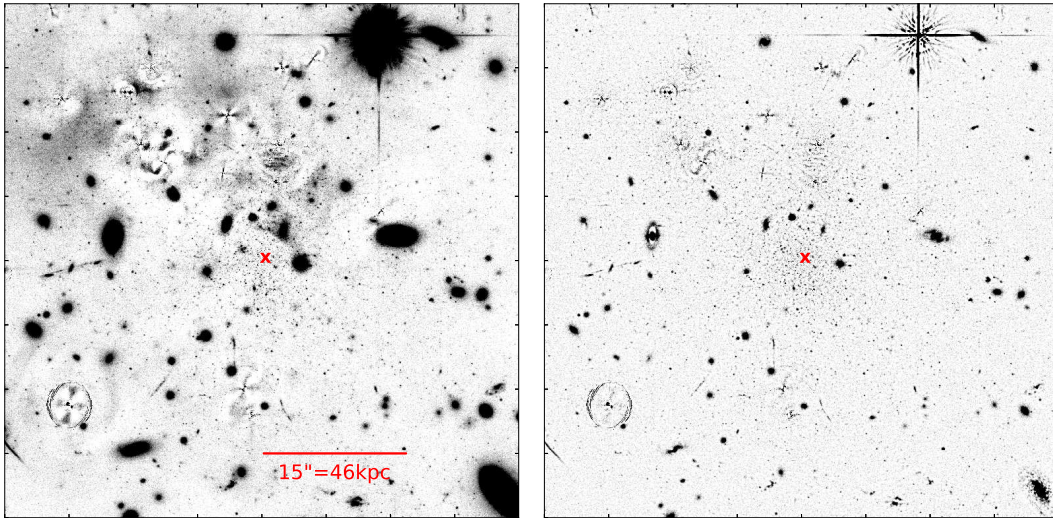obtain what we refer to as the *final_residual* image.

FIGURE 4.3: Zoom to the central region ($\sim 160{\times}160$ kpc) of A1689. The red cross marks the center of the cD galaxy. *Left panel:* residual after subtraction of the luminosity model (*bmodel* plus SExtractor background map); because of its shallow light profile, the cD galaxy itself subtracts very well. *Right panel*: residual after subtraction of the luminosity model and the smooth rmedian image, used only for object detection.

4.3.2 Object Detection

The final_residual image includes many smaller galaxies and residuals from larger galaxies that were difficult to model and are not well represented by the SExtractor background map. To remove these smaller (but resolved) structures, a smoothed image was created by applying the IRAF task `rmedian` (a ring median filter with inner and outer radii of 5 and 9 pix, respectively) to the final_residual image. This ring-median image was then subtracted from the final_residual to obtain the *rmed_residual* image (Figure 4.3). Although the rmed_residual image is extremely flat and suitable for point source detection, it cannot be used to measure reliable source magnitudes, as some flux is removed by the rmedian process.

The source detection was performed with SExtractor on the rmed_residual image. In order to make the detection more robust, we used an RMS error image for the SExtractor detection WEIGHT map, produced as described by Jordán et al. (2004). This RMS map includes detector and photometric noise, as well as the signal-to-noise variations from the corrected bad pixels and cosmic rays. Bright stars, diffraction spikes, areas of lower exposure time near the image edges, and
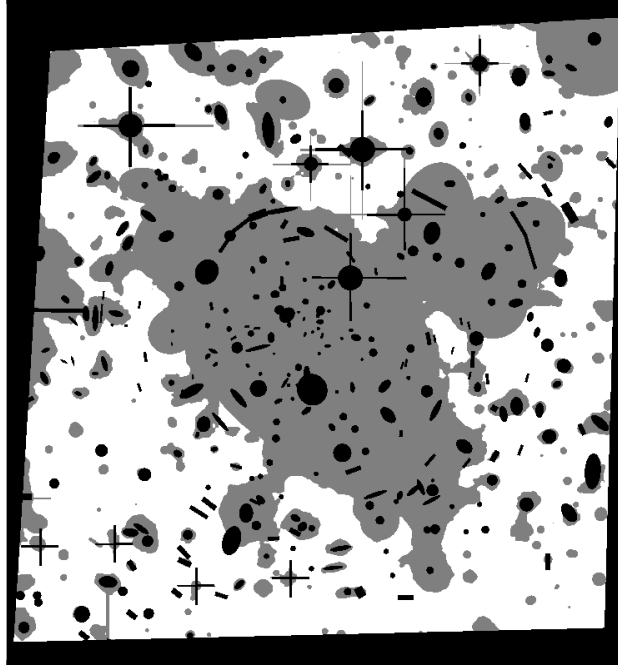
FIGURE 4.4: Black regions: areas masked throughout the entire analysis; gray regions: mask applied to the galaxies, including the cD, used in estimating the number of background contaminants, *bg*.

regions with large model residuals (due to sharp or irregular features within the cluster galaxies) were masked during the detection (black regions in Figure 4.4). At a luminosity distance of 885 Mpc, the GCs appear as point sources, and the SExtractor parameters were chosen to optimize point source detection, using a threshold of 5 or more connected pixels at least 1.5 σ above the local background, which gives a threshold of $\geq 3.35\sigma$.

Source magnitudes were measured on the final residual image with PSF photometry, using the SExtractor output coordinates. The PSF photometry is more accurate than the various aperture magnitudes measured by SExtractor. The PSF was constructed using the standard DAOPHOT (Stetson 1987) procedure. The important parameters were the FWHM of the PSF, fwhmpsf $= 2.6$ pix ($0\rlap{.}''086$), aperture $= 4$ pix, and varorder $= 2$, which means that the PSF is quadratically variable over the image. The best fitting function to describe the PSF was *penny1*, an elliptical Gaussian core, that can be tilted at an arbitrary angle, with Lorentzian wings. Figure 4.5 shows the subtraction of point sources using the modeled PSF.
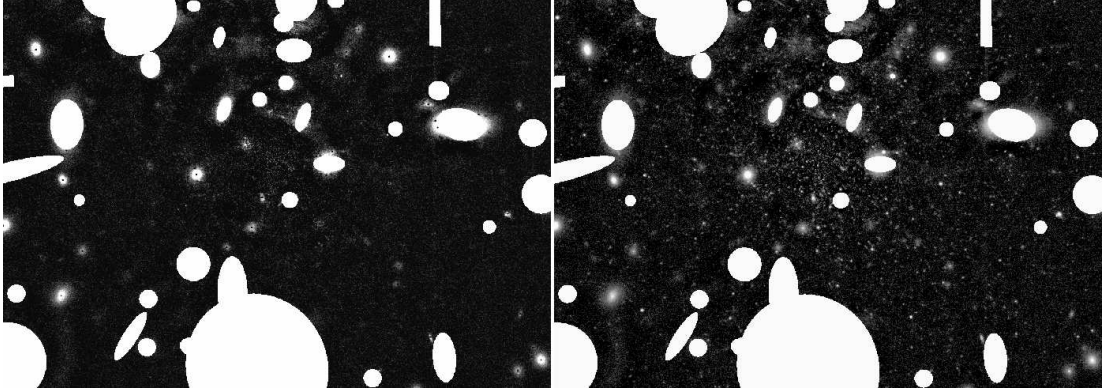
FIGURE 4.5: Zoom to the A1689 center. *Left panel:* residual image after subtraction of point sources using the constructed PSF. *Right panel*: residual image with point sources.

The fact that no residuals are seen around the point sources, indicates that the model is fairly accurate.

Since the radius of the PSF model is finite, an aperture correction, m_{apcor}, was estimated. To this end, first the magnitude difference between 4 and 15 pixels ($\sim 0\rlap{.}''5$) was measured, then a correction from an aperture of $0\rlap{.}''5$ to infinity was obtained from Sirianni et al. (2005). The final aperture correction $m_{\mathrm{apcor}} = -0.36$ mag was applied to all the measured DAOPHOT fit magnitudes.

4.3.3 GC Candidate Selection

The DAOPHOT parameters χ_{DAO} and $sharp_{\mathrm{DAO}}$, which gauge the goodness of the PSF fit and profile sharpness for each object, together provide a good indication of whether an object is a point source. Based on input and output parameters of artificial stars constructed from the PSF, we selected as point sources objects with $\chi_{\mathrm{DAO}} < 5$ and $-0.9 < sharp_{\mathrm{DAO}} < 0.9$.

Assuming that they are similar to nearby globular clusters, the GCs in A1689 should appear at $I_{814} \gtrsim 27.0$. We therefore selected as GC candidates point sources having $27.0 < I_{814} < 29.32$; the faint limit is the magnitude where our detection is 50% complete in the innermost region of the cluster (see below). From this combined selection, we obtained a sample of 8212 GC candidates; Figure 4.6
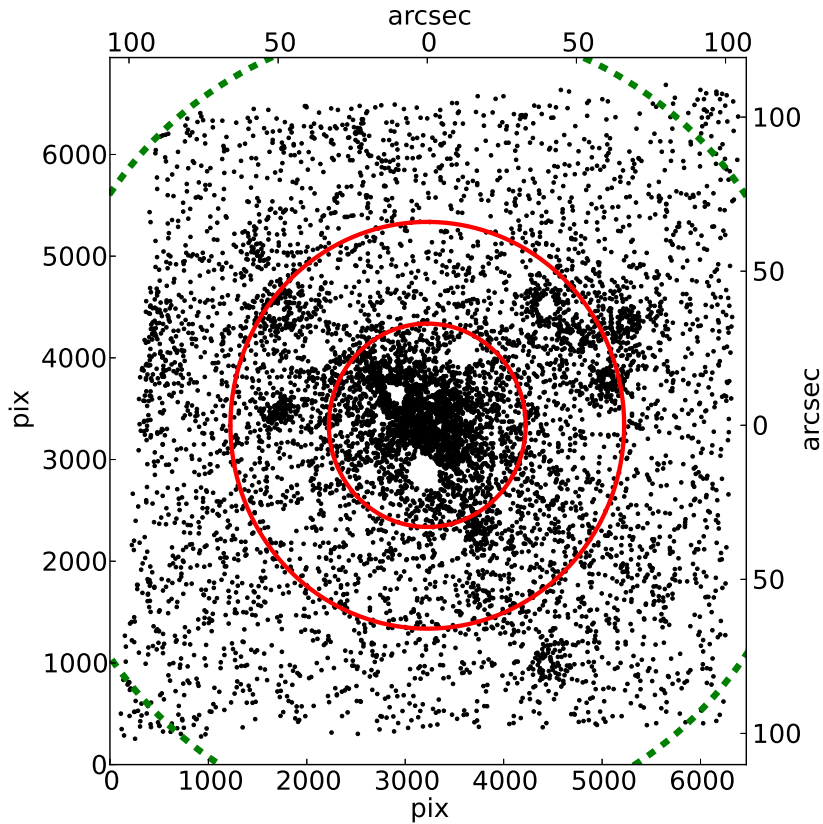
FIGURE 4.6: Spatial distribution of GC candidates. Red circles: boundaries of the three separate regions where the completeness function was fitted; green dashed circle: radius of 400 kpc (130″) from cluster center.

shows their x, y positions, which are strongly concentrated near the cD galaxy, but excesses of GC candidates are also visible around other cluster galaxies.

4.3.4 Completeness

To quantify the completeness, 250 000 artificial stars were constructed from the PSF model and added 500 at a time with random r, θ positions. The origin of the polar coordinates was the center of the cD galaxy, and the uniform random distribution in r yielded a higher density of sources near the cluster center, mimicking the actual sources. When adding the artificial sources, the masked areas were avoided, and the added sources were not allowed to overlap with each other. The artificial stars were added to the rmed_residual and final_residual images, and their fluxes measured with the same procedure that was followed for the real objects,
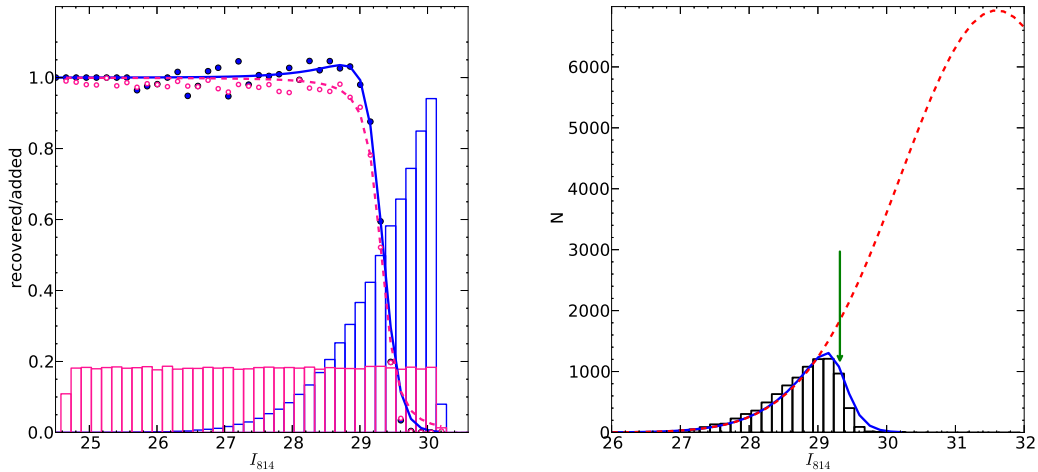
FIGURE 4.7: *Left panel:* completeness functions for the two different input magnitude distributions. *Histograms:* magnitude distributions of the artificial stars, i.e., a Gaussian with mean μ =31.6 mag and σ =1.5 mag (*blue*), and uniform (*pink*). The blue points and pink open circles are the respective recovered fractions, and the lines show the respective best-fit completeness functions: Pritchet (dashed pink line) and modified Fermi (solid blue line). The rising Gaussian distribution, meant to mimic the actual GCLF, causes an excess of recovered point sources near the completeness limit because of Eddington bias. *Right panel:* observed luminosity function of GC candidates (histogram); fitted modified Fermi function $\times$ Gaussian model (solid blue line); and derived Gaussian GCLF (dashed red line). The green arrow at I_{814} = 29.32 indicates the magnitude limit used for the fits.

including the selection based on the values of χ_{DAO} and *sharp* $_{\mathrm{DAO}}$. We carried out this whole process twice, using two different magnitude distributions for the artificial sources: (1) a uniform, or box-shaped, distribution with $25.0 < m < 30.5$; (2) a Gaussian distribution with mean μ =31.6, σ =1.5, and the constraint $m < 30.5$ (more than a magnitude fainter than the completeness limit). The latter case approximates the expected GCLF in A1689 (see Sec. 4.4.1); both distributions are illustrated in Figure 4.7. In the case of the uniform magnitude distribution, the fraction of recovered stars as a function of magnitude is well described by a Pritchet function (eq. 3.3, explained in Section 3.4.2).

In the case of the Gaussian magnitude distribution, the fraction of recovered stars actually exceeds unity before the steep drop in completeness sets in. This excess of detected sources is due to Eddington (1913a) bias: as a result of the steeply

rising luminosity function, measurement errors cause more faint sources to be scattered to brighter detection magnitudes, and relatively fewer bright sources to be scattered to fainter levels. In this case, including both magnitude bias and incompleteness, the recovered fraction is not well described by Eq. (3.3). However, we found that it could be represented by the following modified version of the Fermi function:

$$f^F(m) = \frac{1 + C \exp\left[b(m - m_0)\right]}{1 + \exp\left[a(m - m_0)\right]} , \qquad (4.1)$$

where m_0 is the magnitude at which the completeness would be 0.5 for a standard Fermi function ($C \equiv 0$). The other parameters are linked, but in rough terms, a controls the steepness of the cutoff, b (which must be $< a$) determines where the departure above unity begins, and C indicates the amplitude of the departure.

Although the Pritchet function and uniform magnitude distributions are widely used in the literature (as we did previously in Section 3.4.2), this analysis indicates that these assumptions require great caution: when the actual counts follow a steeply rising luminosity function, incompleteness corrections based on a uniform magnitude distribution overestimate the number of real sources. We adopt the results from the artificial star tests with the Gaussian magnitude distribution, since it more closely approximates the expected GCLF. The magnitude distribution of background sources is also a rising function, more similar to the bright side of the Gaussian than to the uniform distribution.

The ratios of recovered to added artificial stars as a function of recovered magnitude were calculated, and a modified Fermi function was fitted to the completeness fractions in three annular regions: from 0 to $33''$, from $33''$ to $1'1$, and beyond $1'1$ (red circles in Figure 4.6). The values of m_0 found for these three regions are 29.30, 29.35, and 29.33 mag, respectively. After applying the completeness corrections, the number of GC candidates brighter than our adopted limit $I_{814} < 29.32$ increases from 8212 to 8710±100, or 6%. Had we used the completeness estimates based on the uniform magnitude distribution, the increase would instead have been 14%, overestimating the final GC number by 7.5%.
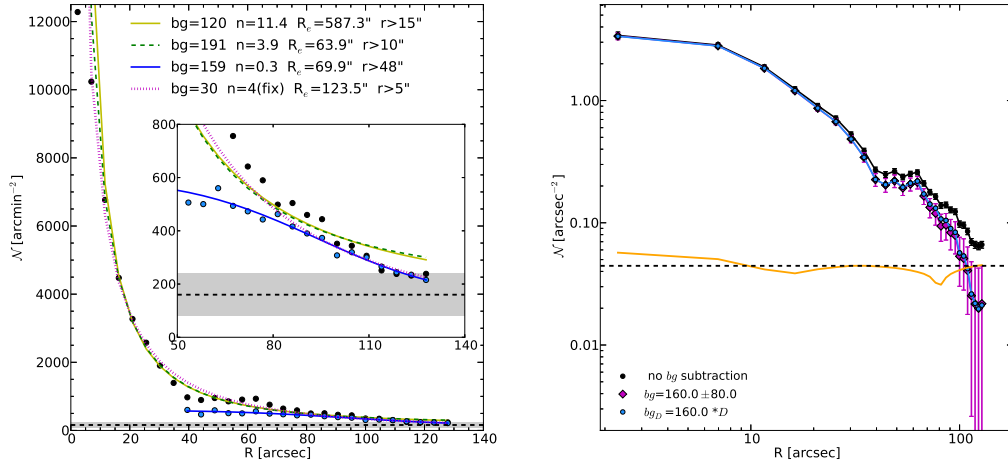
FIGURE 4.8: Radial distribution of the surface number density of GC candidates. *Left panel:* number of GC candidates per arcmin^2 (black dots). Dotted magenta, dashed green, and solid yellow lines: fitted Sérsic functions for different radial domains with the background (*bg*) as an additional free parameter. Blue dots: similar to black ones, but obtained after all the bright galaxies have been masked; blue line: corresponding Sérsic fit. The Sérsic parameters of the various fits are shown at the top of the figure. Dashed black line and gray shaded region: final adopted background and 1-σ error: $bg = (160 \pm 80)$ arcmin^{-2}. *Inset:* zoom of the outer parts of all fits. *Right panel:* logarithmic plot of the number of GC candidates per arcsec^2 without background subtraction (black dots); after subtracting a constant density of 160 arcmin^{-2} (magenta diamonds); and after subtracting $160 \times D$ arcmin^{-2} (blue dots), where D represents the expected profile of the background dilution over this magnitude range as a result of the lens magnification (see text). Dashed black line: value of 160 arcmin^{-2}; solid orange line: $160 \times D$ arcmin^{-2}.

4.3.5 Background Contamination

To estimate the number of background contaminants, *bg*, we follow a procedure different from the one used for the FGs, since there is no blank image with similar depth in I_{814} as the A1689 data. Thus, to estimate *bg*, we first calculate the number of GC candidates per unit area as a function of radius (Figure 4.8). Then, we fit to the surface number density profile, $\mathcal{N}(r)$, a Sérsic function (Section 2.1.1) plus

the background *bg* as a free parameter:

$$\mathcal{N}(r) = \mathcal{N}_e \exp\left\{-b_n\left[\left(\frac{r}{R_e}\right)^{1/n} - 1\right]\right\} + bg, \qquad (4.2)$$

where R_e is the effective radius that encloses half of the GC sample; $\mathcal{N}_e$ is $\mathcal{N}$ at R_e; n is the Sérsic index, which controls the shape of the profile; and $b_n \approx 1.9992n - 0.3271$ (Graham & Driver 2005).

We found that the fitted Sérsic parameters and background are very sensitive to the radial range of the fit. This is partly because of deviations from a smooth profile, but also because the number density of sources continues to decrease as a function of radius, without reaching a constant level. However, the mean background within our adopted magnitude limits must be in the range $0 < bg \lesssim 240$ arcmin^{-2} (the high value being the observed density in the outermost bins). After trying various radial cuts, we found that the most robust value of *bg* resulted from masking the regions around all the bright galaxies (gray region of Figure 4.4, based on our luminosity model). This procedure removes the concentrations of point sources associated with individual galaxies; the remaining objects follow a shallower, smoother radial density profile, shown in the left panel of Figure 4.8. The fitted background in this case was $bg \approx 160$ arcmin^{-2}, which lies within the broad range returned by the various fits prior to the galaxy masking (see examples in left panel of Figure 4.8). We adopt a conservative uncertainty of ± 80 arcmin^{-2}, where the error bar encompasses the unlikely case that all objects in the outermost radial bins are background objects.

We note that after masking the bright galaxies, the remaining objects (blue points in the left panel of Figure 4.8) may represent a smooth population of IGCs in A1689 (see Section 1.2.4). If we integrate the Sérsic function for these putative IGCs over the full area of the image (including masked regions, since IGCs would also be projected onto the galaxies), we find that 50% of the GC candidates are part of this smooth component. Of course, some of these objects will be associated with galaxies, since the spatial distributions of GCs are often more extended than the starlight. We therefore consider 50% to be an upper limit on the IGC fraction

within this central region. More detailed modeling of the GC distributions of individual galaxies, and wider coverage to trace the profile of the smooth component to larger radii, would help to refine this estimate.

Our estimate of the background is based on the outer parts of the ACS/WFC image, but in the case of A1689, it is necessary to make a radial-dependent correction for the effect of cluster lensing (Blakeslee 1999). The gravitational field of A1689 affects the spatial and magnitude distributions of the background sources. Following the formalism of Broadhurst et al. (1995), in the absence of lensing we expect a power-law distribution of background sources, $N_{\mathrm{bg}}(m) \approx N_0 10^{\beta \mathrm{m}}$, where N_0 is a constant, and β is the logarithmic slope of the counts. The lensing magnifies the brightness of the sources by the position-dependent magnification factor A, and thus shifts the source magnitudes brighter by $2.5 \log(A)$. It also increases the surface area by the same factor, and thus decreases the surface density. As a result, the effect of the lens magnification can be approximated as

$$N'_{bg}(m) = A^{-1} N_0 \, 10^{\beta(m+2.5 \log A)} = N_{\mathrm{bg}}(m) \, A^{-2.5(0.4-\beta)} , \qquad (4.3)$$

where N'_{bg} is the observed (lensed) number density. Generally, $\beta < 0.4$, so the background counts over a fixed magnitude range are decreased, or diluted, by a factor $D = A^{-2.5(0.4-\beta)}$. The counts can also be amplified ($D > 1$) in regions where $A < 1$ (see Broadhurst et al. 1995 for a detailed discussion).

The magnification A depends on the distance and mass distribution of the lens, as well as on the distance to the source plane. In general, it can be written as:

$$A = \frac{1}{\mid (1-\kappa)^2 - \gamma^2 \mid}, \qquad (4.4)$$

where κ and γ are the convergence and shear, respectively, for a given source distance. We use a non-parametric κ map for A1689 (M. J. Jee et al. 2013, in prep.; see also Jee et al. 2007), and since we are calculating the number densities in circular annuli, we adopt the spherical approximation $\gamma = \bar{\kappa} - \kappa$, where $\bar{\kappa}$ is the mean convergence interior to radius r. Taking $\beta = 0.35$ (e.g., Benítez et al. 2004), we finally derive the dilution factor D as a function of radius; the orange line in the right panel of Figure 4.8 represents the product of D and the background at

large radii. The background level *bg* has been normalized to the outermost several bins; interior to these, the dilution is both negative and positive, depending on radius.

We note that Coe et al. (2010) also constructed a κ map for A1689 using their "LensPerfect" algorithm, and they reported the best-fitting Sérsic model parameters for the radially averaged profile. As a check, we derived a background source dilution profile using Coe et al.'s Sérsic parameters; the differences with respect to the above analysis were less than 1%.

Finally, we use the radial surface density distribution to correct for the incomplete area coverage (accounting for masked regions and incomplete outer annuli), out to a projected radius of 400 kpc (130″). This increases the sample of GC candidates to 10,596, and subtraction of the radially-dependent background contamination then gives a final sample of 8417±1096 GC candidates with $I_{814} < 29.32$ and $r < 400$ kpc.

4.4 Results and Discussion

After applying the corrections for incompleteness, partial area coverage, and background contamination, we end up with a sample of 8417 GCs with $m < 29.32$ and within $r < 400$ kpc of the central cD galaxy in A1689.

4.4.1 Total GC Number and Specific Frequency

To estimate the total size of the GC population, we assume that the GCLF is similar to those studied in massive ellipticals in more nearby clusters (Section 1.2.3). Based on these works, the absolute I_{814}-band GCLF turnover should occur at $M_{814}^{\mathrm{TO}} = -8.10\pm0.10$ AB mag. However, the observed I_{814}-band corresponds to a different range of wavelengths in the rest frame of A1689, the so-called K-correction (Humason et al. 1956). Thus, including the distance modulus, Galactic extinction, and a K-correction in F814W of 0.03 mag (calculated for a GC spectrum at this redshift) implies an apparent turnover magnitude of 31.71 mag.
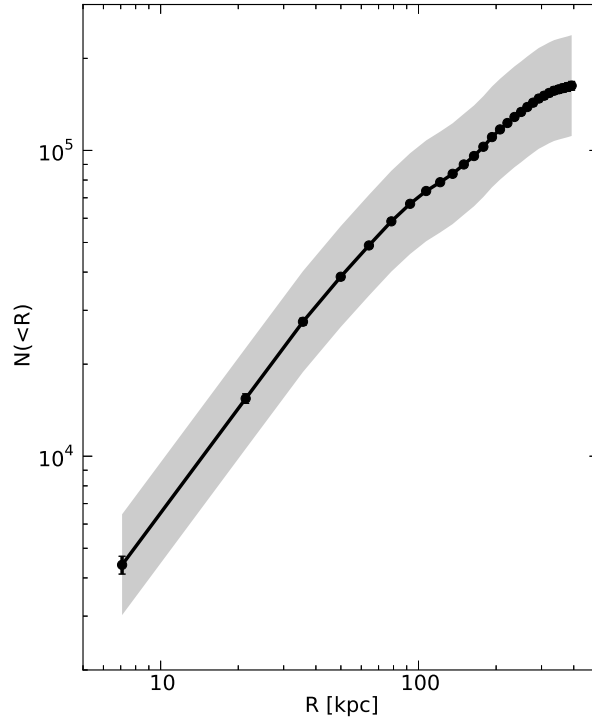
FIGURE 4.9: Cumulative radial profile of the total number of GCs corrected for magnitude and area incompleteness and background contamination, then extrapolated over the GCLF. Gray region: uncertainty due to the GCLF parameters.

However, the lookback time to z=0.183 is 2.25 Gyr, and stellar population models (Bruzual & Charlot 2003) indicate that old, metal-poor systems such as GCs would have been ~ 0.15 mag more luminous at this epoch. We therefore adopt an apparent turnover magnitude $m_{814}^{\rm TO} = 31.6 \pm 0.2$ AB and use a Gaussian width $\sigma_{\rm LF} = 1.4 \pm 0.1$ mag.

The extrapolated total population of GCs within $r < 400$ kpc is then $N_{\rm GC}^{\rm total}$=162,850$\pm_{51310}^{75450}$. The main source of error comes from the uncertainty in the GCLF parameters; for instance, using $\sigma_{\rm LF} = 1.3$ increases $N_{\rm GC}^{\rm total}$ by 30%. Figure 4.9 shows the radial cumulative profile of $N_{\rm GC}$, including the uncertainties. For comparison, based on the Next Generation Virgo Survey (Ferrarese et al. 2012), the total number of GCs within the same 400 kpc radius of M87 in the center of the nearby Virgo cluster is 26,400±3,200 (P. Durrell et al., in preparation), a factor of six lower.

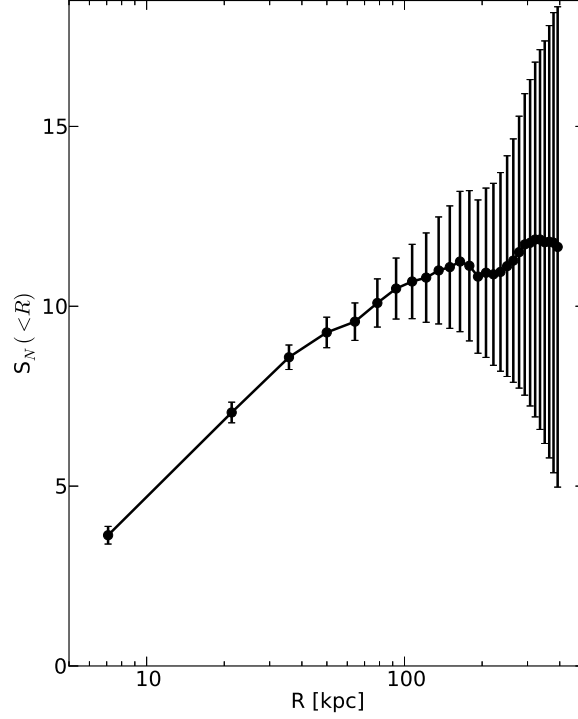FIGURE 4.10: Cumulative specific frequency S_{N} as a function of radius; the error bars include statistical uncertainties in the number of GCs for the assumed (fixed) GCLF and the uncertainty in the galaxy light profile.

To determine the specific frequency ($S_{\mathrm{N}} = N_{\mathrm{GC}}\,10^{0.4(M_{\mathrm{V}}+15)}$), we need to apply a photometric transformation to obtain M_{V}. The absolute magnitude M_V is derived as:

$$M_{\mathrm{V}} = I_{814} - (m{-}M) - A_{814} - K_{814} + (V{-}I_{814}) , \qquad (4.5)$$

where $(m{-}M)$ is the distance modulus, A_{814} is the Galactic extinction, K_{814} is the K-correction, and $(V{-}I_{814})$ is the rest-frame color. We calculate $K_{814} = 0.11$ mag for the spectral energy distribution of a giant elliptical at $z = 0.183$, and based on the extensive compilation of $(V{-}I)$ colors of galaxies by Tonry et al. (2001), we adopt $(V{-}I_{814}) = 0.83$, in order to obtain M_{V}. Figure 4.10 shows the resulting cumulative S_{N} as a function of radius, with the errors propagated from the GC counts and the galaxy luminosity. The uncertainty in the luminosity comes mainly from the assumed sky level $\mu_{814}^{\mathrm{sky}} = 20.90 \pm 0.01$ mag arcsec^{-2}, causing the size of the S_{N} error bars to increase strongly with radius.
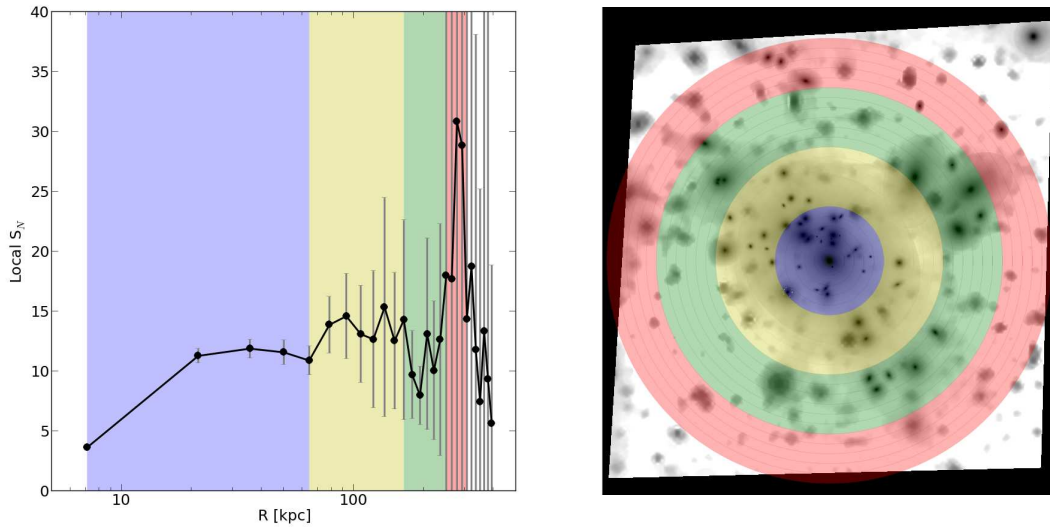
FIGURE 4.11: *Left panel:* local S_N within $\sim 5''$ annuli as a function of radius. *Right panel:* galaxy light model. In both panels, the blue, yellow, green and red regions indicate radial ranges of 0-70, 70-180, 180-230 and 230-300 kpc, respectively. The "dip" in the local S_N at $R \approx 200$ kpc is caused by the grouping of bright galaxies within the green annulus.

For comparison with nearby galaxies, we need to consider how S_N would evolve over a lookback time of 2.25 Gyr. There is no significant star formation in the A1689 early-type galaxies that dominate this central field (Balogh et al. 2002), and stellar population models that match the colors of nearby giant ellipticals (e.g., 10 Gyr, solar metallicity models of Bruzual & Charlot 2003) indicate that they have passively faded by about 0.20 mag since $z = 0.183$. Assuming negligible destruction of GCs in this time, the passive galaxy evolution will cause S_N to become 20% higher at $z = 0$ than at the observed epoch of A1689. Thus, the global value of $S_N = 11.7$ within 400 kpc would correspond to $S_N = 14.0$ at z=0, after correcting for passive evolution, similar to the S_N values observed for the central cD galaxies in the nearby Virgo, Coma, and Hydra clusters (Tamura et al. 2006; Peng et al. 2008, 2011; Harris et al. 2009; Wehner et al. 2008). Of course, for a more exact comparison, the S_N values should be estimated on similar physical scales. Blakeslee (1999) measured S_N within apertures of 40 and 65 kpc for the cores of six rich Abell clusters; he reported $\langle S_N(40) \rangle = 8.7$ and $\langle S_N(65) \rangle = 9.2$ (with rms scatters of ~ 2 in both cases). The corresponding values for A1689 at

z=0 would be $S_N(40)$=10.6±0.4 and $S_N(65)$=11.5±0.5, near the high end of the observed range for nearby massive clusters.

In addition to the cumulative S_N, it is also worth looking at the behavior of the local S_N. We have noted that the surface density distribution of GC candidates is not completely smooth, since they are preferentially located around the bright galaxies. This clustering causes the "bump" at $\sim 1\!'.1$ (200 kpc) in the GC radial density profile shown in Figure 4.8. Such feature in the GC density profile corresponds to a grouping of bright galaxies at this radius, as highlighted by the green annulus in the right panel of Figure 4.11. However, since the GCs are not perfect tracers of the stellar light, and their spatial concentrations are less sharply peaked than the galaxy profiles, an excess of galaxies at a given location around a cD galaxy with high S_N tends to *decrease* the local value of S_N, if the superposed galaxies have a "normal" $S_N \approx 4$. Therefore, at the same radius of 200 kpc where there is a bump in the number density of GCs, we actually find a dip in the local value of S_N, as shown by the green band in the left panel of Figure 4.11. A corresponding dip occurs near 200 kpc in the cumulative S_N distribution in Figure 4.10.

The scaling of N_{GC} in brightest cluster galaxies with the total underlying mass within a common projected radius has been interpreted as a consequence of an early universal GC formation efficiency in dense regions. Using the value 0.71±0.22 GCs per $10^9 M_\odot$ (Blakeslee 1999), our derived N_{GC}^{total} would predict a total mass of $\sim 2.3 \times 10^{14} M_\odot$ within 400 kpc in A1689. However, this estimate assumes that the GCs follow the same radial profile as the total matter distribution. While observations indicate that their spatial distribution is more extended than the starlight, until now it has not been possible to test how they relate to the dark matter distribution. We explore these issues in the following section.

4.4.2 Comparison of Mass Profiles

With the goal of testing the existence of a universal GC formation efficiency in an extreme system such as A1689, we compare the amounts of mass in this central field in the form of GCs, stars, hot intracluster gas, and total mass (including
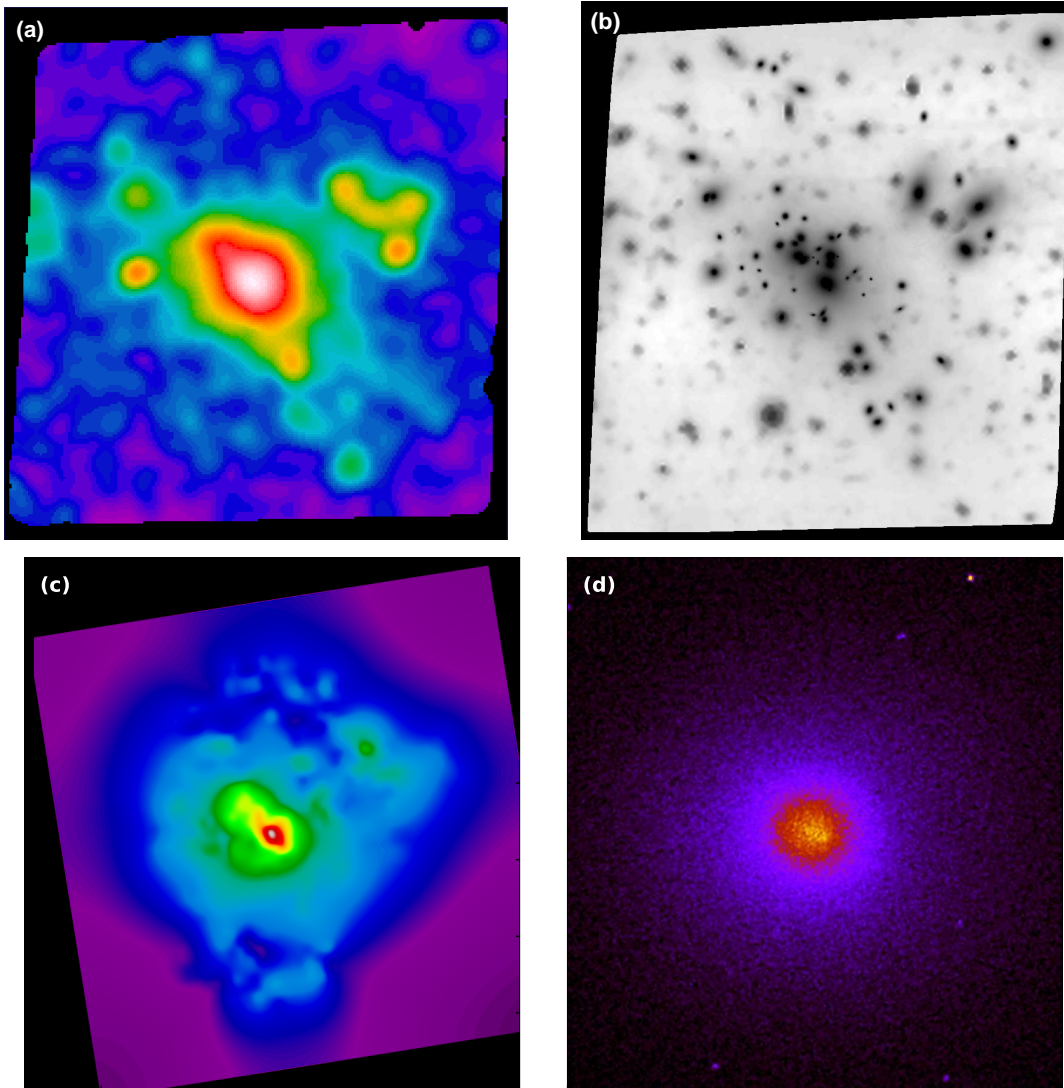
FIGURE 4.12: (*a*) Surface number density of GC candidates, smoothed with a Gaussian with FWHM = $10''$ (300 pix); (*b*) surface brightness distribution from isophotal models of 59 galaxies plus the SExtractor background map; (*c*) lensing-derived total surface mass density (includes baryonic and non-baryonic components); (*d*) X-ray surface brightness distribution (from *Chandra* archive).

dark matter). Figure 4.12 provides a 2-D visual comparison of the number density of GCs, the galaxy luminosity model, the lensing-derived mass distribution, and the X-ray emission map. The symmetry and smoothness of the X-ray gas stand out; this is not a resolution effect (as evidenced by the compactness of the X-ray point sources in the image). To make quantitative comparisons, we now derive the projected radial mass distribution for each component.

The total number of GCs within 400 kpc calculated in the preceding section can be converted to a mass by assuming a mean individual GC mass of $\langle \mathcal{M}_{\mathrm{GC}} \rangle = 2.4 \times 10^5 M_\odot$ (McLaughlin 1999; Blakeslee 1999). The estimated total mass in GCs within this radius is therefore $\mathcal{M}_{\mathrm{GC}}^{\mathrm{total}} = 3.9 \times 10^{10} M_\odot$. For perspective, this is equivalent to 60–80% of the total stellar mass of the Milky Way galaxy (Flynn et al. 2006; McMillan 2011).

To calculate the stellar mass $\mathcal{M}_\star$ we assume a $\mathcal{M}_\star / L_V = 4$, based on solar metallicity Bruzual & Charlot (2003) models with a Salpeter IMF (Section 2.2.1). Of course, the assumption of a constant $\mathcal{M}_\star / L_V$ at all radii is a first-order approximation. Moreover, the $\mathcal{M}_\star / L_V$, and thus the derived mass, can vary by $\sim 30\%$, depending on the IMF, but the choice of Salpeter is reasonable for early-type galaxies (e.g., van Dokkum & Conroy 2010; Conroy & van Dokkum 2012). Finally, using $M_{\mathrm{V},\odot} = 4.81$, we obtain $\mathcal{M}_\star^{\mathrm{total}} = 4.7 \times 10^{12} M_\odot$ within a circle of radius of 400 kpc.

The X-ray gas mass was estimated from the 3-D gas density profile $\rho_{\mathrm{g(r)}}$ constructed by Lemze et al. (2008), based on *Chandra* X-ray data. We found that the published $\rho_{\mathrm{g(r)}}$ is well fitted by a function of the form (Figure 4.13):

$$\rho_{\mathrm{g(r)}} = \frac{\rho_0}{[1 + (r/r_0)^\alpha]^\beta}, \tag{4.6}$$

with best-fit values $\rho_0 = 2.1 \times 10^{-25} \mathrm{g\,cm^{-3}}$, $r_0 = 321$ kpc, $\alpha = 0.58$, and $\beta = 5.6$ (giving $r^{-\alpha\beta} \sim r^{-3.2}$ at large r). These parameters are only used for interpolating the X-ray data points. We then integrate this function along the line of sight ℓ to obtain the projected gas mass surface density ζ as:

$$\zeta = 2 \int_0^{1\,\mathrm{Mpc}} \rho(\sqrt{R^2 + \ell^2}) d\ell, \tag{4.7}$$

where R is the projected radius. This gives an X-ray gas mass within 400 kpc of $\mathcal{M}_{\mathrm{Xray}}^{\mathrm{total}} = 3.6 \times 10^{13} M_\odot$. The baryonic mass comprises field stars, GCs, and intracluster gas. Adding all the components, we obtain $\mathcal{M}_{\mathrm{baryon}} \approx 4.1 \times 10^{13} M_\odot$.

The total mass, $\mathcal{M}_{\mathrm{total}}$, is estimated from the κ map used previously in Sec. 4.3.5. It includes both baryonic and non-baryonic mass, but is dominated by the non-baryonic component (at least outside the central few kpc). The convergence
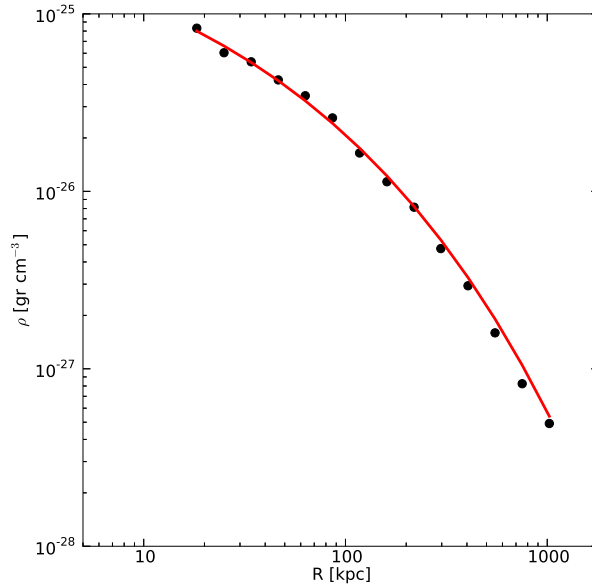
FIGURE 4.13: Dots: X-ray gas radial profile for A1689 by Lemze et al. (2008).
Overplotted is our fit with equation 4.4.2.

κ is the mass surface density, normalized by the critical surface density (i.e.,
$\kappa = \Sigma/\Sigma_{\text{crit}}$), where

$$\Sigma_{\text{crit}} = \frac{c^2 D_{\text{s}}}{4\pi G \, D_{\text{L}} D_{\text{Ls}}} \, ; \tag{4.8}$$

c is the speed of light; D_{L}, D_{s}, and D_{Ls} are the distances to the lens (A1689),
to a reference source (assumed to lie at $z = 3$), and from the lens to the source,
respectively. Integrating, we find $\mathcal{M}_{\text{total}} = 6.4 \times 10^{14} M_{\odot}$ within 400 kpc.

Figure 4.14 presents the radial mass density and cumulative mass profiles for each
of the above components. The stars and GCs are strongly concentrated in and
around galaxies; the most prominent feature is the bump at $R \approx 200$ kpc, discussed
above. The hot X-ray emitting gas and total mass exhibit much smoother profiles.
The hot gas dominates the baryonic mass beyond the central ~ 30 kpc.

To investigate the radial run of the GC mass fraction relative to the other mass
components, we plot in Figure 4.15 the mass ratios for all possible combinations of
the components in Figure 4.14. The stellar mass fraction in GCs ($\mathcal{M}_{\text{GC}}/\mathcal{M}_{\star}$, panel
f) increases by a factor of ~ 2.5 within the central 80 kpc, then levels off, consistent
with the S_{N} profile shown previously. However, compared to either the X-ray gas or
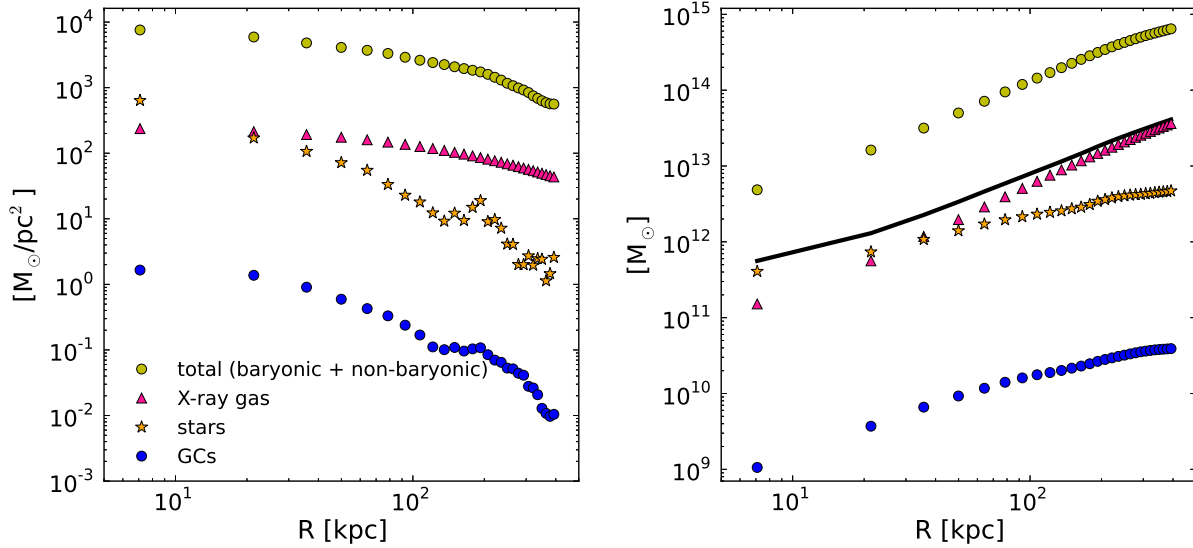
FIGURE 4.14: *Left panel:* radial mass density profile for each component. *Right panel:* cumulative mass profiles versus radius. The thick black line indicates the cumulative profile of the baryonic mass, $\mathcal{M}_{\mathrm{baryon}} = \mathcal{M}_{\mathrm{Xray}} + \mathcal{M}_{\star}$.

total matter, the GC mass fraction decreases faster as a function of radius (panels b and a, respectively); the mass fraction in stars (panels d and c) shows a similar, even steeper, decline. As found in previous studies, the gas mass fraction (panel e) appears to increase monotonically with radius. Interestingly, the baryonic mass fraction (ratio of baryons to total mass, panel g) reaches a minimum near 150 kpc, because the stellar mass is more concentrated than the dark matter, but the gas is more extended. This quantity has been studied extensively in galaxy clusters as an approximation to the baryonic mass fraction of the universe ($\mathcal{M}_{\mathrm{b}}/\mathcal{M}_{\mathrm{DM}} \sim \Omega_{\mathrm{b}}/\Omega_{\mathrm{DM}}$). For instance, Lin et al. (2012) measured baryon fractions for 94 galaxy clusters over a wide range of redshift; our value for A1689 in Figure 4.15 agrees well with the results of that recent study.

McLaughlin (1999) derived an average efficiency of GC formation per baryonic mass, i.e., $\epsilon_{\mathrm{b}} = \mathcal{M}_{\mathrm{GC}}/\mathcal{M}_{\mathrm{baryon}}$, of 0.0026 within $r < 100$ kpc. Comparing Mclaughlin's value to our estimate for the same radial range (Figure 4.15h), we find $\epsilon_{\mathrm{b}} = 0.0021$, which is within the scatter of the values found by McLaughlin. Meanwhile, Blakeslee (1999) reported a mean efficiency per total mass of $\epsilon_{\mathrm{t}} = \mathcal{M}_{\mathrm{GC}}/\mathcal{M}_{\mathrm{total}} =$

1.7×10^{-4} within $r < 50$ kpc; inside this radius, we obtain $\epsilon_t=1.8\times10^{-4}$ (Figure 4.15a), in close agreement with the value found by Blakeslee. However, although the mass ratios within these relatively small radii are remarkably consistent with the universal efficiencies previously proposed in the literature, the global values are not. Inside 400 kpc, we find $\epsilon_b^{A1689}=9.5\times10^{-4}$ and $\epsilon_t^{A1689}=6.1\times10^{-5}$, both a factor of 3 lower than the values cited above. After converting to our assumed mean GC mass, the results of Spitler & Forbes (2009) imply $\epsilon_t = 4.2\times10^{-5}$, about 30% lower than our value within 400 kpc but consistent within the errors; however, it is not clear what radius should be used in this case. Thus, we emphasize again the importance of comparing such ratios within the same physical radii.
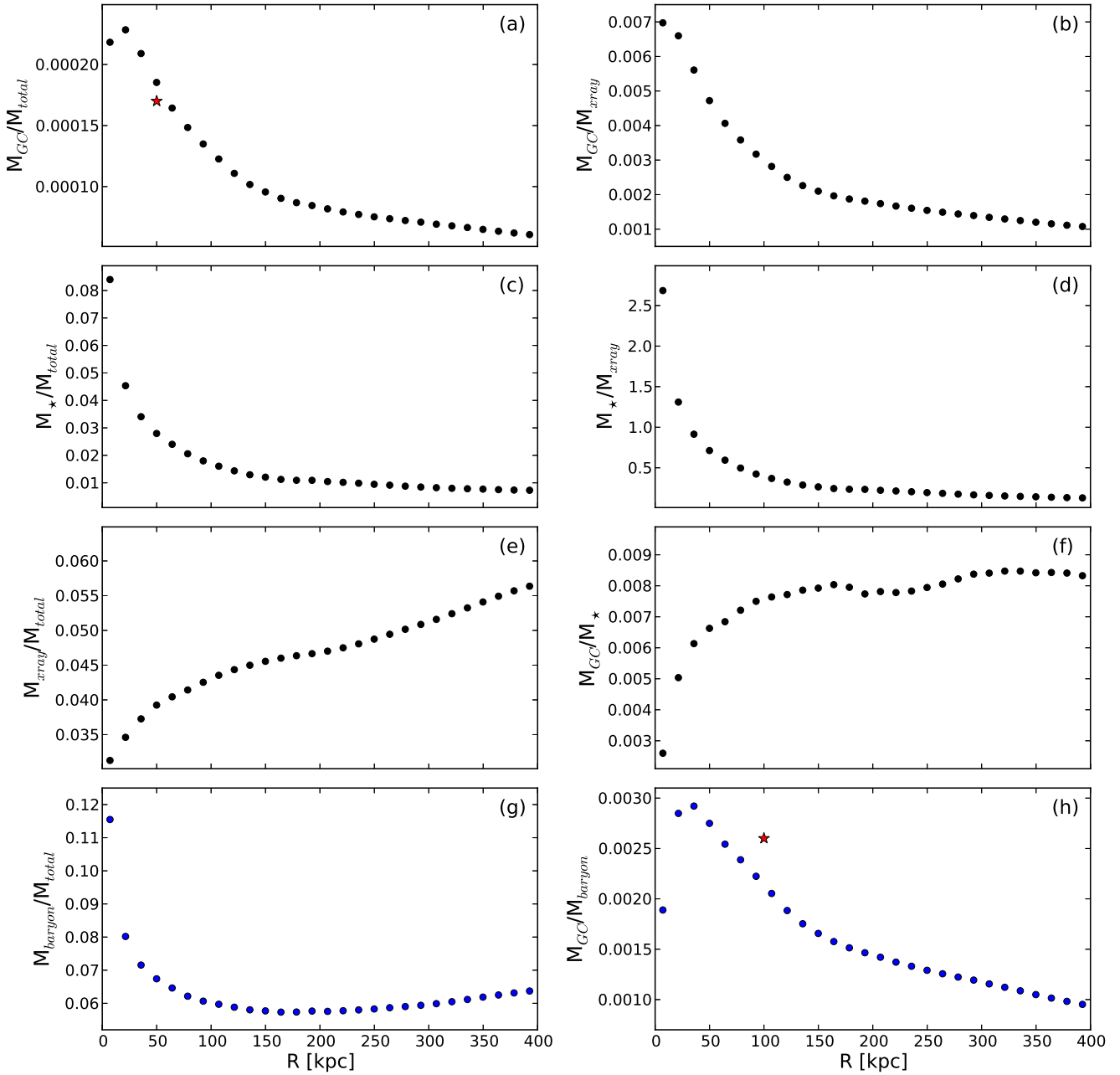
FIGURE 4.15: Ratios of the cumulative distributions for various mass components in A1689, based on the curves plotted in Fig. 4.14. The red stars in (*a*) and (*h*) represent the values $\epsilon_t = 1.7 \times 10^{-4}$ from Blakeslee (1999) and $\epsilon_b = 0.0026$ from McLaughlin (1999), respectively. See text for discussion. Note that the GC stellar mass fraction $\mathcal{M}_{GC}/\mathcal{M}_\star$ shown in panel (*f*) is equivalent to $S_\mathcal{M}/100$, where $S_\mathcal{M}$ is the "specific mass" parameter used in some studies (e.g., Peng et al. 2008).

4.5 Modeling of Individual Galaxies

As a follow-up study of the previous work, we are analysing the individual properties of the brightest 70 galaxies within A1689. Here we present the analysis of the first 59 galaxies (top panel in Figure 4.16), this is an ongoing work.

Sérsic profiles are fitted to each of the 59 bmodels (described in Section 4.3.1). We are following two different procedures for the fitting. The first one is a one-dimensional fitting. We fit a single Sérsic function to the μ_{SB} radial profile of each galaxy (red curves in Figure 4.17), except for the cD galaxy, to which we also fit a core-Sérsic function (Figure 4.18). Although the fits look good, we realize that the PSF component must still be included.

The second approach is to use the GALFIT [2] algorithm to obtain a two dimensional profile (bottom panel in Figure 4.16). It is worth mentioning that these models cover the whole image area, and can be extrapolated to a larger radius. One of the advantages of using GALFIT is that it can fit the convolution of the chosen function (in this case, Sérsic) plus a given PSF. In order to compare the 1D and 2D fits, we show in Figure 4.17 the Sérsic profiles produced by GALFIT (yellow dashed lines). However, as they have not been yet convolved with the PSF, large departures near the center are observed. Finally, we have constructed *empirical* μ_{SB} profiles from the GALFIT models, by measuring the mean μ_{SB} in ellipsoidal annuli (green solid lines in Figure 4.17).

The immediate future work is to produce profiles that include the convolution of the PSF and Sérsic functions. Then, we will follow the same procedure with the GC surface number density map (similar to panel *a* of Figure 4.12), in order to obtain Sérsic models of the spatial distribution of GCs for each galaxy. Afterwards, it will be straightforward to estimate the S_N for each galaxy, and to look for correlations with other properties (e.g., position within the cluster, luminosity, isophotal shape, effective radius, and Sérsic index n).

---

[2] Data analysis algorithm that fits 2-D analytic functions directly to digital images of galaxies and point sources. The available functions include: exponential, Sérsic /de Vaucouleurs, Nuker, Gaussian, King, Moffat, and PSF provided by the user (http://users.obs.carnegiescience.edu/peng/work/galfit/galfit.html).
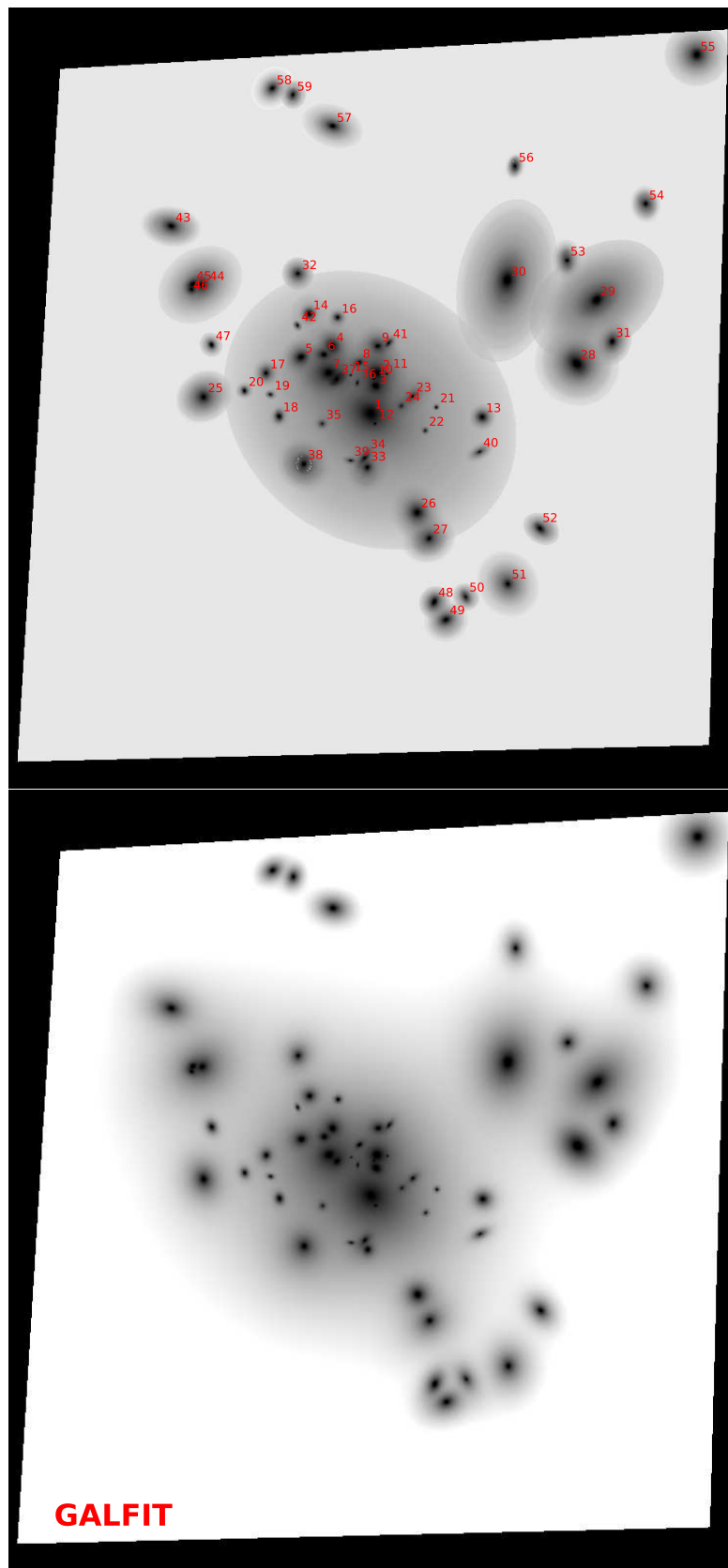
FIGURE 4.16: The 59 brightest galaxies within A1689. Top: bmodels constructed with ellipse/IRAF. Bottom: Sérsic models constructed with GALFIT.
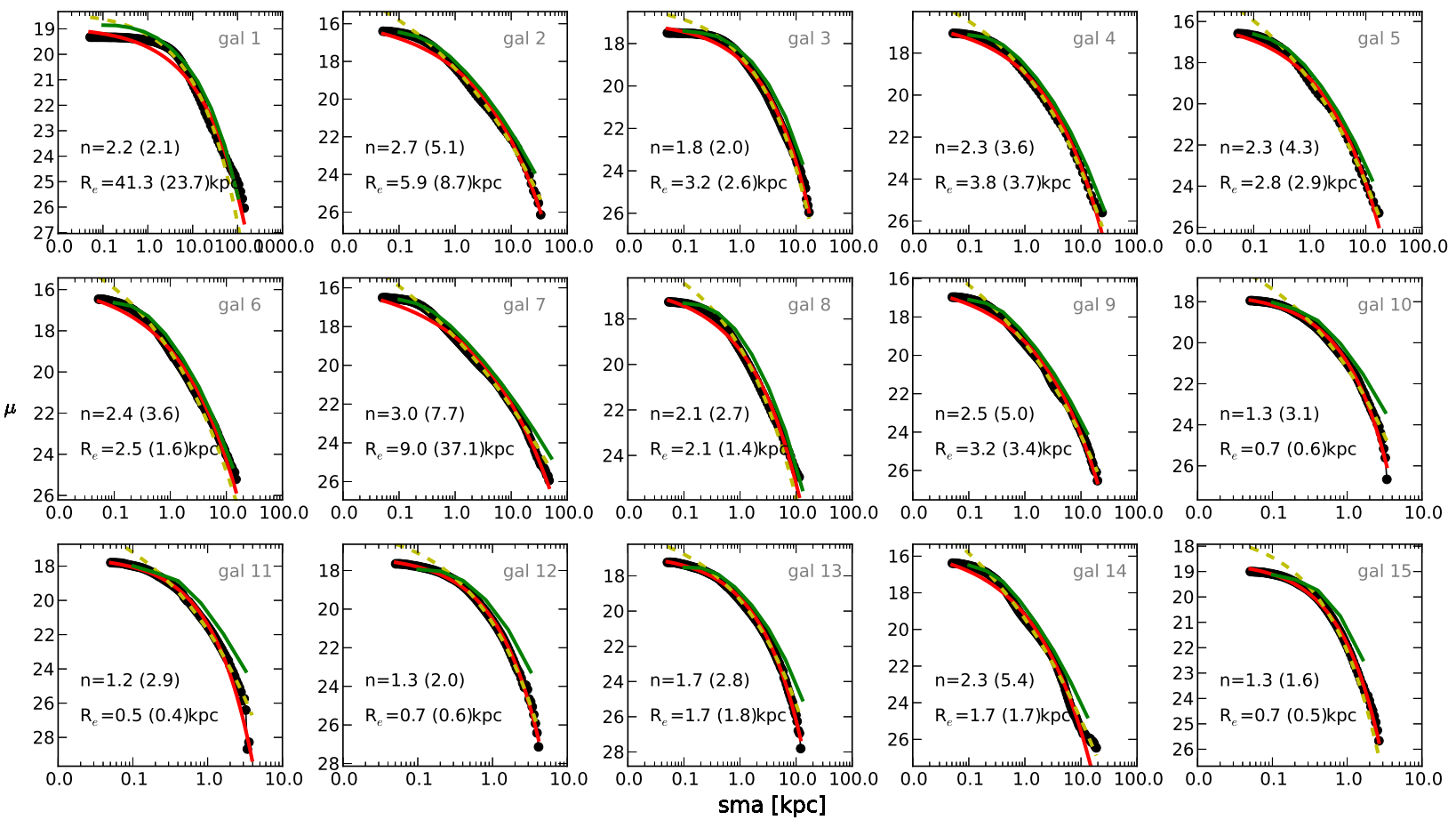
FIGURE 4.17: Surface brightness radial profiles of the brightest 59 galaxies in A1689 (black dots). The curves show the best Sérsic fit in 1D (red), GALFIT Sérsic 2D fit (yellow dashed), and μ_{SB} in ellipsoidal annuli form the GALFIT models (green). The corresponding n and R_e from the 1D fitting and GALFIT models (in parenthesis) are indicated.
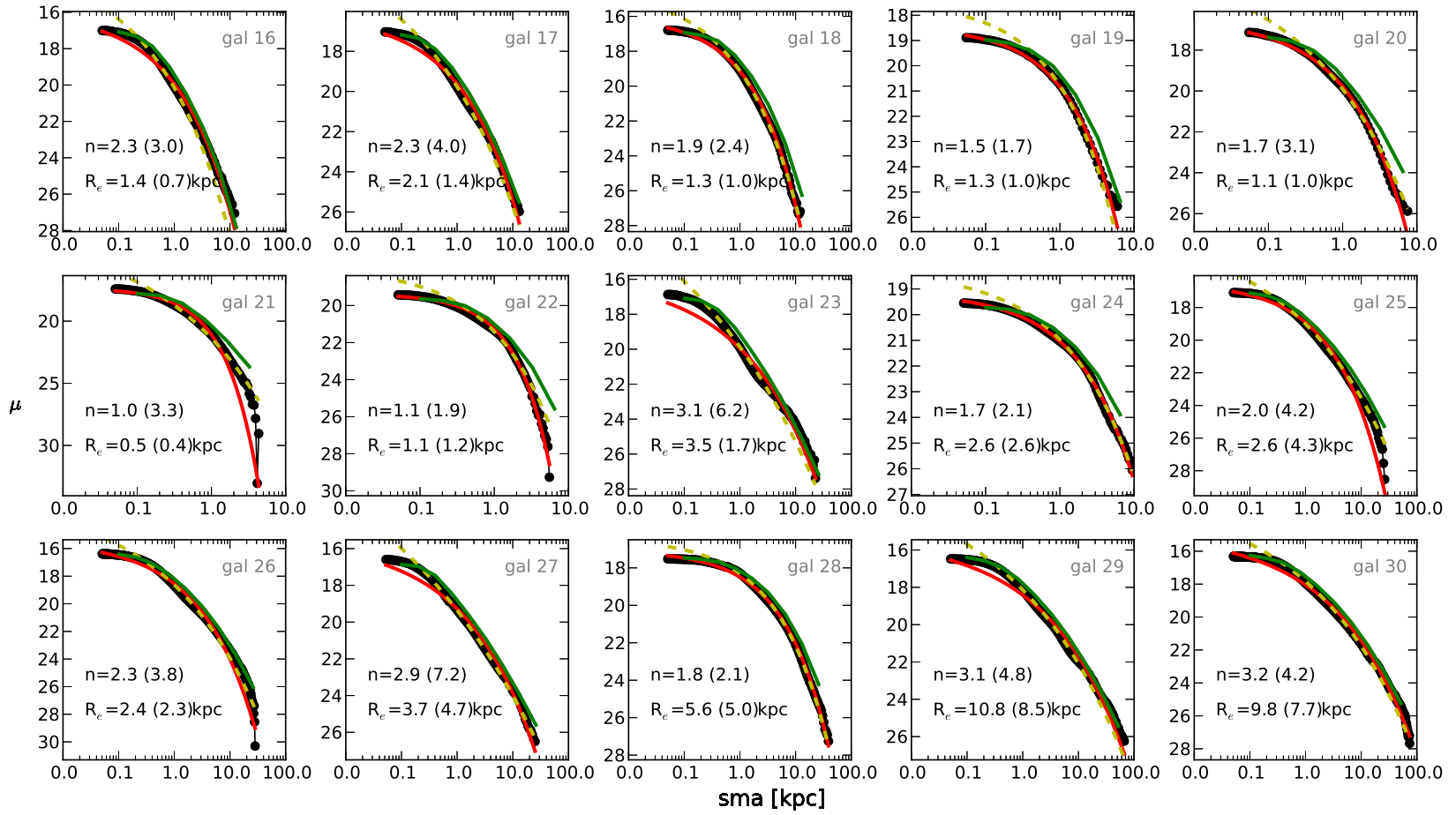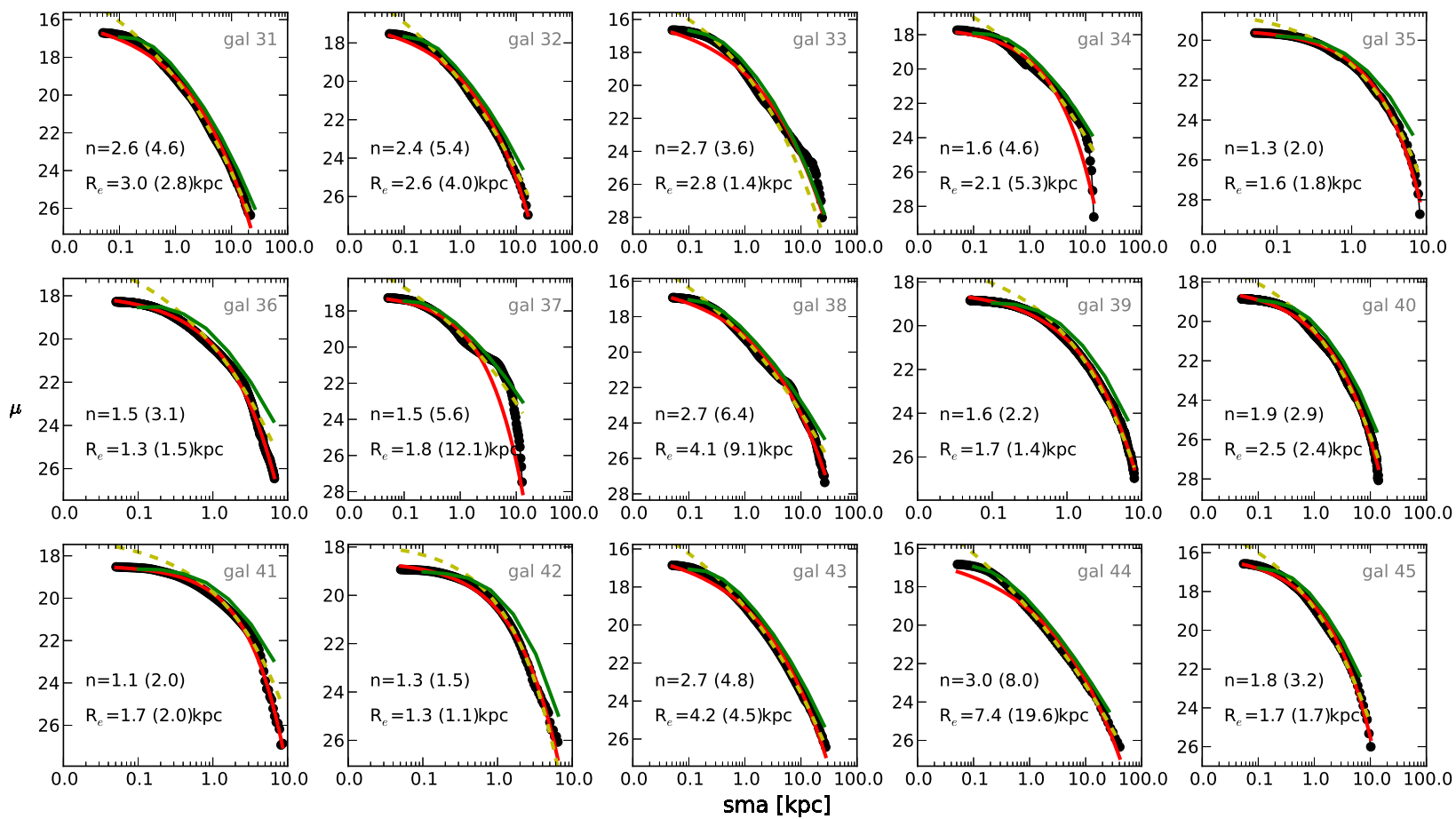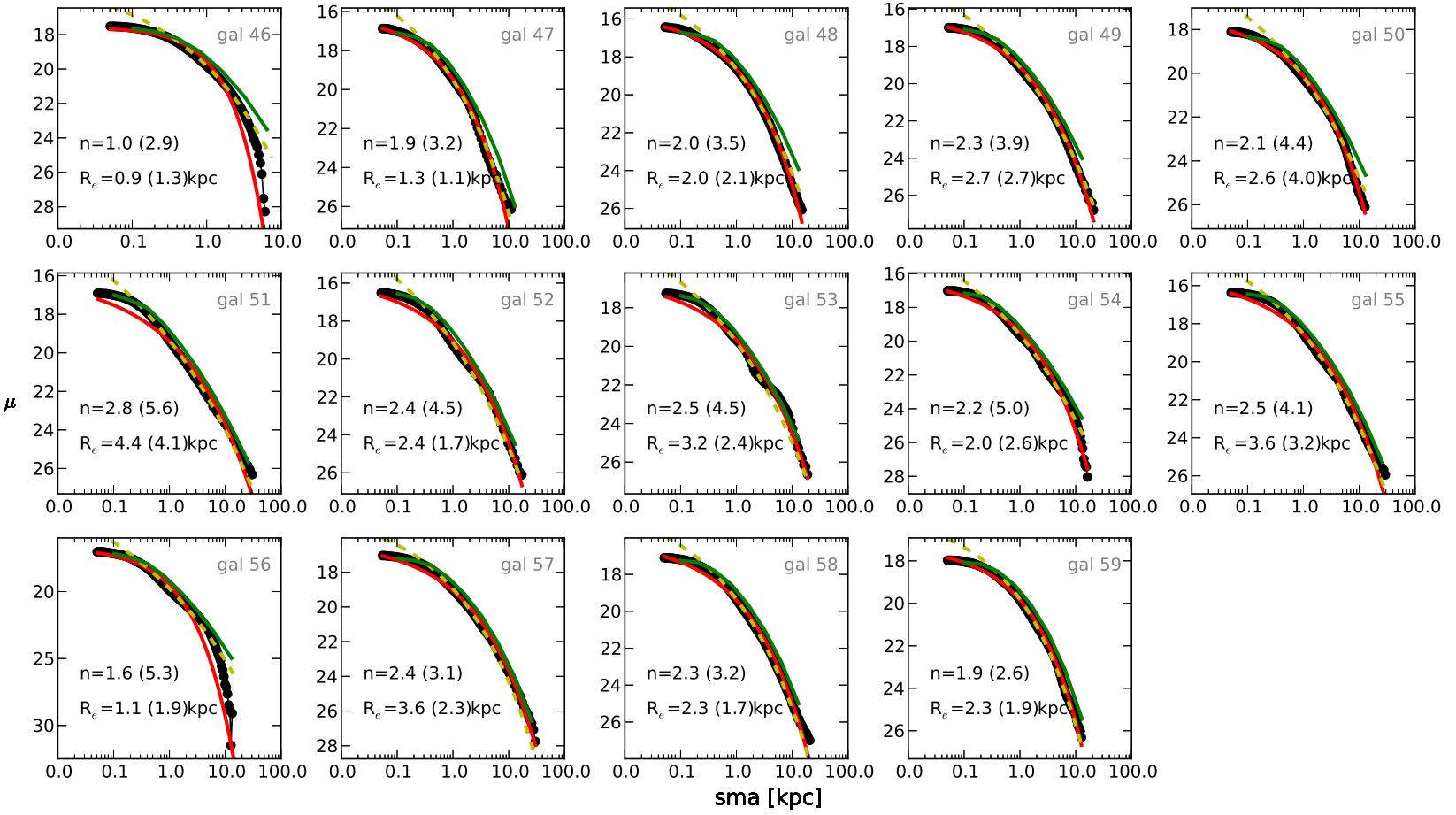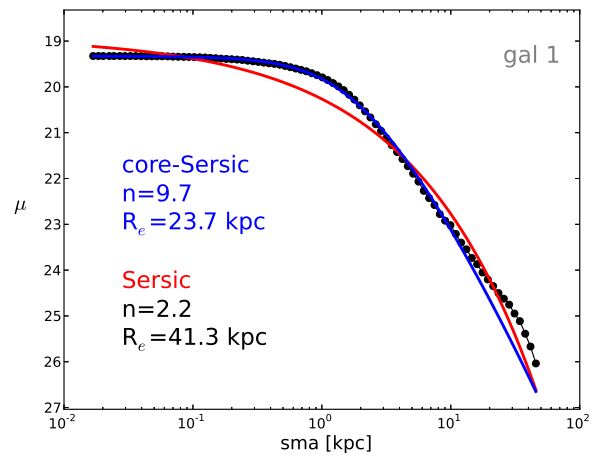
FIGURE 4.17: Continued

FIGURE 4.18: Surface brightness radial profile of the BCG in A1689 (black dots). The curves show the best single Sérsic fit (red) and the best core-Sérsic fit (blue).

Chapter 5

Conclusions

5.1 Fossil Groups

We have studied the globular cluster systems in three representative fossil group galaxies: the nearest (NGC 6482), the prototype (NGC 1132), and the most massive known to date (ESO 306-G017). This is the first systematic study of GC systems in fossil groups.

We detect 369, 1410 and 1918 GCs down to magnitude z=24.7, 26.2 and 26.2 in NGC 6482, NGC 1132 and ESO 306-G017, respectively; after completeness corrections and assuming a Gaussian GCLF with expected $M_{\mathrm{g}}^0 = -7.2$ and $\sigma_{\mathrm{GCLF}} = 1.4$, the number of GCs in each FOV are: 1140±87, 3613±295 and 11577±1046, respectively. The GC color distributions for all three FGs are better described by a bimodal, rather than a unimodal, Gaussian model. For the heteroscedastic cases, NGC 1132 and ESO 306-G017, the dispersion of the red population is wider than for the blue one. The mean $g-z$ colors are: 1.26, 1.11 and 1.20 for NGC 6482, NGC 1132 and ESO 306-G017, respectively. The mean color for the GCs of NGC 6482 is unusually red; it is interesting that this is also the FG with the highest X-ray gas metallicity.

For all three FGs, the spatial distribution of the starlight is more concentrated than that of the GCs, and the distribution of blue GCs are more extended than the red ones, similar to other ellipticals. The derived values of S_{N} are: 1.9 ± 0.1,

3.1 ± 0.3 and 6.3 ± 0.6 for NGC 6482, NGC 1132 and ESO 306-G017, respectively. These span the full range found for normal ellipticals in the Virgo cluster. Both the total number of GCs and the S_{N} increase with the optical luminosity of the galaxy and the X-ray luminosity of the intragroup gas.

From the analysis of the surface brightness distributions, we find evidence of recent interactions, particularly in ESO 306-G017, which shows a tidal feature coincident with the *finger* reported previously in X-rays, and in NGC 1132, which has shell-like structures. While NGC 6482 is well-described by a standard Sérsic profile, the two brighter galaxies are better fitted by core-Sérsic models. All three galaxies contain central dust features. These observations are consistent with numerical simulations indicating that signs of recent merging should be fairly common in first-ranked FG galaxies (Díaz-Giménez et al. 2008), and they suggest that the paradigm of FGs as relaxed, undisturbed systems needs to be reconsidered.

Using X-ray data from the literature, we find that luminosity and metallicity appear to correlate with the number of GCs and their mean color, respectively. Interestingly, although NGC 6482 has the lowest mass and luminosity in our sample, its GC system has the reddest mean color, and the surrounding X-ray gas has the highest metallicity.

Larger samples of GC systems in FGs are needed in order to make more definite conclusions. However, overall we conclude that the GC properties (colors, spatial distributions, specific frequencies) in FG central galaxies are generally similar to those seen in other giant ellipticals, which mainly reside in clusters. Although the environments differ, this study suggests that the GC systems formed under very similar conditions. These results might therefore be taken as a confirmation that the same basic formation processes are responsible for the buildup of massive early-type galaxies in all environments.

These results have been published in Alamo-Martínez, K. A., et al. 2012, A&A, 546, A15.

5.2   Abell 1689

Deep broadband imaging with *HST*/ACS ($\gtrsim 90\%$ complete to $I_{814} = 29$) has revealed an extremely rich GC system in the center of the massive lensing cluster A1689. The estimated total population of $162{,}850^{+75{,}450}_{-51{,}310}$ GCs within a projected radius of 400 kpc represents the largest system of GCs studied to date, six times the number within the same radius in the Virgo cluster. The large error bars are due to the uncertainty in the GCLF parameters. Although the Gaussian form of the GCLF is well calibrated for giant ellipticals in rich clusters, even with 20.9 hrs of integration, our data fall $1.6\,\sigma$ short of the GCLF turnover; we therefore sample only 10% of the GCs brighter than the turnover (or 5% of the total population, assuming a symmetric GCLF). Thus, the large extrapolation yields a sizable systematic uncertainty. Nevertheless, this remains the largest GC system yet discovered, with at least a factor of two more objects than the next most populous systems, including Coma and A3558 (Peng et al. 2011; Barber DeGraaff 2011).

Our analysis accounts for the effects of Eddington bias, gravitational magnification of the background surface density, redshifting of the bandpass (K-correction), and passive evolution of the GCLF. Although it is possible that there has been some evolution in the shape of the GCLF since $z = 0.18$, this would mainly occur by the destruction of low-mass GCs (e.g., Jordán et al. 2007; McLaughlin & Fall 2008), with a negligible effect on the masses of objects near the GCLF peak or brighter. Our assumption of a symmetric GCLF would therefore likely underestimate the population at $z = 0.18$, but the additional low-mass GCs would have affect little our total mass estimates.

The spatial distribution of GC candidates in the center of A1689 is not completely smooth; there are obvious concentrations around the cluster galaxies. However, by masking the bright and intermediate-luminosity galaxies, we can trace an apparently smooth component, which comprises half of the total population when integrated over the field (via the best-fit Sérsic model). If we identify these objects as belonging to a possible intracluster population of GCs, then there may be as many as $\sim 80{,}000$ such IGCs within the central 400 kpc in A1689. We consider this an upper limit, since some of these IGC candidates are undoubtedly bound

to individual galaxies. We plan to investigate this in more detail by modeling the GC distributions around individual galaxies. Imaging to a similar depth at larger radii from the cluster center would also help to constrain the IGC population.

The cumulative S_N increases from a value $\sim$5 within 10 kpc to 10$\pm$0.5 (not including systematic uncertainty from the GCLF) within 70 kpc. Although the uncertainties in S_N become large beyond 100 kpc, the profile appears to flatten, and the value within 150 kpc is $S_N = 11.1 \pm 2.0$. There is a clear dip in the cumulative S_N around 200 kpc, before it rises again to ~ 12 inside 300 kpc. The dip at 200 kpc occurs despite a local increase in the GC number density at the same radius; it is caused by a subgrouping of several bright galaxies which appear to have a more normal $S_N < 10$ (as was shown by comparing the green regions in Figure 4.11). Such galaxies contribute relatively more to the denominator of S_N than to the numerator. This highlights the fact that cannibalization of normal cluster galaxies by the central cD will tend to decrease the S_N, rather than increase it. Thus, the high S_N value must have been imprinted in the cluster core at early times. We have also noted that passive evolution of the galaxy luminosity since $z = 0.18$ would cause the observed S_N to increase by 20% at $z = 0$, but even with this effect, the high S_N in A1689 would not be anomalous among cD galaxies in local clusters.

Remarkably, the mass in GCs within 400 kpc of the center of A1689 is equivalent to 60-80% of the total stellar mass of the Milky Way. Integrated out to the virial radius of ~ 3 Mpc, the total mass in GCs is likely twice that of the stars in our Galaxy. Of course, this is a small fraction of the total mass in A1689. We have examined the mass profile of the GCs as a function of radius, and compared it to the mass profiles of the stellar light, hot intracluster gas, and total lensing-derived matter content within this central field. The mass profile of the GCs is somewhat more extended than the stellar light, but more concentrated than the hot gas or dark matter. If the mass fraction is viewed as a GC formation efficiency, then the efficiency (in terms of either baryonic or total mass) decreases as a function of radius, and there is no "universal" value.

On the other hand, when compared within the same physical radii, the GC mass fractions with respect to the total and baryonic masses agree with the values found

in samples of nearby clusters, all of which have masses lower than A1689. This suggests the possibility of a universal GC formation profile within galaxy clusters. In contrast, Laganá et al. (2011) estimated the stellar, intracluster gas, and total masses within r_{500} for 19 galaxy clusters, and found a decrease in the stellar mass fraction with increasing total mass of the system. That is, more massive clusters have lower overall star formation efficiencies. Taken together, these results are consistent with the view that the high S_N values in cD galaxies are a consequence of "missing" stellar light in more massive clusters (Blakeslee 1997), rather than of an excess in the number of globular clusters.

Finally, we note that in a recent study, Suárez-Madrigal et al. (2012) modeled the influence of the dark matter halo on molecular clouds at different locations within it. They found that the star formation efficiency of the clouds depends on the ambient density, and thus diminishes with distance from the halo center, in qualitative agreement with our finding that GC formation efficiency decreases with radius. If the mass density profiles in galaxy clusters are approximately universal (e.g., Navarro et al. 1997), then it would also make sense that the GC formation efficiency profile may follow a universal form. Further studies of the GC, baryonic, and total mass profiles in galaxy clusters are needed to test this intriguing possibility.

These results are published in Alamo-Martínez, K. A., et al. 2013, ApJ, 775, 20.

Bibliography

Abadi, M. G., Navarro, J. F., & Steinmetz, M. 2006, MNRAS, 365, 747

Abell, G. O., Corwin, H. G., Jr., & Olowin, R. P. 1989, ApJS, 70, 1

Anderson, J., & Bedin, L. R. 2010, PASP, 122, 1035

Andersson, K. E., & Madejski, G. M. 2004, ApJ, 607, 190

Arp, H. C. 1955, AJ, 60, 317

Ashman, K. M., & Zepf, S. E. 1992, ApJ, 384, 50

Atlee, D. W., & Martini, P. 2012, arXiv:1201.2957

Baade, W. 1944, ApJ, 100, 137

Baade, W. 1956, PASP, 68, 5

Balogh, M. L., Couch, W. J., Smail, I., Bower, R. G., & Glazebrook, K. 2002, MNRAS, 335, 10

Barber DeGraaff, R. G. 2011, Ph.D. Thesis, Washington State University

Bastian, N., Cabrera-Ziri, I., Davies, B., & Larsen, S. S. 2013, MNRAS, 436, 2852

Benítez, N., Ford, H., Bouwens, R., et al. 2004, ApJS, 150, 1

Bertin, E., & Arnouts, S. 1996, A&AS, 117, 393

Beuing, J., Dobereiner, S., Bohringer, H., & Bender, R. 1999, MNRAS, 302, 209

Binney, J., & Tremaine, S. 1987, Princeton, NJ, Princeton University Press, 1987, 747

Blakeslee, J. P., Tonry, J. L., & Metzger, M. R. 1997, AJ, 114, 482

Blakeslee, J. P. 1999, AJ, 118, 1506

Blakeslee, J. P., Anderson, K. R., Meurer, G. R. et al. 2003, *Astronomical Data Analysis Software and Systems XII* (ASP Conf. Ser. 295), ed. H. E. Payne, R. I. Jedrzejewski, & R. N. Hook (San Francisco, CA: ASP), 257

Blakeslee, J. P. 2005, Highlights of Astronomy, 13, 171

Blakeslee, J. P., Cho, H., Peng, E. W., et al. 2012, ApJ, 746, 88

Blanton, M. R., Hogg, D. W., Bahcall, N. A., et al. 2003, ApJ, 592, 819

Blumenthal, G. R., Faber, S. M., Primack, J. R., & Rees, M. J. 1984, Nature, 311, 517

Blumenthal, G. R., Faber, S. M., Flores, R., & Primack, J. R. 1986, ApJ, 301, 27

Boylan-Kolchin, M., Bullock, J. S., & Kaplinghat, M. 2012, MNRAS, 422, 1203

Boylan-Kolchin, M., Bullock, J. S., & Kaplinghat, M. 2011, MNRAS, 415, L40

Bradač, M., Allen, S. W., Treu, T., et al. 2008, ApJ, 687, 959

Broadhurst, T., Benítez, N., Coe, D., et al. 2005, ApJ, 621, 53

Broadhurst, T. J., Taylor, A. N., & Peacock, J. A. 1995, ApJ, 438, 49

Brodie, J. P., & Huchra, J. P. 1991, ApJ, 379, 157

Brodie, J. P., & Strader, J. 2006, ARA&A, 44, 193

Bruzual, G., & Charlot, S. 2003, MNRAS, 344, 1000

Buonanno, R., Corsi, C. E., Pulone, L., Fusi Pecci, F., & Bellazzini, M. 1998, A&A, 333, 505

Burstein, D., & Rubin, V. C. 1985, ApJ, 297, 423

Burnham, R. 1966, Flagstaff, Ariz., Celestial Handbook Publications 1966

Byun, Y.-I., Grillmair, C. J., Faber, S. M., et al. 1996, AJ, 111, 1889

Cavaliere, A., & Fusco-Femiano, R. 1976, A&A, 49, 137

Chaboyer, B., Demarque, P., Kernan, P. J., Krauss, L. M., & Sarajedini, A. 1996, MNRAS, 283, 683

Chabrier, G. 2003, PASP, 115, 763

Chies-Santos, A. L., Larsen, S. S., Kuntschner, H., et al. 2011, A&A, 525, A20

Chies-Santos, A. L., Larsen, S. S., Cantiello, M., et al. 2012, A&A, 539, A54

Cho, J., Sharples, R. M., Blakeslee, J. P., et al. 2012, MNRAS, 422, 3591

Clowe, D., Bradač, M., Gonzalez, A. H., et al. 2006, ApJ, 648, L109

Coe, D., Benítez, N., Broadhurst, T., & Moustakas, L. A. 2010, ApJ, 723, 1678

Cohen, J. G., Blakeslee, J. P., & Ryzhov, A. 1998, ApJ, 496, 808

Cohen, J. G., Blakeslee, J. P., & Côté, P. 2003, ApJ, 592, 866

Colbert, J. W., Mulchaey, J. S., & Zabludoff, A. I. 2001, AJ, 121, 808

Collins, C. A., Stott, J. P., Hilton, M., et al. 2009, Nature, 458, 603

Conroy, C., & van Dokkum, P. G. 2012, ApJ, 760, 71

Conroy, C., & Wechsler, R. H. 2009, ApJ, 696, 620

Côté, P., Marzke, R. O., & West, M. J. 1998, ApJ, 501, 554

Côté, P. 1999, AJ, 118, 406

Côté, P., Blakeslee, J. P., Ferrarese, L., et al. 2004, ApJS, 153, 223

Côté, P., Ferrarese, L., Jordán, A., et al. 2007, ApJ, 671, 1456

Cowie, L. L., Songaila, A., Hu, E. M., & Cohen, J. G. 1996, AJ, 112, 839

Cui, W., Springel, V., Yang, X., De Lucia, G., & Borgani, S. 2011, MNRAS, 416, 2997

Cypriano, E. S., Mendes de Oliveira, C. L., & Sodré, L., Jr. 2006, AJ, 132, 514

Dariush, A., Khosroshahi, H. G., Ponman, T. J., et al. 2007, MNRAS, 382, 433

De Angeli, F., Piotto, G., Cassisi, S., et al. 2005, AJ, 130, 116

De Lucia, G., Springel, V., White, S. D. M., Croton, D., & Kauffmann, G. 2006, MNRAS, 366, 499

De Lucia, G., & Helmi, A. 2008, MNRAS, 391, 14

Demarque, P. 1967, ApJ, 149, 117

de Blok, W. J. G. 2010, Advances in Astronomy, 2010, 789293

de Souza, R. E., Gadotti, D. A., & dos Anjos, S. 2004, ApJS, 153, 411

de Vaucouleurs, G. 1948, Annales d'Astrophysique, 11, 247

de Vaucouleurs, G. 1959, Handbuch der Physik, 53, 275

Djorgovski, S., & Davis, M. 1987, ApJ, 313, 59

Djorgovski, S. G. 1998, S&T, 96, 38

Díaz-Giménez, E., Muriel, H., & Mendes de Oliveira, C. 2008, A&A, 490, 965

Díaz-Giménez, E., Zandivarez, A., Proctor, R., Mendes de Oliveira, C., & Abramo, L. R. 2011, A&A, 527, A129

Donzelli, C. J., Muriel, H., & Madrid, J. P. 2011, ApJS, 195, 15

D'Onghia, E., Sommer-Larsen, J., Romeo, A. D., et al. 2005, ApJ, 630, L109

Dressler, A. 1980, ApJ, 236, 351

Eddington, A. S. 1913, MNRAS, 73, 359

Eddington, A. S. 1913, MNRAS, 74, 5

Eddington, A. S. 1915, MNRAS, 75, 366

Eddington, A. S. 1917, The Observatory, 40, 394

Eigenthaler, P., & Zeilinger, W. W. 2012, arXiv:1202.4470

Eggen, O. J., Lynden-Bell, D., & Sandage, A. R. 1962, ApJ, 136, 748

Fall, S. M., & Rees, M. J. 1977, MNRAS, 181, 37P

Fall, S. M., & Rees, M. J. 1985, ApJ, 298, 1

Fasano, G., Bettoni, D., Ascaso, B., et al. 2010, MNRAS, 404, 1490

Ferrarese, L., Ford, H. C., Huchra, J., et al. 2000, ApJS, 128, 431

Ferrarese, L., Côté, P., Jordán, A., et al. 2006, ApJS, 164, 334

Ferrarese, L., Côté, P., Cuillandre, J.-C., et al. 2012, ApJS, 200, 4

Fleming, D. E. B., Harris, W. E., Pritchet, C. J., & Hanes, D. A. 1995, AJ, 109, 1044

Flynn, C., Holmberg, J., Portinari, L., Fuchs, B., & Jahreiß, H. 2006, MNRAS, 372, 1149

Font, A. S., Johnston, K. V., Bullock, J. S., & Robertson, B. E. 2006, ApJ, 638, 585

Forbes, D. A., Franx, M., Illingworth, G. D., & Carollo, C. M. 1996, ApJ, 467, 126

Forbes, D. A., Brodie, J. P., & Huchra, J. 1997, AJ, 113, 887

Ford, H. C., Clampin, M., Hartig, G. F., et al. 2003, Proc. SPIE, 4854, 81

Ford, H. C., Illingworth, G. D., Clampin, M., et al. 2002, BAAS, 34, 675

Forman, W., Kellogg, E., Gursky, H., Tananbaum, H., & Giacconi, R. 1972, ApJ, 178, 309

Freeman, K. C., & Norris, J. 1981, ARA&A, 19, 319

Fruchter, A. S., & Hook, R. N. 2002, PASP, 114, 144

Gebhardt, K., & Kissler-Patig, M. 1999, AJ, 118, 1526

Geisler, D., Lee, M. G., & Kim, E. 1996, AJ, 111, 1529

Georgiev, I. Y., Puzia, T. H., Goudfrooij, P., & Hilker, M. 2010, MNRAS, 406, 1967

Girardi, M., Fadda, D., Escalera, E., et al. 1997, ApJ, 490, 56

Gorenstein, P., Fabricant, D., Topka, K., Harnden, F. R., Jr., & Tucker, W. H. 1978, ApJ, 224, 718

Goudfrooij, P., Strader, J., Brenneman, L., et al. 2003, MNRAS, 343, 665

Goudfrooij, P., Puzia, T. H., Chandar, R., & Kozhurina-Platais, V. 2011, ApJ, 737, 4

Graham, A. W., & Driver, S. P. 2005, PASA, 22, 118

Graham, A., Lauer, T. R., Colless, M., & Postman, M. 1996, ApJ, 465, 534

Gratton, R. G., Lucatello, S., Carretta, E., et al. 2012, A&A, 539, A19

Guo, Q., White, S., Li, C., & Boylan-Kolchin, M. 2010, MNRAS, 404, 1111

Hanes, D. A. 1977, MNRAS, 180, 309

Harris, W. E. 1974, Ph.D. Thesis

Harris, W. E., & Racine, R. 1979, ARA&A, 17, 241

Harris, W. E., & van den Bergh, S. 1981, AJ, 86, 1627

Harris, W. E. 1991, AJ, 102, 1348

Harris, W. E. 1991, ARA&A, 29, 543

Harris, W. E., & Pudritz, R. E. 1994, ApJ, 429, 177

Harris, W. E., Pritchet, C. J., & McClure, R. D. 1995, ApJ, 441, 120

Harris, W. E. 2001, Star Clusters, Saas-Fee Advanced Courses, Volume 28, Springer-Verlag Berlin Heidelberg, 223

Harris, W. E., & Harris, G. L. H. 2002, AJ, 123, 3108

Harris, W. E., Whitmore, B. C., Karakla, D., et al. 2006, ApJ, 636, 90

Harris, W. E., Kavelaars, J. J., Hanes, D. A., Pritchet, C. J., & Baum, W. A. 2009, AJ, 137, 3314

Hartwick, F. D. A., & vanden Berg, D. A. 1973, ApJ, 185, 887

Herschel, W. 1789, Royal Society of London Philosophical Transactions Series I, 79, 212

Hertzsprung, E. 1913, Astronomische Nachrichten, 196, 201

Hinshaw, G., Larson, D., Komatsu, E., et al. 2013, ApJS, submitted

Hoyle, F. 1959, MNRAS, 119, 124

Hubble, E. P. 1926, ApJ, 64, 321

Humason, M. L., Mayall, N. U., & Sandage, A. R. 1956, AJ, 61, 97

Izenman, A. J. 1991, Am. Stat. Assoc., 86, 205

Jedrzejewski, R. I. 1987, MNRAS, 226, 747

Jee, M. J., Ford, H. C., Illingworth, G. D., et al. 2007, ApJ, 661, 728

Johansson, P. H., Naab, T., & Ostriker, J. P. 2012, arXiv:1202.3441

Johnston, K. V., Bullock, J. S., Sharma, S., et al. 2008, ApJ, 689, 936

Jones, C., & Forman, W. 1984, ApJ, 276, 38

Jones, L. R., Ponman, T. J., & Forbes, D. A. 2000, MNRAS, 312, 139

Jones, L. R., Ponman, T. J., Horton, A., et al. 2003, MNRAS, 343, 627

Jordán, A., West, M. J., Côté, P., & Marzke, R. O. 2003, AJ, 125, 1642

Jordán, A., Côté, P., West, M. J., et al. 2004, AJ, 127, 24

Jordán, A., Blakeslee, J. P., Peng, E. W., et al. 2004, ApJS, 154, 509

Jordán, A., Côté, P., Blakeslee, J. P., et al. 2005, ApJ, 634, 1002

Jordán, A., McLaughlin, D. E., Côté, P., et al. 2006, ApJ, 651, L25

Jordán, A., McLaughlin, D. E., Côté, P., et al. 2007, ApJS, 171, 101

Jordán, A., Blakeslee, J. P., Côté, P., Ferrarese, L., Infante, L., Mei, S., Merritt, D., Peng, E. W., Tonry, J. L., West, M. J. 2007, ApJS, 169, 213

Khosroshahi, H. G., Jones, L. R., & Ponman, T. J. 2004, MNRAS, 349, 1240

Khosroshahi, H. G., Ponman, T. J., & Jones, L. R. 2006, MNRAS, 372, L68

Khosroshahi, H. G., Ponman, T. J., & Jones, L. R. 2007, MNRAS, 377, 595

King, I. 1962, AJ, 67, 471

King, I. R. 1966, AJ, 71, 64

Komatsu, E., Smith, K. M., Dunkley, J., et al. 2011, ApJS, 192, 18

Kormendy, J., & Bender, R. 1996, ApJ, 464, L119

Kormendy, J., Fisher, D. B., Cornell, M. E., & Bender, R. 2009, ApJS, 182, 216

Kraft, R. P. 1979, ARA&A, 17, 309

Kron, G. E., & Mayall, N. U. 1960, AJ, 65, 581

Kroupa, P. 2001, MNRAS, 322, 231

Kroupa, P. 2002, Science, 295, 82

Kruijssen, J. M. D. 2012, MNRAS, 426, 3008

Kundu, A., & Whitmore, B. C. 2001, AJ, 121, 2950

La Barbera, F., Paolillo, M., De Filippis, E., & de Carvalho, R. R. 2012, MNRAS, 422, 3010

Laganá, T. F., Zhang, Y.-Y., Reiprich, T. H., & Schneider, P. 2011, ApJ, 743, 13

Larsen, S. S., & Richtler, T. 2000, A&A, 354, 836

Larsen, S. S., Brodie, J. P., Huchra, J. P., Forbes, D. A., & Grillmair, C. J. 2001, AJ, 121, 2974

Larson, R. B. 2005, MNRAS, 359, 211

Leavitt, H. S., & Pickering, E. C. 1912, Harvard College Observatory Circular, 173, 1

Lee, M. G., Park, H. S., & Hwang, H. S. 2010, Science, 328, 334

Lemze, D., Barkana, R., Broadhurst, T. J., & Rephaeli, Y. 2008, MNRAS, 386, 1092

Lemze, D., Broadhurst, T., Rephaeli, Y., Barkana, R., & Umetsu, K. 2009, ApJ, 701, 1336

Limousin, M., Richard, J., Jullo, E., et al. 2007, ApJ, 668, 643

Lin, Y.-T., Stanford, S. A., Eisenhardt, P. R. M., et al. 2012, ApJ, 745, L3

Lotz, J. M., Miller, B. W., & Ferguson, H. C. 2004, ApJ, 613, 262

Loveday, J. 2004, MNRAS, 347, 601

Loveday, J., Norberg, P., Baldry, I. K., et al. 2012, MNRAS, 420, 1239

Madrid, J. P. 2011, ApJ, 737, L13

Madrid, J. P., & Donzelli, C. J. 2013, ApJ, 770, 158

Martínez-Delgado, D., Peñarrubia, J., Gabany, R. J., et al. 2008, ApJ, 689, 184

McLaughlin, D. E., Harris, W. E., & Hanes, D. A. 1994, ApJ, 422, 486

McLaughlin, D. E. 1999, AJ, 117, 2398

McLaughlin, D. E., & Fall, S. M. 2008, ApJ, 679, 1272

McMillan, P. J. 2011, MNRAS, 414, 2446

Mendes de Oliveira, C. L., & Carrasco, E. R. 2007, ApJ, 670, L93

Mendes de Oliveira, C. L., Cypriano, E. S., Dupke, R. A., & Sodré, L., Jr. 2009, AJ, 138, 502

Méndez-Abreu, J., Aguerri, J. A. L., Barrena, R., et al. 2012, A&A, 537, A25

Mieske, S., Infante, L., Benítez, N., et al. 2004, AJ, 128, 1529

Miller, B. W., Lotz, J. M., Ferguson, H. C., Stiavelli, M., & Whitmore, B. C. 1998, ApJ, 508, L133

Moore, B., Diemand, J., Madau, P., Zemp, M., & Stadel, J. 2006, MNRAS, 368, 563

Morgan, W. W., & Mayall, N. U. 1957, PASP, 69, 291

Morgan, W. W., & Osterbrock, D. E. 1969, AJ, 74, 515

Mulchaey, J. S., & Zabludoff, A. I. 1999, ApJ, 514, 133

Muratov, A. L., & Gnedin, O. Y. 2010, ApJ, 718, 1266

Naab, T., Johansson, P. H., & Ostriker, J. P. 2009, ApJ, 699, L178

Nair, P., van den Bergh, S., & Abraham, R. G. 2011, ApJ, 734, L31

Nelder, J. A. & Mead, R. 1965, The Computer Journal, 308, 313

Navarro, J. F., Frenk, C. S., & White, S. D. M. 1997, ApJ, 490, 493

Oemler, A., Jr. 1974, ApJ, 194, 1

Oemler, A., Jr. 1976, ApJ, 209, 693

Oh, S.-H., Brook, C., Governato, F., et al. 2011, AJ, 142, 24

Ostriker, J. P., & Peebles, P. J. E. 1973, ApJ, 186, 467

Ostriker, J. P., Peebles, P. J. E., & Yahil, A. 1974, ApJ, 193, L1

Page, T. 1952, ApJ, 116, 63

Page, T. 1960, ApJ, 132, 910

Partridge, R. B., & Peebles, P. J. E. 1967, ApJ, 147, 868

Peebles, P. J. E., & Dicke, R. H. 1968, ApJ, 154, 891

Peimbert, M. 1968, ApJ, 154, 33

Peng, E. W., Jordán, A., Côté, P., et al. 2006, ApJ, 639, 95

Peng, E. W., Jordán, A., Côté, P., et al. 2008, ApJ, 681, 197

Peng, E. W., Jordán, A., Blakeslee, J. P., et al. 2009, ApJ, 703, 42

Peng, E. W., Ferguson, H. C., Goudfrooij, P., et al. 2011, ApJ, 730, 23

Penzias, A. A., & Wilson, R. W. 1965, ApJ, 142, 419

Peterson, C. J., & King, I. R. 1975, AJ, 80, 427

Piotto, G., Bedin, L. R., Anderson, J., et al. 2007, ApJ, 661, L53

Piotto, G., Milone, A. P., Anderson, J., et al. 2012, ApJ, 760, 39

Ponman, T. J., Allan, D. J., Jones, L. R., et al. 1994, Nature, 369, 462

Postman, M., & Lauer, T. R. 1995, ApJ, 440, 28

Press, W. H., & Schechter, P. 1974, ApJ, 187, 425

Proctor, R. N., de Oliveira, C. M., Dupke, R., et al. 2011, MNRAS, 418, 2054

Pryor, C., & Meylan, G. 1993, Structure and Dynamics of Globular Clusters, 50, 357

Puzia, T. H., Kissler-Patig, M., Thomas, D., et al. 2005, A&A, 439, 997

Renzini, A. 1991, The Magellanic Clouds, 148, 165

Rhode, K. L., & Zepf, S. E. 2004, AJ, 127, 302

Rood, H. J., Page, T. L., Kintner, E. C., & King, I. R. 1972, ApJ, 175, 627

Rubin, V. C., & Ford, W. K., Jr. 1970, ApJ, 159, 379

Rubin, V. C., Ford, W. K. J., & . Thonnard, N. 1980, ApJ, 238, 471

Russell, H. N. 1914, Nature, 93, 252

Sales, L. V., Navarro, J. F., Theuns, T., et al. 2012, MNRAS, 423, 1544

Salpeter, E. E. 1955, ApJ, 121, 161

Sandage, A. 1962, ApJ, 135, 349

Sandage, A. 1982, ApJ, 252, 553

Sarajedini, A., Bedin, L. R., Chaboyer, B., et al. 2007, AJ, 133, 1658

Searle, L., & Zinn, R. 1978, ApJ, 225, 357

Seigar, M. S., Graham, A. W., & Jerjen, H. 2007, MNRAS, 378, 1575

Sereno, M., Ettori, S., Umetsu, K., & Baldi, A. 2013, MNRAS, 428, 2241

Sérsic, J. L. 1968, Atlas de Galaxias Australes (Cordoba: Observatorio Astronomico)

Schechter, P. 1976, ApJ, 203, 297

Schlafly, E. F., & Finkbeiner, D. P. 2011, ApJ, 737, 103

Schlegel, D. J., Finkbeiner, D. P., & Davis, M. 1998, ApJ, 500, 525

Schombert, J. M. 1988, ApJ, 328, 475

Schombert, J., & Smith, A. K. 2012, PASA, 29, 174

Silk, J., & Mamon, G. A. 2012, Research in Astronomy and Astrophysics, 12, 917

Sirianni, M., Jee, M. J., Benítez, N., et al. 2005, PASP, 117, 1049

Shapley, H. 1916, The Observatory, 39, 452

Shapley, H. 1917, PASP, 29, 245

Shapley, H., & Sawyer, H. B. 1927, Harvard College Observatory Bulletin, 852, 22

Spitler, L. R., & Forbes, D. A. 2009, MNRAS, 392, L1

Spitzer, L., Jr., & Hart, M. H. 1971, ApJ, 166, 483

Spitzer, L., Jr., & Thuan, T. X. 1972, ApJ, 175, 31

Springel, V., White, S. D. M., Jenkins, A., et al. 2005, Nature, 435, 629

Springel, V., Frenk, C. S., & White, S. D. M. 2006, Nature, 440, 1137

Stetson, P. B. 1987, PASP, 99, 191

Strader, J., Brodie, J. P., Spitler, L., & Beasley, M. A. 2006, AJ, 132, 2333

Suárez-Madrigal, A., Ballesteros-Paredes, J., Colín, P., & D'Alessio, P. 2012, ApJ, 748, 101

Sun, M., Forman, W., Vikhlinin, A., et al. 2004, ApJ, 612, 805

Tamura, N., Sharples, R. M., Arimoto, N., et al. 2006, MNRAS, 373, 588

Taylor, A. N., Dye, S., Broadhurst, T. J., Benitez, N., & van Kampen, E. 1998, ApJ, 501, 539

Teague, P. F., Carter, D., & Gray, P. M. 1990, ApJS, 72, 715

Tody, D. 1986, Proc. SPIE, 627, 733

Tody, D. 1993, Astronomical Data Analysis Software and Systems II, 52, 173

Tonry, J. L., Dressler, A., Blakeslee, J. P., et al. 2001, ApJ, 546, 681

Toomre, A., & Toomre, J. 1972, ApJ, 178, 623

Toomre, A. 1977, Evolution of Galaxies and Stellar Populations, 401

Tortora, C., Napolitano, N. R., Romanowsky, A. J., Capaccioli, M., & Covone, G. 2009, MNRAS, 396, 1132

Tovmassian, H. 2010, Rev. Mexicana Astron. Astrofis., 46, 61

Trujillo, I., Erwin, P., Asensio Ramos, A., & Graham, A. W. 2004, AJ, 127, 1917

Tyson, J. A., & Fischer, P. 1995, ApJ, 446, L55

Vandenberg, D. A. 1983, ApJS, 51, 29

Vandenberg, D. A. 1988, *The extragalactic distance scale* (ASP Conf. Ser. 4), ed. S. van den Bergh & C. J. Pritchet (San Francisco, CA: ASP), 187

Vandenberg, D. A., Bolte, M., & Stetson, P. B. 1990, AJ, 100, 445

van den Bergh, S. 1956, Z. Astrophys., 41, 61

van den Bergh, S. 1971, JRASC, 65, 13

van den Bergh, S. 1975, ARA&A, 13, 217

van den Bergh, S., & Harris, W. E. 1982, AJ, 87, 494

van den Bergh, S., Morbey, C., & Pazder, J. 1991, ApJ, 375, 594

van den Bergh, S. 1998, Galaxy morphology and classification, Cambridge University Press, 1998. QB857 .V36 1998

van den Bosch, F. C., Yang, X., Mo, H. J., et al. 2007, MNRAS, 376, 841

van Dokkum, P. G., & Conroy, C. 2010, Nature, 468, 940

Vikhlinin, A., McNamara, B. R., Hornstrup, A., et al. 1999, ApJ, 520, L1

Villegas, D., Jordán, A., Peng, E. W., et al. 2010, ApJ, 717, 603

von Benda-Beckmann, A. M., D'Onghia, E., Gottlöber, S., et al. 2008, MNRAS, 386, 2345

Wehner, E. M. H., Harris, W. E., Whitmore, B. C., Rothberg, B., & Woodley, K. A. 2008, ApJ, 681, 1233

West, M. J. 1993, MNRAS, 265, 755

West, M. J., Cote, P., Jones, C., Forman, W., & Marzke, R. O. 1995, ApJ, 453, L77

West, M. J., Côté, P., Marzke, R. O., & Jordán, A. 2004, Nature, 427, 31

West, M. J., Jordán, A., Blakeslee, J. P., et al. 2011, A&A, 528, A115

White, S. D. M., & Rees, M. J. 1978, MNRAS, 183, 341

Whitmore, B. C., Sparks, W. B., Lucas, R. A., Macchetto, F. D., & Biretta, J. A. 1995, ApJ, 454, L73

Whitmore, B. C., & Schweizer, F. 1995, AJ, 109, 960

Worthey, G. 1994, ApJS, 95, 107

Yoon, S.-J., Yi, S. K., & Lee, Y.-W. 2006, Science, 311, 1129

Yoon, S.-J., Lee, S.-Y., Blakeslee, J. P., et al. 2011, ApJ, 743, 150

Yoshioka, T., Furuzawa, A., Takahashi, S., et al. 2004, Advances in Space Research, 34, 2525

Zekser, K. C., White, R. L., Broadhurst, T. J., et al. 2006, ApJ, 640, 639

Zepf, S. E., & Ashman, K. M. 1993, MNRAS, 264, 611

Zepf, S. E., Ashman, K. M., English, J., Freeman, K. C., & Sharples, R. M. 1999, AJ, 118, 752

Zhang, Q., & Fall, S. M. 1999, ApJ, 527, L81

Zinn, R. 1985, ApJ, 293, 424

Zwicky, F. 1937, ApJ, 86, 217